

**NANOFABRICATION USING OPTIMIZED  
PROTON BEAM WRITING AND MASKED ION  
LITHOGRAPHY**

**SARFRAZ QURESHI**

(*B. Tech., IIT Indore*)

**A THESIS SUBMITTED FOR THE DEGREE OF  
DOCTOR OF PHILOSOPHY**

**DEPARTMENT OF PHYSICS**

**NATIONAL UNIVERSITY OF SINGAPORE**

**2018**

Supervisor:

Associate Professor Jeroen Anton van Kan

Examiners:

Associate Professor Osipowicz, Thomas

Associate Professor Bettoli, Andrew Anthony

Professor Harry Whitlow, University of Louisiana at Lafayette



## **DECLARATION**

I hereby declare that this thesis is my original work and it has been written by me in its entirety. I have duly acknowledged all the sources of information which have been used in this thesis.

This thesis has also not been submitted for any degree in any university previously.

A handwritten signature in black ink, appearing to read "Sarfraz Qureshi".

---

Sarfraz Qureshi

24 August 2018



# Acknowledgements

I would like to express my deepest gratitude to my supervisor Assoc. Prof. Jeroen van Kan who introduced me to the world of ion beams. I am indebted for his continuous support, supervision and constructive criticism.

I would like to thank Dr. P. Santhana Raman for his mentorship and efforts to ensure a smooth running of the Singletron without which this thesis wouldn't have been possible.

I would like to acknowledge Dr. Liu Fan, who taught me Proton Beam Writing. Liu fan is a great mentor and a friend who has been available for discussion at odd hours. Special hearty thanks to Dr. Saumitra for his impeccable micro-positioning hands and helping me with the broad beam irradiation. It was a privilege collaborating with Dr. Tanmoy and Dr. Haidong. They both taught me the value of enthusiasm and persistence. I can't express how much I have learnt and relied on Mr. Tan Huei Ming both at personal and professional level. Huei Ming is a curious engineer with wide spectrum of talent. I would like to thank Dr. Prashant for the discussions about DAQ and programming.

Thanks to Assoc. Prof. Thomas Osipowicz. Assoc. Prof. Andrew Bettoli, and Prof. Mark Breese for their encouragement and valuable insights.

I am grateful to my friends Dr. Shriram Venkatesan, (soon-to-be) Dr. Monika, Ms. Mallika, Mr. Nihar, Ms. Alisha Ms. Shefali, Mr. Pang Rudy and Ms Tao Ye for their constant support and encouragement.

I would like to extend my gratitude to all the members of CIBA, for their help and encouragement, Dr. Xinxin Xu, Mr. Choo Theam Fook, Dr. Ren Minqin, Dr. Chen Ce-Belle, Dr. Mi Zhaohong (Mike), Mr. Tan Hong Qi, Ms. Shi Yi, Mr. Jin Huining (Kim), and Mr. Gong Jingtao. It has been my great honor to work in Centre for Ion Beam Application, a home away from home!

I wouldn't have been who I am today if not for my parents' sacrifice. I am thankful for your teachings and support for all these years.

To my fiance', Dr. Deepika Raman, I don't know how to thank you for your patience and intuitive approach to things. It is because of you I met the kitties; Simu, Spotty, Plum, Hobbes and Chapati.

## Table of contents

Acknowledgements.....	i
Abstract.....	vii
List of tables.....	x
List of figures .....	xi
List of abbreviations .....	xvi
1    Introduction .....	1
1.1    Overview of nanofabrication.....	1
1.2    Resist materials for nanofabrication.....	2
1.2.1    PMMA .....	3
1.2.2    HSQ.....	3
1.2.3    Characterization of photo-resist.....	4
1.3    Techniques for lithography .....	5
1.3.1    Photolithography.....	5
1.3.2    Electron beam lithography (EBL).....	6
1.3.3    Ion beam lithography .....	7
1.3.4    Soft lithography .....	9
1.4    Interaction of charged particles with photoresist .....	9
1.5    Applications of proton beam writing .....	12
1.5.1    Nanoimprinting .....	13
1.5.2    Micro/Nanofluidics .....	13
1.5.3    Photonics.....	14
1.5.4    Silicon micromachining .....	16
1.5.5    High resolution resists.....	16
1.6    Motivation for the thesis .....	21
2    PBW at CIBA .....	23
2.1    Accelerator layout .....	23
2.2    Beam defining apertures.....	24
2.3    Electrostatic scanners .....	25
2.4    Beam blanking.....	26
2.5    Probe-forming lenses.....	26
2.6    Beam line optics .....	31
2.7    Beam size estimation and focusing performance.....	33
2.8    Target chamber.....	35
2.9    Data acquisition (automation) .....	37
2.10    Summary .....	38

3	Beam control optimization .....	39
3.1	Depth of focus .....	39
3.2	Automated closed loop.....	40
3.2.1	Calibration for step mode.....	41
3.2.2	Feedback selection .....	42
3.2.3	Algorithm development .....	42
3.3	Sidewall slope estimation.....	43
3.4	Quadrupole alignment .....	47
3.5	Automated slit control.....	53
3.5.1	Hardware design .....	54
3.5.2	Algorithm and control interface.....	56
3.5.3	Results.....	59
3.6	Autofocusing .....	61
3.6.1	Grid imaging .....	62
3.6.2	Automated focusing .....	64
3.7	Writing strategy.....	69
3.7.1	Step and repeat.....	70
3.7.2	Stage scan.....	71
3.8	Stitching .....	74
3.9	Fabrication of resolution standard.....	76
3.9.1	Fabrication of Au resolution standard.....	77
3.10	Secondary electron efficiency from Ni and Au grid .....	79
3.11	Summary .....	85
4	Applications of PBW in Resist Materials.....	86
4.1	General processing for PBW .....	86
4.1.1	Sample preparation .....	86
4.1.2	Metal seed layer deposition .....	87
4.1.3	Proton beam writing.....	87
4.1.4	Exposure files.....	88
4.1.5	Electroplating and copper etching .....	88
4.2	PBW in PMMA.....	89
4.2.1	Nanograting fabrication .....	89
4.2.2	High aspect ratio nano-channels fabrication.....	93
4.2.3	Nano-grating fabrication in PMMA.....	97
4.2.4	Metal lift-off for graphene deposition.....	100
4.3	PBW in HSQ .....	101
4.3.1	Nano-imprinting mask fabrication .....	101

4.3.2	Stamp fabrication .....	105
4.3.3	Linearization of single stranded DNA .....	106
4.3.4	Pillar fabrication in 100 nm thick HSQ .....	108
4.3.5	Line fabrication in 100 nm thick HSQ.....	111
4.3.6	Pillars written with focused 1 MeV He <sup>+</sup> .....	112
4.4	PBW in non-resist based substrates .....	114
4.4.1	Silicon .....	114
4.4.2	STO .....	116
4.5	Summary .....	117
5	Simulation of Masked Ion Lithography.....	119
5.1	Introduction .....	119
5.2	Simulation of masked ion irradiation .....	125
5.2.1	Geant4 simulation setup.....	125
5.2.2	Range of ions in Ni .....	128
5.2.3	Results.....	130
5.2.4	Effect of edge scattering .....	132
5.2.5	Simulation of 60 nm lines separated by 500 nm.....	136
5.2.6	Effect of beam divergence .....	140
5.2.7	Effect of mask-sample tilt with respect to beam.....	142
5.2.8	Effect of mask to sample gap.....	145
5.2.9	Simulation of 250 nm apertures .....	146
5.2.10	Resolution test with 10 nm aperture .....	146
5.2.11	Simulation of lines and spaces .....	147
5.3	Summary .....	148
6	Masked Ion Lithography Experiments .....	150
6.1	Introduction .....	150
6.2	Mask fabrication in ma-N 2410 .....	150
6.2.1	Pillars written in ma-N.....	151
6.2.2	Grating writing in ma-N 2410.....	153
6.2.3	Ni electroplating.....	156
6.2.4	Cu etching .....	160
6.2.5	Experimental set-up .....	160
6.2.6	Irradiation parameter.....	161
6.2.7	Developed feature .....	162
6.3	Summary .....	164
7	Conclusion and future work .....	166
	List of publications .....	171

References.....	172
-----------------	-----

# Abstract

Proton Beam Writing (PBW) is a direct-write lithographic technique used for micro- and nano-fabrication using a beam of focused protons. An incident proton can interact with the substrate electrons and nuclei through electronic and nuclear scattering respectively. Due to mass and momentum mismatch between the incident proton and substrate electron, a beam of protons has a straight trajectory featuring minimal proximity effect coupled with a uniform energy deposition in thin polymer layers. A spot size of  $9.3\text{ nm} \times 32\text{ nm}$  has been demonstrated in CIBA through an optimized beam optics arrangement using magnetic quadrupole lenses. Feature sizes matching the focused beam spot size have been fabricated in photoresists down to 19 nm. Reproducible sub-10 nm beam focusing will make PBW a promising contender for sub-10 nm lithography. The major limitation in terms of focusing, is the lower brightness from the RF ion sources used for generating ions. A nano-aperture ion source is currently under development in CIBA which shows a four-order increase in the reduced brightness of the system. In this thesis, we present optimization of the proton beam writing beamline towards reproducible nanofabrication in photoresist. The thesis focuses on three areas of improvement: optimization of beam controls, resist characterization for high resolution PBW and high aspect ratio stencil fabrication and masked ion lithography for higher throughput.

Optimization of the proton beam writing control was performed for positioning, automated alignment and focusing, and imaging. Through bias optimization of a micro-channel plate (MCP), we show a tuneable secondary electron detection per proton, for imaging Ni and Au resolution standards. Fabrication of a 200 nm

thin free-standing gold resolution standard further improves the secondary electron collection efficiency to  $92 \pm 5$  % secondary electron yield per proton. Based on Scanning Transmission Ion Microscopy (STIM) mode beam size measurement, we discuss considerations for quadrupole system alignment to remove higher order translational and rotational misalignments, critical to achieve sub-50 nm spot sizes. A spot size of  $13 \times 32$  nm<sup>2</sup> (STIM) was achieved using a newly developed interface, capable of autofocusing ion beams and automatic slit alignment.

Performance characterization of high-resolution photoresists, HSQ and PMMA, was performed for sub-50 nm lithography. We demonstrate fabrication of high aspect ratio Ni apertures through channel fabrication in PMMA and subsequent Ni electroplating. For faster replication, we show fabrication of nanoimprint master used to fabricate nanofluidic chip for DNA extension. For large area fabrication, we have shown a combined beam and stage writing with minimized stitching error. We show fabrication of 30 nm channels in 2  $\mu$ m thick PMMA (aspect ratio ~67) using 2 MeV proton beam focused down to 30 nm. Besides, 42 nm lines in HSQ were fabricated to be used as master for lab-on-a-chip device nanoimprinting. We have shown fabrication of high aspect ratio channels in porous silicon with features down to 100 nm.

Aiming towards higher throughput, we demonstrate fabrication of high aspect ratio Ni stencil mask with 60 nm features using PBW. Through metal stencil fabrication using focused PBW, we have demonstrated faster replication of nanostructures down to 60 nm using masked ion lithography. A Geant4 Monte

Carlo simulation was carried out to analyse the experimental results of masked proton lithography and its limitations down to 10 nm features.

## List of tables

Table 2-1. System layout of spaced oxford triplet .....	31
Table 2-2. Aberration Coefficient for spaced oxford triplet extracted from PBO simulations .....	32
Table 2-3 Total percentage of beam as a function of sigma .....	35
Table 3-1. Parameters used/estimated for grid thickness measurement .....	47
Table 3-2. Beam parameters used for focusing .....	69
Table 3-3. Stage motion for single beam scan length.....	73
Table 3-4. Summary of stitching error with step and repeat lithography .....	76
Table 4-1. Step and repeat in 400 nm PMMA .....	91
Table 5-1. Critical angle vs aperture or line width. ....	143
Table 6-1. Parameters for writing pillars in ma-N 2410.....	152
Table 6-2. Optimum dose comparison from SRIM .....	162

# List of figures

Figure 1-1 Molecular structure of PMMA monomer .....	3
Figure 1-2. Crosslinking of HSQ leading to formation of cage.....	4
Figure 1-3. Contrast curve measured for 2 MeV protons at two different exposure timings .....	5
Figure 1-4. Spatial energy density map for protons and electrons .....	11
Figure 1-5. Fabrication of nanochannels in 3 $\mu\text{m}$ thick PMMA using EBL (figure taken from [77]) .....	12
Figure 2-1. Accelerator and beamline layout at Centre for Ion Beam Applications (CIBA), NUS .....	23
Figure 2-2. Cross-section of a quadrupole lens. Shown are the four pole pieces generating magnetic field lines in the space within. Positively charged particles at position 1 and 2 travel into the plane of the paper .....	27
Figure 2-3. Layout of the beamline optics for PBW at CIBA. 3 Quadrupole lenses configured in spaced oxford triplet mode (CDC) with first and second lens coupled to the same power supply.....	31
Figure 2-4. PBO Simulation of 2 MeV proton. The beam line demagnification is calculated to be $857 \times 130$ . Figure (a) shows the particle distribution in an objective slit of opening $8 \times 4 \mu\text{m}^2$ ; (b) shows the beam spot size of $9.3 \times 32 \text{ nm}^2$ . Collimator aperture was set for $30 \times 30 \mu\text{m}^2$ . ....	32
Figure 2-5 Schematic of beam spot estimation.....	33
Figure 3-1. Beam full width half maximum vs focal plane offset. For fixed quadrupole excitation, if the sample plane is shifted off from the focal plane, beam spot increases more for the direction of higher demagnification. ....	40
Figure 3-2. Schematic of the closed loop control in Z.....	40
Figure 3-3. Differential step motion as a function of amplitude voltage applied. In the algorithm this determines the number of steps and step voltage needed to minimize the positioning error. ....	42
Figure 3-4 (a) STIM Spectrum of 1 MeV $\text{H}_2^+$ through Ni grid. (b) STIM spectrum through 0, 2.5 $\mu\text{m}$ and 5 $\mu\text{m}$ thick layers of Mylar. Inset shows the On-axis STIM image over a scan size of $130 \times 130 \mu\text{m}^2$ .....	45
Figure 3-5. Y FWHM plotted as function of collimator translation in X and Y directions around quadrupole optic axis. ....	48
Figure 3-6 PBO Simulation of rotational misalignment .....	49
Figure 3-7. Effect of lens 2 rotation upon beam size. ....	50
Figure 3-8. (a) Before and (b) After alignment. Higher order rotational aberration: (c) before and (d) after correction.....	50
Figure 3-9. Correction for rotational misalignment by fine tuning lens 3 rotation .....	51
Figure 3-10. Optimal focus after quadrupole alignment. (a) Off-axis scanning transmission ion microscopy images of the Ni resolution standard with ( $a_x, a_y$ ) extracted line scans by adding 200 neighbouring pixels. (b) Secondary electron image acquired using MCP with ( $b_x, b_y$ ) showing extracted line scans by adding 120 neighbouring pixels. Images (a) and (b) were taken with scan size of $5 \times 5 \mu\text{m}^2$ .....	52
Figure 3-11. a) CAD Drawing of the motor housing made with aluminium profiles. Bottom motor is placed inverted due to space constraints. b) Housing	

with the motors mounted and coupled to the micrometres using 3D-printed gears.....	54
Figure 3-12. Study of micrometre backlash. Micrometre was moved by single step each time and beam current measured.....	55
Figure 3-13. Magnetic field intensity along the motor shaft axis .....	56
Figure 3-14. Computer interface to the stepper motors .....	57
Figure 3-15. Automated alignment algorithm flowchart .....	57
Figure 3-16. Control Interface written in LabVIEW 2011 .....	58
Figure 3-17. a) Defining Beam Shape in objective slit (step 2, Figure 3-15). A rectangular aperture is defined in objective slit after this step. b) Reducing objective size as per step 4i in Figure 3-15.....	59
Figure 3-18. Objective slit alignment as per step 4ii in Figure 3-15. Slits are scanned with fixed opening till the maximum current position is found in both X & Y directions. Scan step size and direction are reduced and reversed respectively with negative beam current gradient .....	60
Figure 3-19. Control Interface developed in LabVIEW 2011. Shown are all the tabs with different functionality.....	61
Figure 3-20. Layout of data acquisition for PBW.....	61
Figure 3-21. Automated Scan size calibration. (a) Scan calibration in X direction with 1 $\mu\text{m}$ stage motion corresponds to 31-pixel difference in the edge position (120-89) resulting in Pixel size of 32 nm. Calculated X FWHM = 262 nm; (b) Scan calibration in Y direction with 1 $\mu\text{m}$ stage motion corresponds to 29-pixel difference between the edge locations (105-76) at a Pixel Size of 34.5 nm and calculated Y FWHM of 448 nm. ....	64
Figure 3-22. Rough Focusing using STIM Image and manually adjusting quadrupole lenses.....	65
Figure 3-23. STIM Image of Ni Resolution standard after autofocusing with objective and collimator opening of $30 \times 20 \mu\text{m}^2$ and $60 \times 60 \mu\text{m}^2$ respectively. ....	67
Figure 3-24. Off-axis STIM image of Ni resolution standard images using $800 \times 800 \text{ nm}^2$ scan area at 256-pixel resolution.....	69
Figure 3-25. Lithography tab from the interface for step and repeat, and stage scan .....	70
Figure 3-26. Effect of stage velocity on pattern writing in resist. Non-overlapping beam scans lead to gaps in resist region expected to be exposed. ....	72
Figure 3-27. Gap spacing and frequency observed in PMMA after development.....	74
Figure 3-28. On-axis STIM image of Ni resolution standard.....	75
Figure 3-29. SEM image of developed cross written at dose of $240 \text{ nC/mm}^2$ .76	76
Figure 3-30. SEM images of Au grid. (a) Full grid image showing the portion of grid folds on itself due to stress owing to poor support from the Ni frame. (b) and (c) shows high resolution images of the bottom right corner of the resolution which can be used to focus ion beams using STIM and Secondary electrons. ....	78
Figure 3-31. Thickness measurement of Au grid using method described in section 2.3 .....	79
Figure 3-32. Collection efficiency of MCP as a function of bias voltage .....	81
Figure 3-33. Collection Efficiency as a function of bias voltage applied to the front plate for increasing incident beam energy .....	84

Figure 3-34. (a) MCP image for 500 H <sub>2</sub> <sup>+</sup> (350 V bias, 2800 V accelerating voltage, 3800 cps). (b) On-axis STIM image of the same spot .....	85
Figure 4-1. Fabrication flow of a nanograting in PMMA.....	89
Figure 4-2. Figure schematic for the step and repeat algorithm .....	90
Figure 4-3. Nanograting (200 nm channels and 300 nm spacing) fabricated using Step and repeat algorithm. A field of 100 $\mu\text{m} \times 100 \mu\text{m}$ is scanned for grating and the stage is stepped 100 $\mu\text{m}$ for writing the next field.....	91
Figure 4-4. Schematic of nanograting (300 nm channels and 200 nm spacing) .....	93
Figure 4-5. Fabricated Nanograting using step and repeat (full device view).93	
Figure 4-6. 30 nm channels in PMMA. 30 nm Channels in 2 $\mu\text{m}$ PMMA, 2MeV protons written using 85 nC/mm <sup>2</sup> .....	94
Figure 4-7. Ni lines after stripping PMMA. 40 nm ridge are seen in the image on the left, 50 nm ridges shown on the right at a dose of 285 nC/mm <sup>2</sup> .....	95
Figure 4-8. (a) 30 nm channels in 2 $\mu\text{m}$ PMMA, 2MeV protons written using 100 nC/mm <sup>2</sup> , 1 $\mu\text{m}$ Ni Plating – image after removing PMMA (b) Ni under-plating of 500 nm at the base .....	97
Figure 4-9. (a) 200 nm (2 pixel) channels in 2 $\mu\text{m}$ PMMA and (b) 320 nm channels (9 pixels) written using 2MeV protons written using 200 nC/mm <sup>2</sup> and 120 nC/mm <sup>2</sup> respectively (500 nm and 1 $\mu\text{m}$ pitch grating).....	98
Figure 4-10. Nanograting in 2 $\mu\text{m}$ thick PMMA. Optical image of the sample after development. Channel width (pixels) and Dose (nC/mm <sup>2</sup> ) is superimposed on the image for every region between grid bars. ....	99
Figure 4-11. SEM image of the developed sample with the full field showing the grating areas within the grid windows .....	99
Figure 4-12. 30 nm Cu lines on Si after PMMA stripping. Inset shows the line scan of 174 nm line widths. ....	101
Figure 4-13. SEM image of full area written using step and repeat .....	103
Figure 4-14. (a) 44 nm line, 70 $\mu\text{m}$ long; (b) 44 lines, 3 $\mu\text{m}$ spacing and 70 $\mu\text{m}$ long .....	104
Figure 4-15. Lines written using stage scan showing the gaps left due to non-uniform stage motion .....	105
Figure 4-16. Optical image of the HSQ lines aligned with the DWL micro lines. (b) Features transferred to Ormostamp after two copies showing Ormostamp ridges .....	105
Figure 4-17. Linewidths of 250 nm, 170 nm and 100 nm in HSQ shown in high resolution SEM images and full area features used for the experiment on the left .....	108
Figure 4-18. 30 nm pillars (a), 50 nm pillars (b) .....	110
Figure 4-19. Pillar size vs Dose written using beam of 2 MeV H <sub>2</sub> <sup>+</sup> focused to 23 nm $\times$ 32 nm .....	110
Figure 4-20. 50 nm lines (left) and 33 nm lines (right) using the same beam as pillars.....	112
Figure 4-21 Line width vs log dose .....	112
Figure 4-22. Pillars written using 1 MeV Alpha in HSQ. (a) 100 $\times$ 200 nm <sup>2</sup> pillars written at 1000 He <sup>+</sup> /pillar ( $\sim$ 53 nC/mm <sup>2</sup> ). (b) 200 $\times$ 200 nm <sup>2</sup> pillars written using 6500 alpha/pillar ( $\sim$ 346 nC/mm <sup>2</sup> ) .....	113
Figure 4-23. 200 nm lines and 100 nm spacing written by overlapping spot irradiation in Y direction at a dose of 5000 ions/pillar .....	114

Figure 4-24. On-axis STIM Image of Ni resolution standard. Also shown are the line scans extracted from the image showing a focus of $17 \times 102 \text{ nm}^2$ ...	115
Figure 4-25. 100 nm channel etched in Si. (a) plan view SEM of a 100 nm wide channel with a 1 MeV proton fluence of $2 \times 10^{16}/\text{cm}^2$ . (b) Cross-section SEMs of similar channel as in (a), showing (right) the full anodized depth beyond the end-of-range at 15 $\mu\text{m}$ and (left) the top 5 $\mu\text{m}$ where a channel width of 150 nm is produced .....	116
Figure 4-26. SEM image of the waveguides in STO .....	117
Figure 4-27. Line width and pitch matching the target stage motion .....	117
Figure 5-1. Mask and Sample geometry defined in Geant4. Also shown are 200 keV alpha ions incident on the mask plane from left. Scattering of the ions can be observed through the mask and further transmission through 400 nm thick PMMA layer kept right after Ni.....	127
Figure 5-2. Projected range comparison from SRIM and Geant4 in Ni for helium in the energy range of 10 keV to 2000 keV .....	128
Figure 5-3. Range and scattering of 200 keV Alpha plotted in 1 $\mu\text{m}$ thick Ni from Geant4 (left) and SRIM (right) .....	129
Figure 5-4. Edge scattering from the 60 nm aperture with a point beam of 200 keV alpha positioned 2 nm from the aperture edge. ....	131
Figure 5-5. Edge scattering from the aperture edge with beam centre varied from 2 nm to 100 nm .....	132
Figure 5-6. Escape probability of ions from the aperture with point beam centre moved away from the aperture edge. ....	133
Figure 5-7. Scatter plot (a, c) and energy maps (b, d) shown for 2 nm (a, b) and 20 nm (c, d) from the aperture edge respectively.....	134
Figure 5-8. 200keV alpha transmission through a 60 nm aperture. (a) scatter plot, (b) energy map at the PMMA surface. ....	135
Figure 5-9. Line profile of the scattered ions on the surface of PMMA after transmission through the 60 nm aperture defined in Ni mask. ....	135
Figure 5-10. Geometry of two 60 nm lines spaced 500 nm centre to centre in Geant4.....	136
Figure 5-11. Edge scattering from the top 60 nm line with the point beam positioned at the edge of the line at varying distance. ....	137
Figure 5-12. Edge scattering of 200 keV alpha landing on the PMMA surface. (a, c) shows the scatter plots and (b, d) images show the energy maps for the beam positioned at 2 nm from the edge and 20 nm respectively from the edge. ....	138
Figure 5-13. Escape probability of 200 keV ions at varying distance from the edge of the line. ....	139
Figure 5-14. Scatter plot (a, c) of ions reaching the PMMA surface for 60 nm lines spaced 500 nm apart. Also shown are the energy maps (b, d) at the fluences for (a, b): $10^5$ ions; (c, d): $10^6$ ions .....	140
Figure 5-15. Effect of beam divergence on the energy spectrum of ions reaching the PMMA surface .....	141
Figure 5-16. Scatter plot (a) and Energy map (b) for an incident beam divergence of 1 mrad .....	142
Figure 5-17. Line width variation as a function of incident beam divergence .....	142
Figure 5-18. Line width vs beam tilt with respect to the mask-sample stack. ....	143

Figure 5-19. Energy spectrum of transmitted ions through the 60 nm lines at varying incident beam angle .....	144
Figure 5-20. Scatter plot and energy map on the PMMA surface with beam tilt to 3.43 ° .....	144
Figure 5-21. Effect of gap between mask and sample plane. ....	145
Figure 5-22. Pattern transfer of 250 nm aperture on the PMMA surface with irradiation of 200 keV alpha. (a) scatter plot and (b) shows the energy plot. ....	146
Figure 5-23. Simulation of ion transmission through a 10 nm aperture;(a) scatter plot and (b) energy map.....	147
Figure 5-24. Simulation of 10 nm lines and spaces in 1 μm thick Ni. ;(a) scatter plot and (b) energy map.....	147
Figure 5-25. Simulation of 60 nm line and spaces in 1 μm thick Ni; ;(a) scatter plot and (b) energy map .....	148
Figure 6-1.Sample for mask fabrication in maN 2410 and Ni plating.....	151
Figure 6-2. SEM images of pillars turned lines in ma-N shown after Ni plating .....	152
Figure 6-3. EPL layout for scanning. Shown are two grating pitches 1 μm (right) and 5 μm left.....	153
Figure 6-4. SEM image of full area of the grating written in ma-N 2410 after development. Dose increases from right to left and line width increases from top to bottom. $D_M = 300 \text{ nC/mm}^2$ and $D_N = 20 \text{ nC/mm}^2$ .....	154
Figure 6-5. SEM image of 230 nm linewidth in ma-N after development written using 3 pixels .....	155
Figure 6-6. Grating in PMMA after development. showing line width of 200 nm .....	155
Figure 6-7. Ni lines of 200 nm at varying pitch of 500 nm to 5 μm from top to bottom. Lines were resolved in PMMA and written with stage scan. Gaps in the lines are seen which result from non-uniform stage motion.....	156
Figure 6-8. 250 nm wide apertures 50 μm long in Ni after stripping ma-N 2410 in acetone. (a) shows the grating with 5 μm pitch; (b) shows a high resolution of the 250 nm opening in 1 μm thick Ni before Cu etching .....	157
Figure 6-9. 300 nm gap in Ni masked by cross-linked ma-N which is harder to be removed in Acetone .....	158
Figure 6-10. Mask features showing 60 lines in Ni after ma-N stripping but before Cu etching. (a) 500 nm spaced lines 60 nm wide at the edge of the grating region due to ma-N adhesion. (b), (c) and (d) shows 60 nm lines in Ni left after electroplating due to ma-N adhesion loss during Ni electroplating. ....	159
Figure 6-11. Mask with electroplated frame around to ease handling.....	160
Figure 6-12. SEM image of (a) 69 nm linewidth in PMMA written with a beam of 200 keV He <sup>2+</sup> at a dose of 2.5 nC/mm <sup>2</sup> . (b) 269 nm channels written with 250 nm aperture in Ni .....	163
Figure 6-13. SEM image of (a) 69 nm linewidth and (b) 314 nm linewidth in 400 nm thick PMMA written with a beam of 200 keV He <sup>2+</sup> at a dose of 9.5 nC/mm <sup>2</sup> .....	163
Figure 6-14. 260 nm lines reproduced in PMMA layer written with a beam of 200 keV He <sup>2+</sup> at a dose of 9.5 nC/mm <sup>2</sup> .....	164

# List of abbreviations

<b>ITRS</b>	International Technology Roadmap for Semiconductor
<b>DRAM</b>	Dynamic Random Access Memory
<b>PMMA</b>	Poly-methyl methacrylate
<b>HSQ</b>	Hydrogen silsesquixane
<b>EBL</b>	Electron Beam Lithography
<b>FIB</b>	Focused Ion Beam
<b>HIM</b>	Helium Ion Microscope
<b>PBW</b>	Proton Beam Writing
<b>IPL</b>	Ion projection Lithography
<b>PPAL</b>	Programmable Proximity Aperture Lithography
<b>MIBL</b>	Masked Ion Lithography
<b>RF</b>	Radio-frequency
<b>DAQ</b>	Data Acquisition and Control
<b>TTL</b>	Transistor-Transistor Logic
<b>AO</b>	Analog Output
<b>PBO</b>	Particle Beam Optics
<b>FWHM</b>	Full Width Half Maximum
<b>STIM</b>	Scanning Transmission Ion Microscopy
<b>MCP</b>	Microchannel Plate
<b>PXI</b>	PCI eXtensions for Instrumentation
<b>SEM</b>	Secondary Electron Micoscopy
<b>DI Water</b>	De-ionized water
<b>IPA</b>	Isopropyl Alcohol
<b>SRIM</b>	Stopping Range of Ions in Matter
<b>GEANT4</b>	Geometry and Tracking

# 1 Introduction

## 1.1 Overview of nanofabrication

Integrated circuit fabrication has pushed the limits of lithography down to sub 20 nm using techniques such as immersion lithography [1][2] combined with resolution enhancement techniques such as optical proximity correction [3], phase shift mask development [4] and double patterning [5]. ITRS 2015 [6] extended the roadmap with expected gate length of DRAM shrinking to sub-10 nm. Fabrication in the industry now, is dictated by the demand for consumer electronic products. To achieve the demand for fabrication at single digit nanometre length scale, next generation lithographic methods have begun to make progress [7][8][9]. Fabrication of smaller features lead to increase in device density per die. However, deviation from classical device characteristics at smaller length scales are detrimental to the performance of classical CMOS architecture. Alternative methods such as design of high-k gate dielectric materials, change in the circuit layout and device architecture namely FINFETs [10] and Gate-all-around transistors are implemented to overcome these deviations. A major aspect of fabrication of these complex features will require the development of exposure sources to reach high volume manufacturing at reduced cost and transition to more than Moore era. In addition to the source requirement, metrology [11] and mask fabrication [12] pose further challenges towards achieving high performance devices.

Apart from the commercial application in semiconductor industry which requires parallel exposure and multiple mask layer exposures, research in the domain of material modification at nanoscale has already picked pace.

Emerging applications such as fluidics [13][14] and lab-on-chip techniques reduces the consumables at higher sensitivity and throughput [15][16]. Higher density heat assisted magnetic recording [17] to modern architecture with bit pattern media where each bit is lithographically defined to attain density of  $>1\text{Tb/in}^2$  [18] has led to the advancement in memory architecture. Novel implementation towards non-volatile memory [19] and development of racetrack memory [20] which uses magnetic domain wall motion to store media are advancing the device architecture to three dimensions.

Behaviour of materials at nanoscale is significantly different from their bulk counter parts which offers avenue to advance the progress made in various disciplines. Nanofabrication lies at the core of harnessing the advantages of materials at nanoscales. Here we briefly review techniques which are employed to modify material characteristics.

## 1.2 Resist materials for nanofabrication

Resists are radiation sensitive materials which can be coated on substrates and modified locally to yield desired patterns. Based on the nature of the interaction with the exposure method, they are broadly classified as positive and negative resists. Positive profile resists are the photosensitive materials which show higher rate of etching of exposed regions with a compatible solvent post-exposure. On the other hand, negative resists are the photopolymers which show low etching rate of exposed regions in developers after exposure. Two of the most common and high-resolution photoresists used for nanofabrication are PMMA and HSQ.

### 1.2.1 PMMA

Poly-methyl methacrylate (PMMA) is an organic chain molecule that polymerizes to form longer chains. Molecular weights for the chains ranges from 100k g/mol to 3M g/mol. Figure 1-1 shows the chain of PMMA molecule.

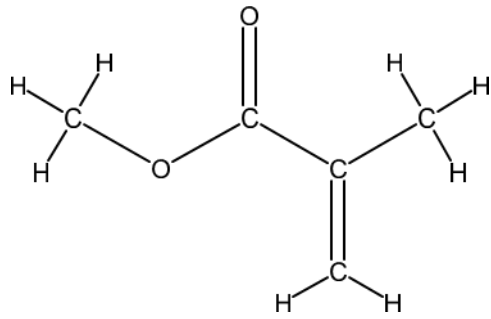


Figure 1-1 Molecular structure of PMMA monomer

PMMA is a transparent material with absorption wavelength of <260 nm. Characteristics of PMMA upon irradiation with various lithographic techniques, studied in [21], found the backbone chain scission to linearly increase with the exposure dose. Besides, the degradation path through backbone chain scission was found to be an order of magnitude higher for high energy charged particles in comparison to deep UV exposures. It also highlighted that the number of chain scission in the molecule was higher for protons than electrons. Exposed PMMA is developed using developer mixtures such as MIBK:IPA, IPA:DI water or GG-developer.

### 1.2.2 HSQ

Hydrogen silsesquioxane is an inorganic resist material that acts as negative resist upon exposure of charged particles. HSQ is transparent to DUV and only exposes in the x-ray or lower wavelengths. The structure of HSQ [22] is shown in Figure 1-2. Post irradiation the cages are crosslinked making it insoluble in

the developer. Common developers for HSQ are TMAH, KOH and salty-developer such as aqueous mixture of NaOH and NaCl [23].

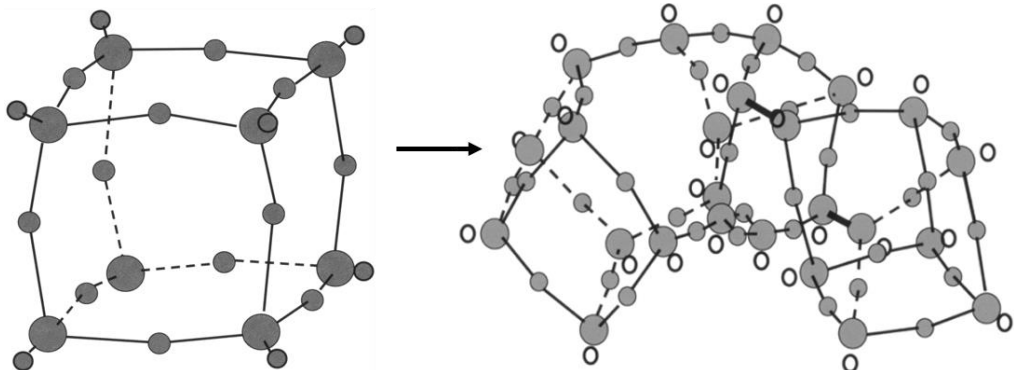


Figure 1-2. Crosslinking of HSQ leading to formation of cage

### 1.2.3 Characterization of photo-resist

Resist contrast is a measure of sensitivity and the response to a dose variation of a lithographic process. Positive or negative resists such as PMMA and HSQ are compared and studied based on the gradient of thickness left after exposure to the dose required. For a positive resist, remaining thickness is plotted as a function dose deposited. Figure 1-3 shows an example contrast curve for HSQ denoting effect of delayed exposure [24]. Contrast ( $\gamma$ ) defined as the slope of the linear range of the H-D profile as  $\gamma = \left( \log \frac{D_f}{D_i} \right)^{-1}$ , where  $D_f$  and  $D_i$  are the exposure doses at which resist is insoluble and completely soluble for a negative resist respectively.

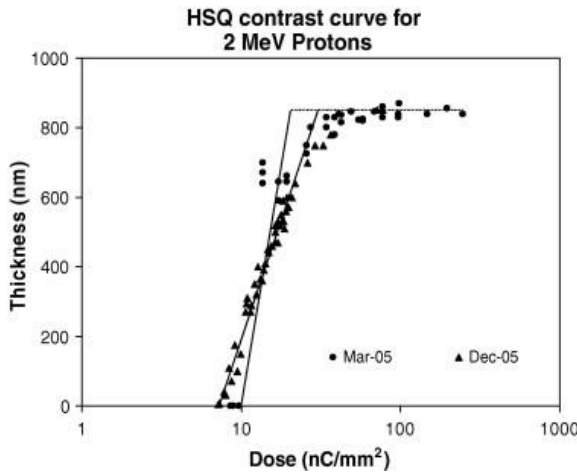


Figure 1-3. Contrast curve measured for 2 MeV protons at two different exposure timings

Several factors affect resist contrast for the lithographic technique used for fabrication. As can be seen from Figure 1-3, contrast of the resist changes with delay between coating and exposure. Contrast in different resists has been compared for both electrons and protons [21][25]. The sensitivity of protons is two orders higher than electrons in PMMA. Other effects such as temperature of developer [26], development time and type of photoresist are other factors that influences resist contrast [27].

### 1.3 Techniques for lithography

#### 1.3.1 Photolithography

A high throughput nanofabrication technique employed by the semiconductor industry is photolithography. It uses a light source that is adjusted to emit collimated light beam of wavelength,  $\lambda$ , onto a photomask upon which features are drawn in Cr layer on top of a quartz base. As per Rayleigh's criterion for diffraction from a slit, the resolution of two features that can be resolved is dependent on the wavelength of the light source and numerical aperture of the lens used to expose the photo resist.

$$\text{Res.} = \frac{\lambda}{2n\sin\theta} \quad (1.1)$$

Resolution of this technique is limited by the wavelength of light source used, distance between mask and polymer and the refractive index of the medium in between the lens and sample mask stack. To improve the resolution, it is thus required to reduce the wavelength of light source used and increase the numerical aperture used. Besides, other techniques such as Phase shift mask [28], where the phase of the light transmitting through the mask is inverted to give interfering patterns on the polymer surface have been used to push the limits down to 45 nm. Techniques such as Litho-Etch double and triple patterning has shown reduction in the linewidth or feature sizes through clever process designs for the 14 nm node [29][30][31]. EUV sources are still under development and require modifications of the exposure optics needed such as reflective masks instead of absorbing masks. Fabrication of features down to 20 nm requires precise fabrication of masks with optical proximity corrections [29]. Fabrication of these masks is carried by using electron beam lithography.

### 1.3.2 Electron beam lithography (EBL)

Electron beam lithography (EBL) corresponds to the technique where energetic electrons emitted from high brightness sources are focused down to sub nm spot sizes and scanned over photoresist materials [32]. Resolution of electron beam lithography in photoresists is not limited by diffraction because of the smaller de Broglie wavelength  $\lambda$ .

$$\lambda(\text{nm}) \approx \frac{1.23}{\sqrt{V}} \quad (1.2)$$

Where  $V$  is the electron energy in eV. Electrons accelerated beyond energies of 1 keV will have de Broglie wavelength less than 38.7 pm. However, a primary incident electron can interact with the substrate electrons in elastic and inelastic collisions. Elastic collisions result in incoming electrons scattering away from the primary trajectory and inelastic collisions lead to ionization and excitation of target atoms. Energy transferred in inelastic collisions, result in generation of secondary electrons which can travel longer distances from the track of primary particles [33]. Furthermore, at the resist-substrate interface, backscattering of electrons leads to broadening of the feature width which is known as proximity effect. Resolution in photoresist is thus limited by the proximity effect [34], [35]. EBL has matured into an effective sub-10 nm lithographic technique by implementing measures to correct proximity effect [36], process optimization [37], exposure strategy [38] and resist development [39][40]. For instance, EBL has demonstrated ability to fabricate sub 5 nm features in both HSQ [23] and PMMA using cold development [41]. Moreover, 1.7 nm isolated holes have been fabricated in PMMA using aberration corrected EBL [42]. High aspect ratio nanostructures have also been fabricated with EBL in PMMA [43]. EBL is used for mask fabrication in photolithography using techniques such as variable shaped beam [44], [45] and multi-beam approaches [46] to increase the throughput.

### 1.3.3 Ion beam lithography

#### 1.3.3.1 Focused ion beam lithography (FIB)

Heavy ions, such as Ga, accelerated to energies in the range 5-30 keV, can be focused down to single nm spot sizes [47]. Heavy ions transfer kinetic energy to substrate atoms leading to sputtering of neutral or charged species.

Applications of FIB include mask repair for photolithography [48], [49], implantation to create etch stop regions in wet etching [50], [51] and preparing thin sections for Transmission Electron Microscopy [52]. The major limitation of the technique is re-deposition of sputtered substrate atoms at the sidewalls as the depth of etching is increased [53].

With the development of helium ion sources of higher brightness, sub-nm spot sizes have been demonstrated which has been useful in imaging materials at sub-nm resolution [54], [55]. Low energy helium ion can be used just as in EBL to define features in the photoresist layers that can later be resolved using a developer mixture. Sub-10 nm features have been demonstrated using scanning helium ion beam in HSQ [56], [57].

### 1.3.3.2 Proton beam writing (PBW)

MeV protons propagating through materials interact mostly by electronic scattering while a smaller fraction interacts by end of the range nuclear scattering [58][59]. Protons, being relatively higher in mass than substrate electrons ( $\approx 1800:1$ ), can travel in a straight path leaving a uniform energy loss trail [60], [61]. Proton beams, focused to nanometre dimensions, have demonstrated fabrication of orthogonal [62] and high aspect ratio structures [63] in photoresist with low sidewall roughness [64]. Features down to 19 nm have been fabricated in HSQ using PBW technique [65]. This technique is also serial in nature and relies on low brightness ion sources as well as depends on the energy stability of the accelerator to achieve sub-10 nm spot sizes. The reduced brightness  $B_r$ , for the ion source is calculated as

$$B_r = \frac{I(pA)L^2(m^2)}{A_{object}(\mu m^2)A_{collimator}(mm^2)E(MeV)} \quad (1.3)$$

where I is the beam current measured in pA,  $A_{objective}$  and  $A_{collimator}$  are the objective and collimator aperture openings, L is the distance between the objective aperture and the collimator aperture, and E is the energy of the ions.

Projection techniques employing high resolution of ion beam lithography have been implemented to increase throughput. For instance, Ion projection lithography (IPL) [66] projects a demagnified image of a stencil mask using ion optics onto the sample plane. Features down to 70 nm have been fabricated using this technique [67]. A programmable proximity aperture lithography (PPAL) system has also been developed which uses apertures to define the beam shape down to 100 nm [68], [69].

#### 1.3.4 Soft lithography

Higher throughput can be achieved by mask or mold fabrication using serial writing techniques such as FIB, EBL and PBW described above. The resist features are transferred to a master using electroplating [70], [71] or directly used as stamps [72]. The master can then be stamped on soft polymers close to the glass transition temperatures. Feature sizes down to 10 nm have been shown using this nanoimprinting technique [73].

#### 1.4 Interaction of charged particles with photoresist

Energetic ions passing through a material interacts with the substrate atoms and electrons. Due to coulombic interaction, the ion loses energy through various elastic and inelastic collisions. The rate of loss of energy through the depth of penetration in material is referred to as linear energy transfer or stopping power.

Linear energy transfer or stopping power can be split into two components. The first aspect refers to the energy loss of ions due to elastic scattering with the substrate nucleus. Multiple collisions lead to small angle scattering of the incident ion well before the end of the range in material. However, for thicker materials (thickness > range), the ions lose more energy close to the end of the range and eventually stopping in the material. As the ion gets slower towards the end of the range, it spends more time in the proximity of substrate nucleus thereby leading to a faster rate of energy loss. The second energy loss component is the inelastic collision with the substrate electrons. Owing to mass and momentum mismatch compared to electrons, ions travel in straighter paths and loses minimal energy to the substrate electrons. Electronic energy loss is an order higher in magnitude than nuclear energy loss for thin resist layers due to higher scattering cross-section for the ion collisions with substrate electrons than nucleus. Moreover, the energy loss is uniform throughout the depth for thin photo resists. The electronic energy loss goes towards generation of secondary electrons through ionization and excitation mechanisms. Ion induced secondary electrons travel almost perpendicular to the ion track due to lower mass and carry energy typically  $<20$  eV. These secondary electrons lead to generation of electron cascades till electrons come to rest in the material. The electrons generated in the cascade lead to chemical changes in the photo-polymers such as bond-scission or cross linking of chains.

The extent of the secondary electrons and the cascade have been studied both analytically using simple track approximation [74] as well as event by event Monte Carlo simulations. Udalagama *et. al.* [60], [61] reported the comparison between energy density profile in PMMA for proton and electron irradiation.

Figure 1-4 shows the energy deposition profile of protons and electrons at three different energies used typically for lithography. Dapor et. al. [75] recently reported event by event Monte Carlo simulation using dielectric response function showing a decline in the radial dose to  $\sim 10$  nm in PMMA for all the energies up to 100 keV. They concluded the optimum energy to be 100 keV for lithography.

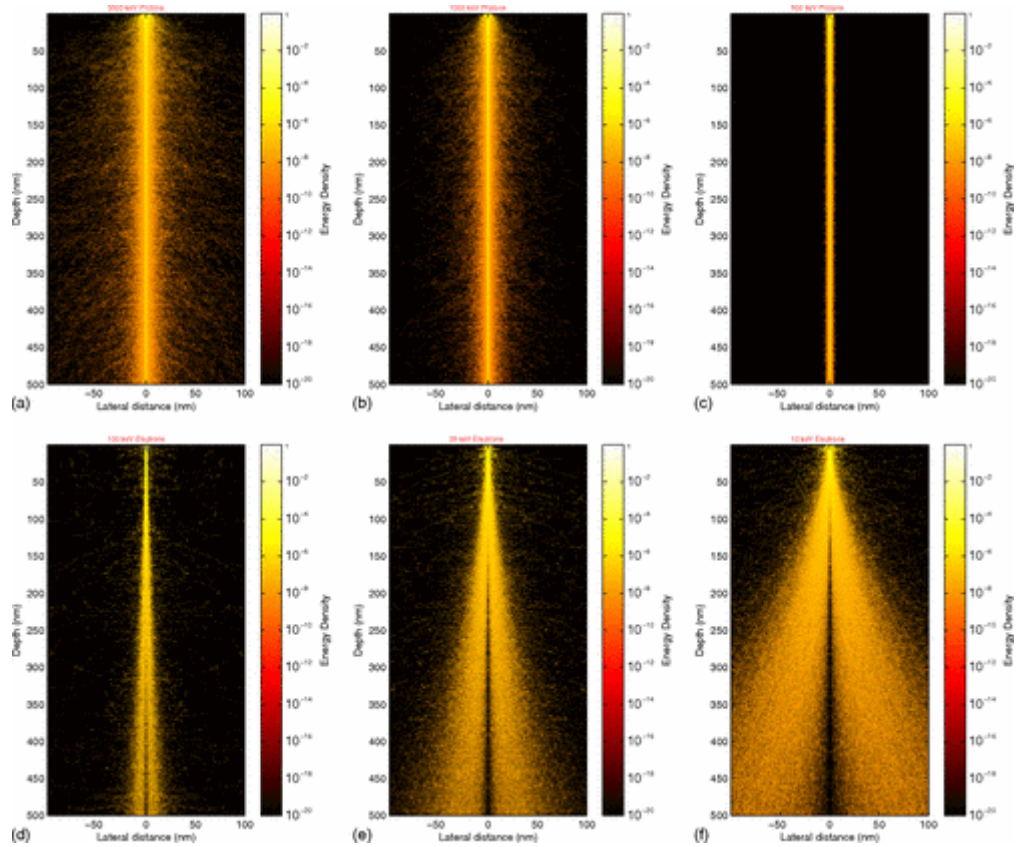


Figure 1-4. Spatial energy density map for protons and electrons

The range of these secondary electrons were shown to be well within 10 nm of the proton tracks both from analytical and simulation results.

van Kan *et. al.* [76] estimated the radial energy spread of a 2 MeV proton beam in PMMA. The results of this study concluded a spread of less than 100 nm for depths of 100  $\mu\text{m}$  in PMMA whereas the effect of delta ray electrons extend to

32 nm at a depth of 20  $\mu\text{m}$ . While results for patterned structure will be reviewed in the following section, it is worthwhile to note that maximum aspect ratio allowed for EBL was demonstrated experimentally with accompanying simulations. Figure 1-5 shows a cross-section image of 100 nm channels fabricated in 3  $\mu\text{m}$  thick PMMA sample using EBL. The channel size increases from 100 nm to 300 nm to a depth of 3  $\mu\text{m}$  leading to a maximum aspect ratio of 14 [77].

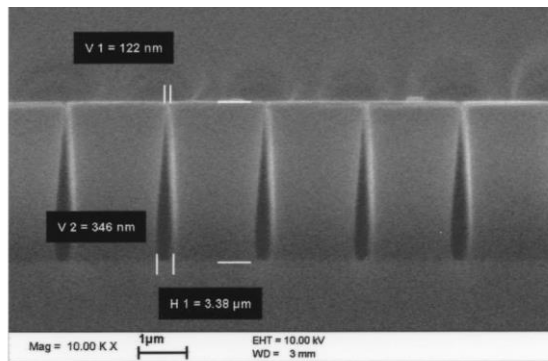


Figure 1-5. Fabrication of nanochannels in 3  $\mu\text{m}$  thick PMMA using EBL  
(figure taken from [77])

### 1.5 Applications of proton beam writing

Features such as uniform energy deposition, straight trajectory and proximity free lithography make proton beam writing an ideal candidate for precise nanofabrication. van Kan *et. al.* [78] showed 3D high aspect ratio lithography using protons in SU-8 and PMMA. Line width of 60 nm was achieved in 10  $\mu\text{m}$  thick SU-8. Line widths of 30 and 50 nm were patterned in PMMA of 350 nm and 250 nm thicknesses respectively. Fabrication of these grooves in PMMA shows that proximity free writing in photoresist during PBW is possible.

Proton beam writing has been successfully employed for the following applications:

### 1.5.1 Nanoimprinting

Proton beam writing has demonstrated fabrication of smooth and vertical sidewall with measured surface roughness as low as 3 nm [79]. Higher throughput for nano-replication can be achieved using nanoimprinting. This technique employs replication of a master mold fabricated in photoresist using PBW in soft polymers. Lithographically defined patterns in resist have been transferred to metal stamp using Ni electroplating. High aspect ratio masters with features down to 100 nm have been fabricated and used for imprinting [70], [80]–[82]. Besides electroplating, high resolution mold patterned in HSQ with details down to 30 nm have been replicated in OrmoStamp using a double transfer [72]. Enclosed nano-channels in PDMS with cross-sections of 100 nm was demonstrated using imprinting and thermal bonding [83]. Master stamps fabricated using a programmable aperture plate system with resolution down to 20 nm in HSQ were transferred to PDMS [84].

### 1.5.2 Micro/Nanofluidics

High throughput of PDMS nanochannels [85] were demonstrated to cross-sections of 100 nm x 60 nm using proton beam written master replication in HSQ and SU-8. Herein, the extension of DNA molecule was shown to increase with the reduction in the channel dimension. Fabrication of closed microchannels in SU-8 after development was shown by two consecutive overlapping tilted exposures with focused protons to generate a closed lambda structure [86].

Nanochannels fabricated using PBW and UV lithography [87] were used to study dynamic response of DNA compaction and unpacking in response to in-

situ change of buffer concentration. DNA confined in nanochannels showed increasing extension in response to narrow channel widths of 80 nm [88].

A combined UV and PBW procedure was demonstrated towards fabrication of closely spaced high aspect ratio nickel electrodes [89]. Uniform field distribution between the electrodes lead to higher transfection for single cell electroporation. Lab-on-chip device fabricated using PBW and PDMS casting was used to demonstrate separation of superparamagnetic particles down to 130 nm sizes [90].

### 1.5.3 Photonics

PBW can be applied to fabricate micro/nanostructures of interest in photonics such as lens array, grating and arbitrary templates for direct self-assembly [91]. Material damage at the end of the range locally changes the refractive index. This characteristic leads to formation of buried waveguides. PBW with 1  $\mu\text{m}$  spot size was used to fabricate erbium-doped waveguide amplifiers [92]. Channel waveguides can also be fabricated using masked ion irradiation [93]. Micro lenses in PMMA were fabricated by exposing the sample using a Nickel mask and selectively diffusing MMA monomers in the irradiated areas [94]. This leads to swelling of the irradiated region thereby making spherical protrusions of the sample surface which can then be used for optics application.

Optimization of a synchronized line scanning was demonstrated for PBW of long and arbitrary structures [95]. This technique was employed to fabricate Mach-Zehnder modulator featuring identical arms with absence of phase change due to length mismatch. PBW demonstrated fabrication of high aspect

ratio metamaterial using electroless plating [96] and polymer microlaser with suspended cavity [97].

Proton beam writing was optimized in Forturan and CR-39 type solid state nuclear track detector [98]. A change in the refractive index of the material post exposure allows for applications such as microphotonics. Fluences as low as 1 nC/mm<sup>2</sup> were sufficient to etch the exposed regions in HF for microchannels.

Exhibiting the higher sensitivity for ions when irradiating Forturan, doses as low as 0.25 nC/mm<sup>2</sup> were used to expose and create buried channels in the sample [99]. However, a full etching was achieved with a 1 nC/mm<sup>2</sup> dose for a 2.5 MeV proton beam.

The lift-off process imposes a limitation on the critical dimension and thickness achievable for TiO<sub>2</sub> layers. Directly patterning TiO<sub>2</sub> is advantageous for applications spreading over solar cell, optical waveguides, gas sensors and electrochromic displays. Using a sol-gel based spin coatable TiO<sub>2</sub> resist for PBW developed in acetone for 60 s shows negative behaviour [100]. A contrast value of 2.3 was obtained for 2 MeV protons with a sensitivity of 3000 nC/mm<sup>2</sup>.

End of the range energy deposition in diamond leads to graphitization of the substrate. This property can be used for making sensors integrated in diamond substrate. Picollo *et. al.* [101] showed fabrication of micro strips which exhibited graphitization using Deep Ion Beam Lithography. A contact masking via thick Cu deposition (4  $\mu$ m) and micro patterning using tapered thickness across the edge of the strips to allow graphitization till the surface. A broad 1.8 MeV helium beam was used to irradiate the micro-aperture in Cu mask. The

damage profile showed ohmic behaviour marking the formation of graphite layer buried in diamond.

#### 1.5.4 Silicon micromachining

Energetic ions incident on Si create defects at the surface to the end of the range. Defect density created along the trajectory of ions increases the resistivity which offers a differential etching rate in subsequent electrochemical etching[102], [103]. Ion irradiation combined with electrochemical etching has been employed to fabricate micro/nanostructures in porous Si. Multi-level cross structures and high aspect ratio nano-tips have been fabricated in Si down to 15 nm at the tip surface [104]. Fabrication of 3D nanostructures with masked ion lithography and electrochemical anodization have shown fabrication of 100 nm structures in porous Si [105]. Photonic crystals in mid-infrared range have been fabricated in porous Si [106] towards silicon-based photonic circuits. Buried nanochannels have been fabricated in Si using PBW for Lab-on-chip application [107].

#### 1.5.5 High resolution resists

An epoxy resist [108] was tested for PBW using 2 MeV proton beam focused down to 2-3  $\mu\text{m}$ . This resist showed a resolution of 5  $\mu\text{m}$  and negative behaviour. The epoxy resist was proposed as an alternative to SU-8 resist, which is hard to remove after crosslinking. A 35  $\mu\text{m}$  thick Epoxy resist was developed in TMAH and stripped in acetone after 30 mins of sonication.

Polytetrafluoroethylene (PTFE) microstructures have been fabricated using 3 MeV proton beam in air under different gaseous environments as well as vacuum [109]. This study showed beam induced etching as a function of fluence

but independent of the ion energy. Samples processed in air showed etched micro holes in various gaseous environment. However, irradiation under vacuum showed protrusions of the samples in the exposed regions. The method was later optimized in an oxygen rich environment [110] which led to a burr free etching or micromachining with no re-deposition at the edges due to the formation of stable gaseous compound following beam induced decomposition.

Melting of PMMA during proton exposure was studied [111] using a 2 MeV proton beam exposed on to a 50  $\mu\text{m}$  PMMA film. Four regions of exposure were noticed - underexposed, change of refractive index, partially melted and completely melted which were observed from the interferometric images of the exposed PMMA post exposure.

Based on the higher sensitivity of resists for ions, resolution of single ions can be experimentally validated by single ion beam lithography. Alves *et. al.* [112] exposed PMMA and CR-39 resists using low fluences with a beam line optimized for low fluence irradiation with the expectation of patterning holes of 10 nm upon single ion impacts in both photoresists. PMMA data was inconclusive, however, CR-9 showed 100 nm holes and 30 nm depth control for single proton exposure for 2 MeV.

Alves *et. al.* [113] studied the effect of single ion damage to photo resists such as PMMA. They first characterized the dose required to fully etch the exposed resist with wider features. Relating the Linear Energy Transfer and correlating the fluence needed to fully etch the resist, they arrived at  $1 \text{ eV/nm}^3$  as the minimum damage density required. Isolated damage tracks were studied by exposing 50 nm PMMA spin coated on Si PIN diode while counting. Fluence

was varied in the range of 10 ions to 10000 ions (F, Cu and I). For a 5  $\mu\text{m}$  beam spot size, exposures less than 300 ions showed no overlap in the damage tracks. Besides, for exposures with beams of 8 MeV F, 71 MeV Cu and 88 MeV Iodine and developed under IPA: DI water with a 4:1 concentration, they showed hole diameters less than 50 nm.

The contrast in HSQ ranges from 0.55 up to 3.2 for EBL. van Kan *et. al.* [24] showed fabrication of linewidths down to 20 nm. Using PBW, a contrast of 3.2 was found for 850 nm thick HSQ. The sensitivity of HSQ and SU-8 was found to be similar for 2 MeV proton ( $30 \text{ nC/mm}^2$ ). It was shown that the resist contrast degrades based on the delay between spin coating and exposure. Wherein contrast of the resist dropped to 1.7 for an exposure delay of over nine months, implying the resist resolution degrades for delay between coating and exposure. Similar observation had been made for the process steps in e beam writing. Using a beam of 2 MeV  $\text{H}_2^+$  ions and a fluence of  $1.2 \times 10^6$  protons, a 22 nm line was written in 850 nm thick HSQ layer giving an aspect ratio of 39:1.

High aspect ratio structures have been demonstrated in SU-8 resist. However, fabrication of high aspect ratio metal structures requires photo resists which can be easily stripped after electroplating. Removal of cross-linked resist after development is challenging and incompatible with other process steps specific to applications such as imprinting and fabrication of resolution standard. TADEP [114] was developed with the ease of stripping and high aspect ratio nanofabrication capabilities. Using an optimized process [115], 280 nm linewidth was achieved using 2 MeV proton beam focused to 200 nm for resist thickness of 12  $\mu\text{m}$  (aspect ratio of 42). For a 2  $\mu\text{m}$  thick resist, linewidth of 167

nm was achieved. The spacing was preserved after Ni electroplating and resist stripping.

HSQ has shown sub 10 nm line width resolution with EBL. PBW has shown features down to 19 nm in HSQ. However, sensitivity and contrast values are found to deteriorate with increasing exposure delay. Effect on these parameters as function of delay between coating and exposure was studied by van Kan *et. al.* [116] wherein, while new batches of HSQ showed contrasts of 3.2, exposure delay of more than a year reduced the contrast to 1.2. It can thus be concluded that sensitivity of HSQ will degrade over time, and contrast varies significantly with exposure delay after coating.

PBW in chemically amplified epoxy resist KMPR and EPO core, which exhibit similar behaviour as SU-8 was performed at CIBA [117] using 2 MeV protons focused to 200 nm × 200 nm beam. Lines with dimensions down to 750 nm were written in KMPR whereas EPO core showed 10 μm squares. As opposed to SU-8, KMPR could be removed if not highly cross-linked with slight damage to the Nickel mold. However, EPO core could not be removed after electroplating.

Sensitivity of PMMA to irradiation of carbon, helium and hydrogen was compared [118] wherein sensitivity was shown to be improved with higher particle mass but with a narrowing gap between positive and negative regions. Clearing dosage as low as 53 nC/mm<sup>2</sup>, 38 nC/mm<sup>2</sup>, and 3 nC/mm<sup>2</sup> were observed for 2 MeV Protons, 3 MeV He<sup>2+</sup> and 6 MeV C<sup>3+</sup> respectively for PMMA developed in IPA:DI water.

Direct writing on Poly L lactic acid (PLLA) which is a piezoelectric polymer has been done with 1 MeV proton and developed in ammonia solution as developer [119]. 3  $\mu$ m lines were fabricated in the dose range of 500 nC/mm<sup>2</sup> to 1000 nC/mm<sup>2</sup> written with a beam size of 1.5  $\mu$ m. PFO layer was irradiated [120] which showed negative behaviour at TIARA of JAEA with a broad range of fluence (1 nC/mm<sup>2</sup> to 20000 nC/mm<sup>2</sup>) and developed in toluene. A critical dose of 1000 nC/mm<sup>2</sup> was reported with aspect ratio of 12.

Double exposure at two different beam energies leads to fabrication of 3D structures. Takano *et.al.* [121] compared the effect of super critical drying on the performance of proton beam writing as compared to normal air drying. It has been long known that, as the density of the features increases, the probability of pattern collapse due to low surface tension of the developer will increase. Supercritical drying method eliminates the wetting of the exposed photo resist by drying the sample in supercritical gas-liquid phase. Bridge structures were written using 3 MeV protons and 0.5 MeV protons in SU-8. An arching of the bridge between two supporting pliers was observed because of higher energy deposition and overlap of 3 MeV crosslinking track and Bragg peak of 0.5 MeV protons. In contrast, air dried samples showed flat bridges.

AR-P 3250 resist designed for i-line UV lithography (365 nm) shows attributes of a positive resist. However, when exposed to a beam of energetic protons, it exhibits negative behaviour. Yinghui *et. al.* [122] showed PBW and a subsequent UV exposure can be used to fabricate high aspect ratio (~10) nano structures which could be used in fabricating Nickel moulds, used for nano-imprinting and injection moulding. AR-P showed a contrast of 3.5 and a 330

nm line width with a beam of 1 MeV protons. Thinner layers of AR-P 3250 were shown to be spin coated when diluted in AR 300-12 down to 280 nm (1:3 dilution). Features down to 120 nm were fabricated and successfully transferred to Nickel mold using electroplating. A negative resist, ma-N 2401, was used to fabricate 60 nm lines using 1 MeV protons. PBW was also evaluated in ma-N 2410 (1  $\mu$ m thick) [82] with sub-micron features being faithfully transferred to Nickel mould after electroplating in nickel-sulfamate bath.

Writing with focused ions or electrons are inherently serial in nature. Time to write dense patterns is dependent on the writing algorithm employed. Patterning nano holes in wider scan area could increase the writing time as the exposure is usually done per pixel. Increasing the scan area and setting the pitch greater than the beam size therefore reduces the time required to expose the entire scan field. Nielsen *et. al.* [123] showed fabrication of nano holes using EBL with scan pitch set to the pitch intended.

van Kan *et. al.* [124] reviewed the performance of different photoresists for PBW. They also showed improvement of contrast value for ARP 3250 as the feature size reduced. This indicates a weak link between resolution and contrast value of the photoresist for a lithographic method.

## 1.6 Motivation for the thesis

PBW has demonstrated fabrication of nano-structures down to 19 nm in photoresist. A beam focusing of 9.3 nm  $\times$  32 nm has also been shown illustrating the capability of the sub-10 nm focusing of the system. This thesis aims towards optimization of the beam controls towards reproducible beam focusing defined by the system demagnification and fabrication of nanostructures in resist close

to beam spot size. With the performance characterization of PBW in HSQ, we intend to fabricate nanofluidics chips with sub-50 nm details for DNA linearization. Aiming towards higher throughput, we propose fabrication of free standing stencils using PBW and masked ion lithography for faster replication in resist.

## 2 PBW at CIBA

In this chapter, we review the layout of the proton beam writing at the Centre of Ion Beam Applications (CIBA), NUS. Figure 2-1 shows the layout of the beamlines in CIBA. A 3.5 MV Singletron accelerator from HVEE is used for 5 different beam lines shown in the schematic.

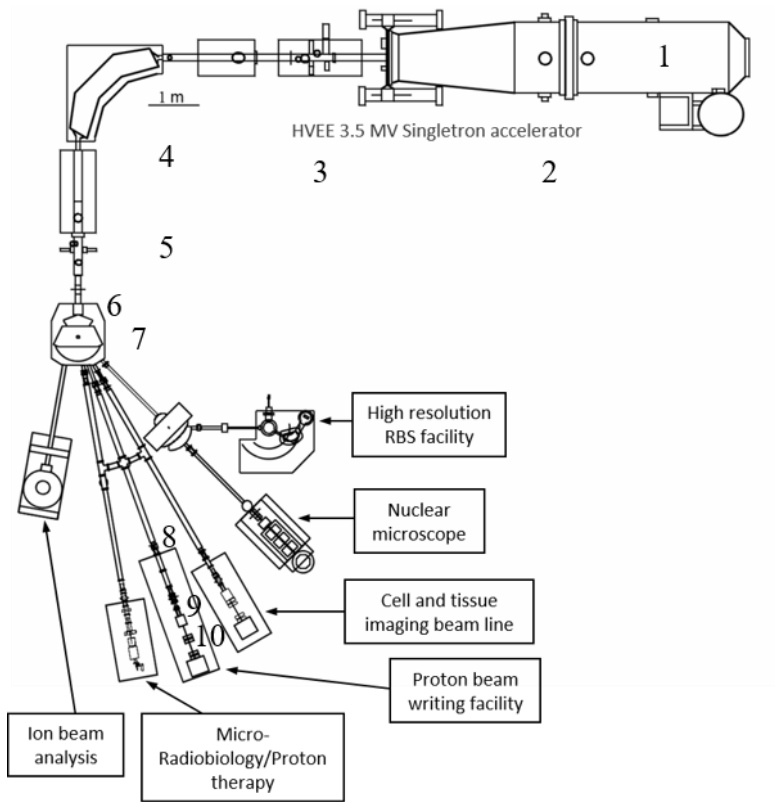


Figure 2-1. Accelerator and beamline layout at Centre for Ion Beam Applications (CIBA), NUS

### 2.1 Accelerator layout

Ions generated by exciting incoming gas to a source is extracted by applying electric field across the source (2). Energy of the ions is defined by the terminal voltage applied (1). Ion sources generate a variety of ion species of different

charge states. For example, hydrogen gas can be easily excited to generate molecular hydrogen ions with a +1-charged state or protons with +1 charge state. The required charge ( $Q$ ) and masses ( $M$ ) are filtered by the  $90^\circ$  magnet (4) which filters out the non-relevant ion species with the resolution of  $Q/M$ . By placing this magnet appropriately, it can also be used to focus the beam at the objective slit plane. Steering (3) of the ion beam out of the accelerator is controlled by applying electric fields in orthogonal directions to optimize passage of a maximized current and aligned beam. The objective aperture (5) is used to define the virtual source size of the beam and to reduce the beam divergence from the accelerator. A switcher magnet (7) bends the beam towards the end station by applying the proportional magnetic field. Blanking plates (6) are placed before the switching magnet to deflect the beam away from the beam line which stops the flow of ions towards the target station. A de-magnified image of the objective aperture is formed on the target plane by the quadrupole lens focusing system (10). For nanometre spot sizes, controlling the divergence before the focusing lenses is important. This is done by using collimator aperture (8) which reduces the beam divergence for the finer focusing through the lenses at the expense of losing beam current. The beam is scanned on the target plane by scanners (9) placed before or after quadrupole lenses.

## 2.2 Beam defining apertures

Beam defining slits are used as objective and collimating apertures to shape the beam in nuclear microprobes. MeV ions are stopped within these apertures due to their higher density and thickness, greater than the end of the range of ions in materials ( $<10\text{ }\mu\text{m}$ ). The non-interacting part of the ion beam passes through the aperture openings which can then be focused to a spot on the target plane using

electric or magnetic lenses. Spot size of the focused beam in such systems is defined by demagnified aperture size in the objective plane [125]. The collimator apertures are used to reduce the divergence and aberrations of the beam drifting from the objectives upon scanning through the quadrupole lenses [126][127]. The effect of scattering from the slits and impact on beam focusing was studied by Gorelick *et. al.* [128] and experimentally reported by van Kan *et. al.* [129] and Watt *et. al.* [130]. Some ions passing through the objective slits are scattered at the edges (i.e. transparency zone) leading to an increased angular spread of the beam along with an increased energy spread.

In the nuclear microprobe systems at Centre for Ion Beam Applications (CIBA), tungsten carbide (WC) slits are used for defining beam centroid in objective and collimator apertures. These slits serve for applications ranging from material characterization using high resolution Rutherford Back Scattering (RBS) [131], proton beam writing (PBW) [59], [129] and bio-imaging [132], [133] using focused ion beams. The slits are attached to the end of a manually operated differential micrometre to define the aperture size and alignment (Mitutoyo 110-101).

### 2.3 Electrostatic scanners

Electrostatic scanner plates in orthogonal direction are placed before the quadrupole lenses to scan the beam in image plane. Scanners are driven by individual amplifiers depending on the appropriate scan size. Larger scan sizes are achieved using Trek amplifier (Trek 609E-6  $\pm 4$  kV) with a noise level of 50mV, and smaller scan sizes are achieved using Trek amplifiers with noise

levels of 70  $\mu$ V. The ratio of the scan output voltage follows the ratio of demagnification indicating a stigmatic system.

#### 2.4 Beam blanking

A Fischer amplifier (dual  $\pm 220$ V High Voltage) with a slew rate of 1000 V/ $\mu$ s is placed before the switching magnet that applies high voltage across two parallel plates and deflects the beam away in the horizontal direction. This allows for fabrication of arbitrary structures during beam scanning.

#### 2.5 Probe-forming lenses

Due to higher magnetic rigidity of ions accelerated to MeV energies, quadrupole lenses with radial distribution of fields are needed to focus to smaller spot size.

Lorentz force acting on a particle with charge  $q$ , and velocity  $v$  in a magnetic field  $B$  can be written as:

$$\mathbf{F} = q\mathbf{v} \times \mathbf{B} \quad (2.1)$$

Magnetic field in quadrupoles are generated by the current running through the coils wrapped around the magnetic pole pieces. Figure 2-2 shows the cross-sectional view of a quadrupole magnet.

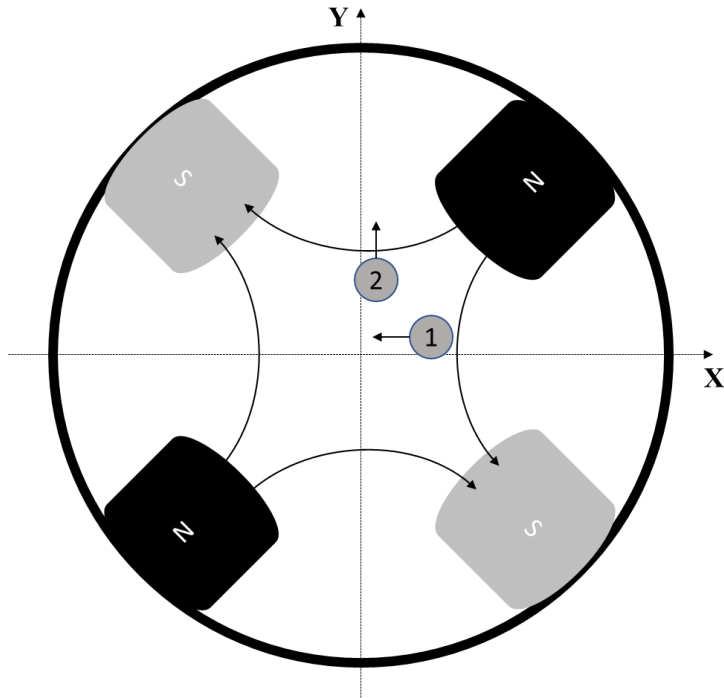


Figure 2-2. Cross-section of a quadrupole lens. Shown are the four pole pieces generating magnetic field lines in the space within. Positively charged particles at position 1 and 2 travel into the plane of the paper

Magnetic field lines are contained within the lenses and are orthogonal to the incoming charged particle travelling into the plane of the paper. A positively charged particle at position 1 will experience a force towards the centre, whereas particles at position 2 will experience an outward force. A single quadrupole lens will focus the beam in one plane and defocus in orthogonal plane. Therefore at least two quadrupole lenses are required for defining a spot focus.

A few assumptions can be considered for quadrupole lenses: They are long enough to avoid components of magnetic field in the direction of beam. Field is calculated in current free region. By Ampere's law,

$$\vec{\nabla} \times \vec{B} = 0 \quad (2.2)$$

This implies a scalar potential,  $V$  such that  $\vec{B} = \nabla V$ . Also, divergence of magnetic field is zero, i.e.  $\nabla \cdot \vec{B} = 0$ . This implies

$$\nabla^2 V = 0 \quad (2.3)$$

This Laplace equation can be solved by four-fold symmetric scalar potential of the form

$$\phi(r, \theta) = \sum_{n=2,6,10\dots} k_{2n} (\sin n\theta) r^n \quad (2.4)$$

However, due to practical limitations in manufacturing of the pole pieces, higher order harmonic terms need to be considered. The general expression of the scalar potential could then be written as

$$\phi(r, \theta) = \sum_{n=2}^{\infty} \sum_{m=2}^{\infty} v_{mn} k_{mn} r^n \sin(n\theta - \alpha_{mn}) \quad (2.5)$$

Where  $n$  is the multipole index and  $m$  is the boundary condition (equation 2.6) in the solution of Laplace equation

$$\phi(r, \theta) = -\phi\left(r, \theta + \frac{\pi}{m}\right) \quad (2.6)$$

$$v_{mn} = \begin{cases} 1, & n = m, 3m, 5m \\ 0, & \text{otherwise} \end{cases} \quad (2.7)$$

Solving for  $\mathbf{B}$  in cartesian coordinates with magnetic plane described in XY plane, the strength of the magnetic field in X direction is dependent on the distance from Y axis, while field in Y direction is dependent on the relative position from X axis as

$$B_x = GY \quad (2.8)$$

$$B_y = GX \quad (2.9)$$

where, G is the magnetic field gradient and given by

$$G \simeq \frac{2\mu_0 n I}{r_0^2} \quad (2.10)$$

Multiple lens system:

A typical nuclear microprobe beam line is an inverted microscope where the object aperture is demagnified by a set of magnetic quadrupole lenses to form an image at the target. Various configurations can be defined based on the number of lenses used namely doublet, triplet, quadruplets and so on. Higher demagnification has been shown using triplets and spaced Oxford triplet configurations at the expense of asymmetric demagnifications and chromatic and spherical aberrations. Quadruplets offer symmetric demagnification with lower spherical aberration at the expense of lower demagnification and need of higher stability of power supplies. A typical triplet configuration is called a converging – diverging and converging configuration with a cross over in X direction. Spacing the first two lenses in the direction of beam can further increase the demagnification in the converging direction.

Beam coordinates in the objective plane can be represented by a vector  $\vec{x}_o$  which is a  $N \times 1$  matrix. Such that  $\vec{x}_o \equiv [x_o, y_o, \theta_o, \phi_o, \delta]$ .

Here,  $x_o, y_o$  are the position coordinate of an ion in the object XY plane,  $\theta_o$  and  $\phi_o$  are the projection angle of the travelling ion with respect XZ-plane and YZ-planes respectively.  $\delta$  is the momentum dispersion of the ion.

For a single quadrupole lens, matrix method defines the focusing and defocusing effect in terms of a transform matrix  $M$ . Image coordinates,  $\vec{x}_i$  as a result can be written in terms of  $\vec{x}_o$  and  $M$  as

$$\vec{x}_i = M\vec{x}_o \quad (2.11)$$

For a set of multiple lenses, the image coordinate matrix can be defined in terms of  $P$ , the chain product of individual transfer matrices and a vector combination of initial coordinates expanded from each quadrupole element. Taking the first order transfer element for the system as illustrated by Grime *et. al.* [125], focal point in both X and Y directions should be independent of the divergences. This leads to a demagnification of the system in X and Y directions defined as

$$D_x = \langle x|x \rangle^{-1} \quad (2.12)$$

$$D_y = \langle y|y \rangle^{-1} \quad (2.13)$$

And image coordinates can be derived by expanding the matrix multiplication which defines the aberration of the system

$$x_i = A_o + A_1 x_o + A_2 y_o + A_3 \theta_o + \dots + A_n v_1^i v_2^j v_3^k \quad (2.14)$$

Where  $v_m$  is the system variable and  $n$  (sum of the exponents  $i, j, k$ ) describes the order of aberration.

## 2.6 Beam line optics

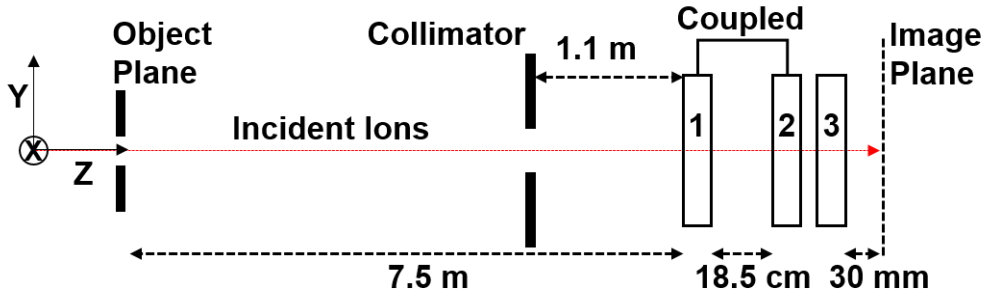


Figure 2-3. Layout of the beamline optics for PBW at CIBA. 3 Quadrupole lenses configured in spaced oxford triplet mode (CDC) with first and second lens coupled to the same power supply

Figure 2-3 shows the layout of the beam line optics used for Proton beam writing in CIBA. The optimization of the layout was done by van Kan *et. al.* [129] and Yao *et. al.* [134]. Proton beam writing system at CIBA uses spaced Oxford triplet configuration in converging-diverging-converging configuration. System parameters for this oxford triplet configuration are listed in Table 2-1 .

Table 2-1. System layout of spaced oxford triplet

Element	Distance
Object to Lens 1	7.5 m
Lens bore radius	3.75 mm
Lens length	55 mm
Spacing between lens 1 and 2	18.5 cm
Spacing between lens 2 and 3	2.5 cm
Image distance	30 mm

Beam optics simulations were carried out using particle beam optics laboratory 3.0 (PBO Lab) [135]. A beam of 2 MeV protons passes through a objective

aperture set to  $8 \times 4 \mu\text{m}^2$  with a half angle beam divergence of  $3 \mu\text{rad}$ . Beam divergence is defined using the collimator aperture opening of  $30 \times 30 \mu\text{m}^2$ .

Figure 2-4 bshows the spot focus attained with a demagnification of  $857 \times (-130)$ . Table lists down the aberration coefficient for the system.

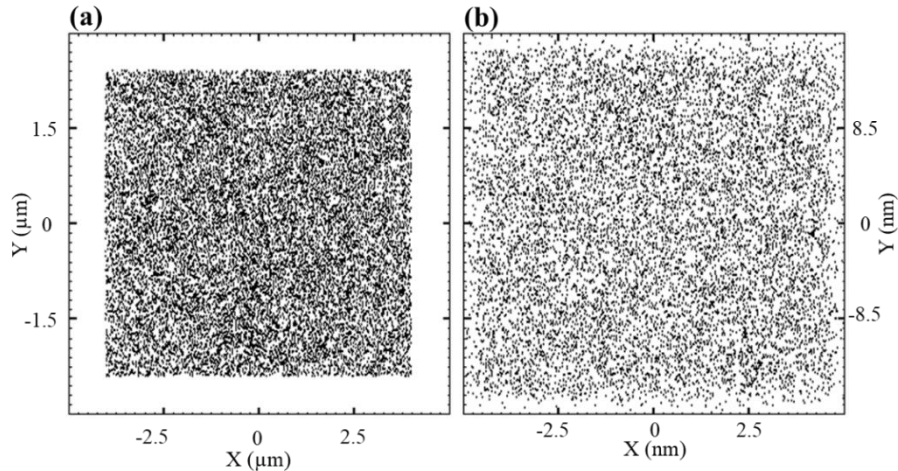


Figure 2-4. PBO Simulation of 2 MeV proton. The beam line demagnification is calculated to be  $857 \times 130$ . Figure (a) shows the particle distribution in an objective slit of opening  $8 \times 4 \mu\text{m}^2$ ; (b) shows the beam spot size of  $9.3 \times 32 \text{ nm}^2$ . Collimator aperture was set for  $30 \times 30 \mu\text{m}^2$ .

Table 2-2. Aberration Coefficient for spaced oxford triplet extracted from PBO simulations

Demagnification (First order)	$D_x = \langle x x \rangle^{-1}$	857
	$D_y = \langle y y \rangle^{-1}$	-130
Chromatic Aberration (Second order) (mm/mrad)	$\langle x \theta\delta\rangle^{-1}$	-52
	$\langle y \theta\delta\rangle^{-1}$	126
Spherical Aberration (Third order) mm/mrad <sup>3</sup>	$\langle x \theta^3\rangle$	24
	$\langle x \theta\phi^2\rangle$	10.877
	$\langle y \phi^3\rangle$	-24
	$\langle y \theta^2\phi\rangle$	-71

Chromatic aberration of the ion beam reaching the probe forming lenses, triplets or quadruplets, limits the smallest spot size achievable. Typically, stability of 100 eV per MeV is required for resolution of less than a micron. Maintaining sub-10 nm stable spot sizes require a 10-ppm stability of the incident beam for probe forming lenses with higher demagnification. Singletron accelerator at CIBA has shown resolution down to 10 nm with 20 eV stability [134].

## 2.7 Beam size estimation and focusing performance

Estimation of the beam size is the key element to auto-focus and write features in photoresist. Beam is scanned across the edge of the grid and ions/electrons are collected. The collected line scan resembles a complimentary error function. This function can be modelled as a gaussian using central limit theorem. Figure 2-5 shows the schematic of a beam being scanned across the edge.

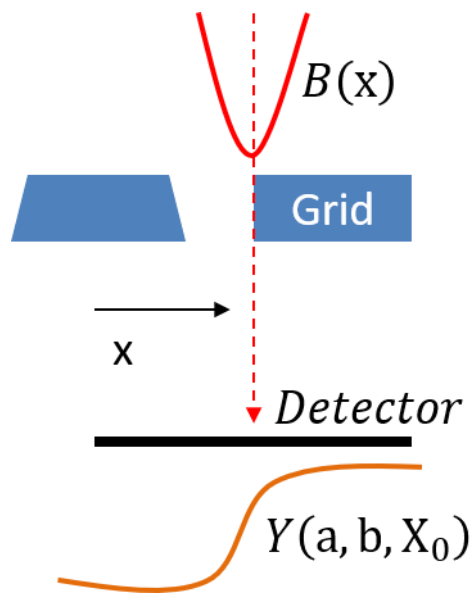


Figure 2-5 Schematic of beam spot estimation

The original beam can be modelled as 2-dimensional gaussian distribution independent of cross terms in XY as

$$B(x) = \frac{a}{\sqrt{2\pi\sigma^2}} e^{-\frac{(x-X_0)^2}{2\sigma^2}} \quad (2.15)$$

Where  $a$  is the normalization factor to get the total beam current,  $X_0$  is the beam centre which is scanned across the resolution standard edge and  $\sigma$  is the standard deviation of the beam current distribution. The grid bar can be defined as a step function,  $F(x)$  with edge positioned at  $b$ .

$$F(x) = \begin{cases} 1, & x < b \\ 0, & x \geq b \end{cases} \quad (2.16)$$

Yield of the ions/electrons collected as a function of position in  $x$  direction when the beam is scanned across the grid edge,  $Y(a,b,X_0)$  can be written as the integral of the product of the step function and the beam gaussian as

$$Y(a, b, X_0) = \int_{-\infty}^{\infty} F(x) B(x) dx \quad (2.17)$$

Defining the step at  $x = b$ , and integrating equation

$$Y(a, b, X_0) = \int_{-\infty}^b B(x) dx \quad (2.18)$$

$$Y(a, b, X_0) = \frac{a}{2} \left[ 1 + \operatorname{erf} \left( \frac{2\sqrt{\ln 2}}{f} (b - X_0) \right) \right] \quad (2.19)$$

Where  $f$  is the full width half maximum and is related to the beam standard deviation  $\sigma$  as

$$f = 2\sigma\sqrt{2\ln 2} \approx 2.35\sigma \quad (2.20)$$

For the case of electron detection, an enhanced edge is detected owing to secondary electrons escaping both from the front surface and edge of the grid bar equation 2.19 is modified with an added beam distribution weighted as per the intensity described by

$$Y(a, b, X_0) = H_{low} + H_{err} \left( 1 + \operatorname{erf} \left( \frac{2\sqrt{\ln 2}}{f} (b - X_0) \right) \right) + H_{gauss} e^{-\frac{\ln 16}{f^2} (b - X_0)^2} \quad (2.21)$$

From both equations 2.19 and 2.21, number of variables required to fit are 3 and 5 respectively. Table 2-3 below shows the percentage of the beam around the centre  $X_0$  for different threshold.

Table 2-3 Total percentage of beam as a function of sigma

Beam region	Percentage
$b \pm \sigma$	16 to 84
$b \pm f/2$	12 to 88
$b \pm 2\sigma$	2.5 to 97.5

## 2.8 Target chamber

Samples are mounted inside a custom designed end station that houses a nano-positioning stage from PI using nexus piezo mechanism. Samples are positioned in the focal plane from the feedback of Omron interferometer (Omron ZS-HLDC11). Raster scans are generated from a PXI-6259 DAQ card from

National Instruments with an effective 13-bit resolution. A resolution standard is mounted on the sample holder to focus ion beams using forward scatter scanning transmission ion beam microscopy or direct STIM. Transmitted or forward scattered ions are collected using a PIN diode (Hamamatsu, S1223) reverse biased at 15 V bias. An annular multi-channel plate (NVT 2C45/C4M10) is mounted in front of the sample mounted on the chamber wall around the beam entrance to image ion induced secondary electrons. Ortec pre-amplifier (142A) and pulse shapers are used for STIM imaging and a custom designed pre-amplifier is used for imaging secondary electrons from MCP which converts current on the collector plate to voltage pulses with a gain of 20. The shaped pulses from both the signal processing system are fed to FAST ADC (dual ADC, 7072) and a single channel analyser. Noise level in the detection system is determined using the ADC spectrum. A TTL pulse is generated by the ADC/SCA corresponding to an ion/electron detection. This pulse is fed to the gate of the counter that records the counter status. A two-dimensional image is generated by converting the counter buffer to an intensity map as shown by Udalagama *et. al.* [136] Quadrupole currents are supplied from Bruker power supply with 2 ppm resolution. These power supplies are controlled through National Instruments VISA interface. Auto-focusing is done by defining the scan length across the edges of the resolution standard. Beam size is estimated using a complementary error function and non-linear fitting for Equations 2.19 and 2.21. Lithography is done using the same interface using step and repeat or stage scan combined with beam scan.

## 2.9 Data acquisition (automation)

An important part of the proton beam writing setup is focusing and estimating the beam spot size and using it for lithography on the samples mounted in the target chamber. Object and collimator slits are aligned to the quadrupole optical axis to minimize beam steerer while adjusting the lens current supply. Proton beam is then scanned over a free-standing resolution standard using electrostatic or magnetic scanners. As the beam scatters through the resolution standard, scattered particles are collected and imaged using particle detectors. Assuming a gaussian profile for the focused beam, a line scan fit is drawn while scanning the beam at the edges of the resolution standard in orthogonal directions. This routine can be automated by optimizing the quadrupole lens current supply while estimating the beam size. Imaging of resolution standard can be achieved using various techniques such as STIM (On and OFF axis), ion induced secondary electron emission, and Rutherford Backscatter Imaging. The minimum spot focus is defined based on the demagnification of the lenses limited by the aberrations. Once the spot focus is achieved, a writing file containing the geometry of the features to be written can be loaded and the data fed to the scanners. Blanking plates are placed after the object aperture to deflect the beam away from the target for the regions in the geometry where the beam is supposed to be off. Various strategies can be employed for writing structures. Scanning the beam over the defined area is limited by the beam clipping and quadrupole parasitic aberrations. Scan area is also limited by the beam broadening at the edges of the scan field. By combining a nano-positioning stage, a step and repeat procedure can be implemented which is however prone to stitching errors. Long waveguides and channels can be written with just moving

the stage at target velocity corresponding to the dose required at a given beam current.

## 2.10 Summary

In this chapter, we introduced the implementation of PBW at CIBA. PBW beamline is based around a spaced-Oxford triplet magnetic quadrupole system used for focusing ions. This system achieves a demagnification of  $857 \times 130$  and has demonstrated focusing capability down to  $9.3 \text{ nm} \times 32 \text{ nm}$ . We also discussed estimation of beam spot size using a two-dimensional gaussian model. The complimentary error function which represents the yield of ions or secondary electrons collected by the detector is then used to extract the beam FWHM. A brief description of the end station was provided along with the implementation of data acquisition and beam control.

### 3 Beam control optimization

Proton beam writing at sub-50 nm scale needs an optimized system for reproducible nanofabrication. Smaller spot sizes can be achieved due to higher demagnification. However, this puts stringent requirement on beam focusing with reduced depth of focus. In section 3.1 we discuss implementation of a closed loop positioning algorithm. Using this system, we show an automated positioning in the focal plane with accuracy of approximately 500 nm. In section 3.3, we show an experimental thickness measurement of resolution standard to estimate side wall slope which is crucial to estimate beam spot size. In section 3.4, we discuss quadrupole alignment procedure to enable beam focusing to 13 nm in X direction. An automated slit control and focusing algorithm is discussed in sections 3.5 and 3.6 respectively. Writing strategies are discussed in section 3.7. Stitching limitation is characterized in section 3.8. Finally, in section 3.9 we discuss fabrication of Au resolution standard to improve secondary electron collection efficiency using a multi-channel plate detector.

#### 3.1 Depth of focus

A rectangular objective slit is focused to a rectangular spot size in the image plane. As shown in Figure 2-4 a PBO simulation result with objective slit opened to  $8 \times 4 \mu\text{m}^2$  results in a spot focus of  $9.3 \times 32 \text{ nm}^2$  using spaced oxford triplet configuration for the magnetic quadrupole lenses. This higher demagnification implies a lower depth of focus for the case of square collimator aperture. As the sample plane is moved away from the image plane, beam size in X direction increases more than the beam size in Y direction. Figure 3-1 below shows the change in beam spot size as a function of focal plane offset.

The ratio of the X and Y FWHM is the same as the ratio of the demagnification of the magnetic lenses configuration (system demagnification of 857:130).

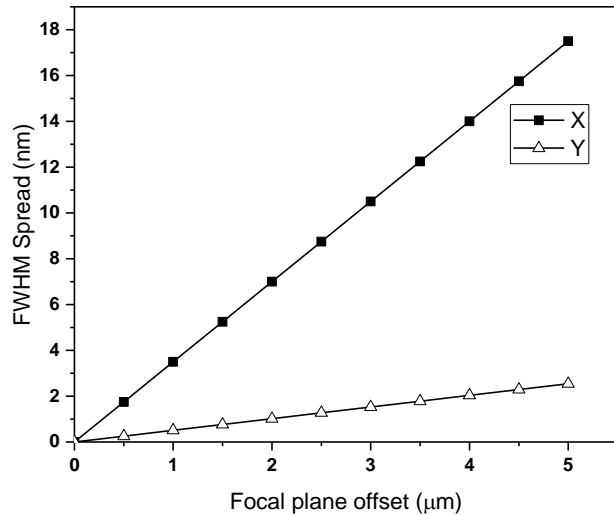


Figure 3-1. Beam full width half maximum vs focal plane offset. For fixed quadrupole excitation, if the sample plane is shifted off from the focal plane, beam spot increases more for the direction of higher demagnification.

### 3.2 Automated closed loop

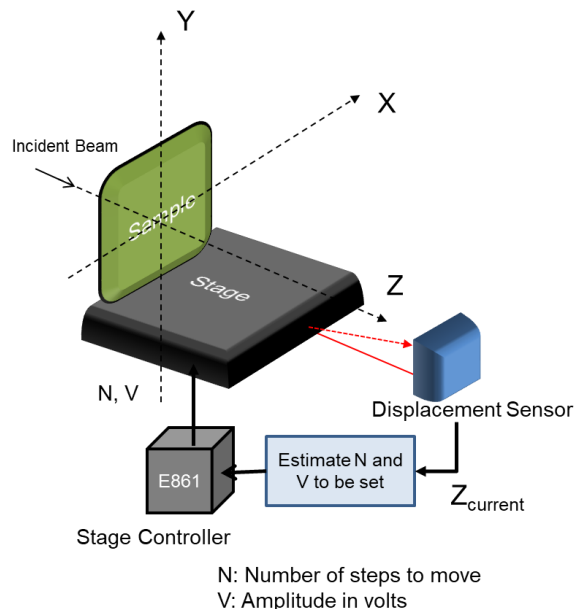


Figure 3-2. Schematic of the closed loop control in Z

Samples are mounted on top of the nano-positioning stage from PI capable of 4 nm closed loop resolution in both X and Y directions with travelling range of 20 mm each. However, it lacks a closed loop control in Z direction. Motion control in Z will be beneficial for PBW to position the sample accurately in the focal plane after optimal beam focusing has been attained through resolution standard imaging.

The closed loop network consists of a displacement sensor (Omron ZS-HLDC11) which monitors the stage motion in Z direction and a LabVIEW VI (Virtual Instrument) running on PC that processes current position value read by the sensor. This VI also commands a motion controller (PI E-861) to move the stage according to a target position value (refer Figure 3-2). Implementation of closed loop positioning is described in this section.

### 3.2.1 Calibration for step mode

Stage controller (E-861 from PI) was calibrated to determine a relation between the single step-size (SZ) of the stage in Z for applied voltages (Amplitude) ranging from 0.7 Volts to 55 Volts. Figure 3-3 shows the relationship between amplitude and step-size obtained experimentally.

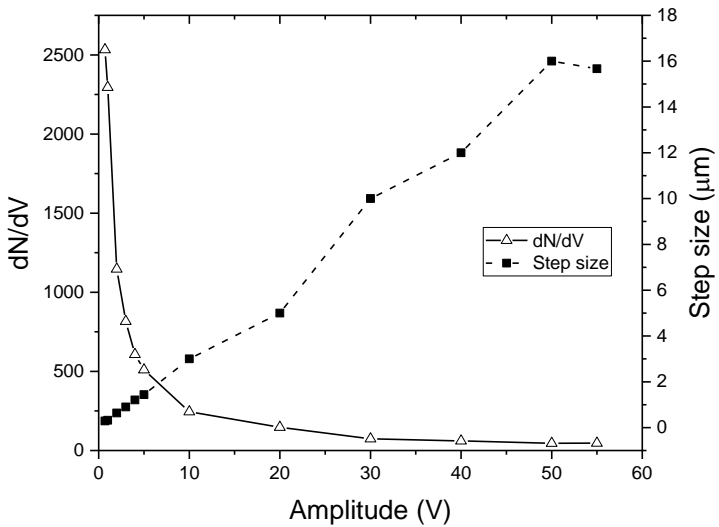


Figure 3-3. Differential step motion as a function of amplitude voltage applied. In the algorithm this determines the number of steps and step voltage needed to minimize the positioning error.

### 3.2.2 Feedback selection

Three methods (Analog Voltage, Analog Current and USB) were tested and compared for the feedback path from the displacement sensor to the DAQ/PC.

Noise remained major concern with analog feedback which also required calibration to translate to position values. Minimum noise attained using noise reduction techniques resulted in maximum positioning error of 30  $\mu m$  (Analog Voltage) and 8  $\mu m$  (Analog Current). Through serial communication, USB feedback offers accurate position measurement in comparison to analog voltage and current feedback from the sensor. Using a Burleigh Inchworm stage with closed loop resolution of 20 nm, we verified the accuracy of the read out down to 500 nm.

### 3.2.3 Algorithm development

In step mode, E-861 requires two inputs to move the stage, viz. Amplitude (A) and the number of steps (N) to move. Based on the difference between target

position and current position, a corresponding step size is chosen such that the required number of steps is an integer, otherwise the closest step size which results in minimum positioning error is passed. Amplitude is then determined based on the relationship from Figure 3-3. Analog feedback requires an extra step of determining number of steps per unit error voltage,  $\frac{dN}{dV}$ , corresponding to the position calibration for the sensor as a function of Amplitude (Figure 3-3 shows the experimental relationship for analog voltage feedback). Finally, corresponding Amplitude is derived based on the current value of  $\frac{dN}{dV}$ . To take stage hysteresis into account, algorithm runs multiple iterations until position error is reduced to a set minimum ( $\leq 500$  nm).

### 3.3 Sidewall slope estimation

Estimation of beam FWHM was discussed in chapter 2 with beam modelled as 2D Gaussian. Beam is scanned across the edge of the resolution standard and a Yield function is fit using non-linear LMA algorithm. Grid edge was assumed to be step function in equation to derive the intensity yield as a function of distance. Experimental yield curves are dependent on the side wall slope of the resolution standard. As the slope gets wider, beam size is convoluted with the sidewall slope. Estimation of beam size thus depends heavily on the sidewall slope of the resolution standard used for imaging. Earlier experiments using Ni resolution standards with sidewall slopes of 30 nm resulted in over estimating the beam spot size when compared to the feature sizes resolved in photo-resist [137]. A sub-micron thick Ni resolution standard was fabricated using PBW [138] with expected side-wall slope of approximately 6 nm. In this section, we

describe thickness measurement and estimation of sidewall slope of the fabricated resolution standard using STIM.

Besides regular imaging, STIM can also be used for spectroscopic measurements [139], [140]. In order to experimentally determine the thickness of the PBW resolution grid [138], we calculate the energy loss of a molecular beam ( $H_2^+$ ) through the Ni grid. This 1 MeV  $H_2^+$  beam was scanned across an edge of the grid for a total length of  $\sim 1.5 \mu m$ . As soon as the incoming high energy molecular hydrogen interacts with the surface of the grid bars, it splits into two protons each carrying half the energy. Each proton then propagates through the grid, losing energy mostly due to electronic scattering. Protons are then detected by a silicon PIN diode (Make: Hamamatsu, Model: S1223 with a detector resolution of 30 keV) positioned on-axis behind the grid. Scanning the beam across the edge of the grid bar and recording the energy spectrum, using STIM, will result in three peaks. The first peak, labelled as D in Figure 3-4a, corresponds to the direct beam with an energy of 1 MeV and the second peak, labelled as T in Figure 3-4a, corresponds to the transmitted beam through the grid. The third peak, hardly visible in Figure 3-4a, corresponds to the coincident detection or pile-up of two particles in peak T. Energy calibration is required to determine the energy of the peaks. The energy calibration equation can be written as:

$$E_n = nE_{ch} + Z \quad (3.1)$$

where  $E_n$  denotes the energy of  $n^{th}$  ADC channel calculated using  $E_{ch}$  (energy per channel) and Z (zero-channel offset energy). This equation is solved by using known energy values of two ADC channels. The energy of the direct beam

is known from the accelerator potential applied (1 MV) which corresponds to peak D in Figure 3-4a.

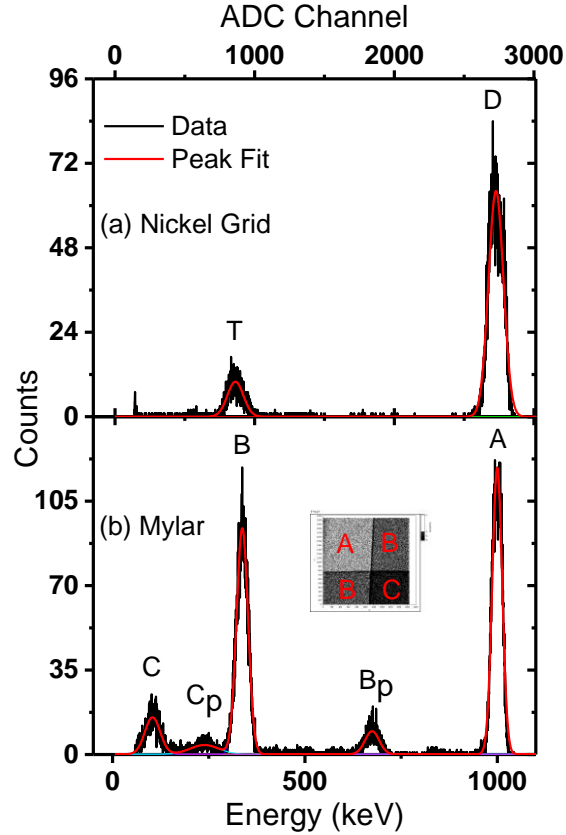


Figure 3-4 (a) STIM Spectrum of 1 MeV  $\text{H}_2^+$  through Ni grid. (b) STIM spectrum through 0, 2.5  $\mu\text{m}$  and 5  $\mu\text{m}$  thick layers of Mylar. Inset shows the On-axis STIM image over a scan size of  $130 \times 130 \mu\text{m}^2$ .

To determine the energy of the second peak, T in Figure 3-4a, we performed a separate spectrum calibration using Mylar foils of different thicknesses, as shown in the inset of Figure 3-4b ( $A = 0$ ,  $B = 2.5 \mu\text{m}$ , and  $C = 5 \mu\text{m}$ ). The same 1 MeV  $\text{H}_2^+$  beam was raster scanned across the intersection of the stacked Mylar foils. The corresponding STIM spectrum obtained is shown in Figure 3-4b. Peaks labelled A, B and C corresponds to region with 0, 2.5 and 5  $\mu\text{m}$  thick layers of Mylar respectively. Two smaller peaks labelled  $B_P$  and  $C_P$  correspond

to the coincident or pile-up detection of two particles with energies corresponding to peaks B and C respectively.

Next, two methods were employed to calibrate this Mylar spectrum. The first method employs the fact that energy of peaks  $B_P$  and  $C_P$  is twice the energy of peaks B and C respectively. Based on this observation, the energy calibration equation (Eq. 1) is solved, and the result is shown in Table 1 under method 1. Using this calibration, we calculated the energy of peak T in Figure 3-4(a) to be 320 keV. Subtracting the energy of this transmitted beam (320 keV) from its otherwise un-scattered counterpart (500 keV), will yield the total energy loss of each 500 keV proton when passing through the Ni grid, which is  $179 \pm 24$  keV. Using the electronic energy loss in Ni (average  $S_E = 171.45$  keV/ $\mu\text{m}$ ) from SRIM [34], the Ni grid thickness is estimated as  $1.04 \pm 0.14$   $\mu\text{m}$ .

In the second method, we use the energy of the transmitted ions (peak B in Figure 3-4b) propagating through a 2.5  $\mu\text{m}$  thick Mylar foil, to compute the energy of peak T in Figure 3-4a. A SRIM [141] simulation for 10000 protons with an energy of 500 keV propagating through 2.5  $\mu\text{m}$  thick Mylar shows a forward scattered proton energy of  $368 \pm 7$  keV (refer Figure 3-4(b) peak B). Substituting the energy values of peak A and B and solving the energy calibration equation (Eq. 1), we obtain  $E_{ch}$  and Z, as shown in Table 3-1 under method 2. On applying this energy calibration to the Ni grid spectrum, the energy of peak T (in Figure 3-4a) is found to be 351.0 keV, and the corresponding energy loss of a 500 keV proton through the Ni grid is estimated to be  $149 \pm 24$  keV. Using average electronic energy loss in Ni ( $S_E = 171.45$  keV/ $\mu\text{m}$ , from SRIM) for a 500 keV proton, the grid is measured to be  $0.86 \pm$

0.14  $\mu\text{m}$  thick. Same exercise was repeated with a 2 MeV  $\text{H}_2^+$  beam for Ni grid using method 1. Combining all the measured values, we estimate the Ni grid to be  $0.9 \pm 0.1 \mu\text{m}$  thick. These measurements are in agreement with the intended thickness of the electroplated Ni grid [138] and correspond to a  $6.0 \pm 0.6 \text{ nm}$  side-wall slope, vital for achieving sub 10 nm beam focusing.

Table 3-1. Parameters used/estimated for grid thickness measurement

<b>For protons</b>	<b>Method 1</b>	<b>Method 2</b>
<b>Incident energy = 500 keV</b>		
Energy calibration equation	$E_n(\text{keV})$ $= 0.363n$ $+ 6.173$	$E_n(\text{keV})$ $= 0.346n$ $+ 52.701$
Energy of peak S in Figure 3-4a (keV)	320	351
Calculated energy loss through Ni grid (keV)	$179 \pm 24$	$149 \pm 24$
Average $S_E$ (electronic energy loss) in Ni, simulated using SRIM, (keV/ $\mu\text{m}$ )	171.45	171.45
Ni grid thickness ( $\mu\text{m}$ )	$1.04 \pm 0.14$	$0.86 \pm 0.14$

### 3.4 Quadrupole alignment

Rotational and/or translational misalignment in the quadrupole lens system for a spaced Oxford triplet configuration can severely affect the achievable ultimate beam spot [125]. Layout of the focusing system was described in section 2.6.

First order translation misalignment can be checked by translating the collimator slits around the optic axis of the quadrupoles. Figure 3-5 shows the variation in beam full width half maximum (FWHM) in Y direction, measured using STIM as a function of collimator slit translations:  $C_x$  and  $C_y$  around the optic axis of the quadrupoles in X and Y directions respectively. With respect to Y FWHM, two notable things are observed from Figure 3-5: system inability to focus below 100 nm, and significant beam size variation with respect to collimator slit position.

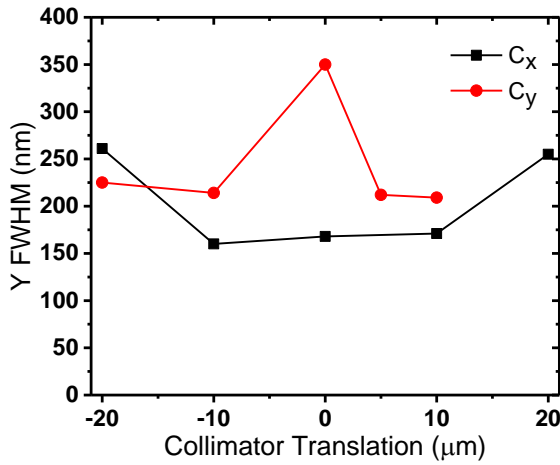


Figure 3-5. Y FWHM plotted as function of collimator translation in X and Y directions around quadrupole optic axis.

Both aspects indicate first order translational aberration. However, X FWHM remains constant within measurement error as a function of collimator translation in X and Y directions (not shown). Collimator translation of 40  $\mu\text{m}$  in  $C_x$  and  $C_y$  results in average X FWHM of 46 nm ( $\pm 28$ ) and 52 nm ( $\pm 17$ ) respectively. A well aligned system, on the other hand, shows no change in both X and Y FWHM, implying a corrected first order translation aberration. For the object and collimator slit openings of  $8 \times 4 \mu\text{m}^2$  and  $30 \times 30 \mu\text{m}^2$

respectively and 40  $\mu\text{m}$  collimator translation,  $C_x$ , the X and Y FWHM remain constant within measurement error;  $37 \pm 9$  nm and  $75 \pm 11$  nm respectively. Similarly, for collimator translation  $C_y$ , we measure a constant X and Y FWHM of  $33 \pm 11$  nm and  $73 \pm 12$  nm respectively.

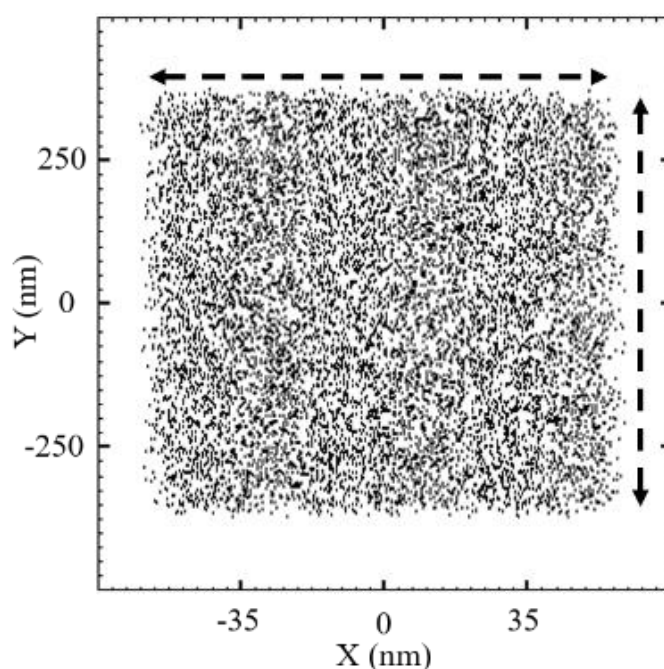


Figure 3-6 PBO Simulation of rotational misalignment

Figure 3-6 shows the effect of a 1 mrad rotational misalignment of lens 2 (roll rotation around the optic axis) on the spot size. The spot size in X direction increases from 9 nm to 120 nm and Y size increases from 32 nm to 760 nm. Due to diverging nature of lens 2, Y FWHM is prone to larger variation than X FWHM because of rotational misalignment as shown in Figure 3-7. Rotating lens 2 in a range of -0.75 to 0.5 mrad varies Y FWHM from 400 nm to 1  $\mu\text{m}$  respectively with a minima at -0.5 mrad, wherein Y FWHM drops to 90 nm without adjusting quadrupole excitation. This observation matches with the simulation of the misalignment.

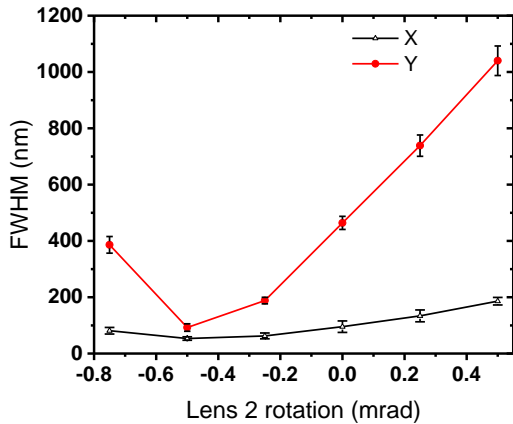


Figure 3-7. Effect of lens 2 rotation upon beam size.

Figure 3-8a-d shows a sequence of steps taken to align the quadrupole lenses using ion beam fluorescence from quartz, thereby correcting higher order translation and rotational aberrations. A horizontal line focus is shown in Figure 3-8a, which steers above and below the spot focus for under and over focusing respectively. This higher order translational aberration can only be corrected by translating lens 2 in +Y direction by 20  $\mu\text{m}$ . Moving either lens 1 or 3 in  $\pm\text{Y}$  didn't result in reduction of translational aberration; and neither did moving the collimators in  $\pm\text{Y}$  direction reduce this translational aberration.

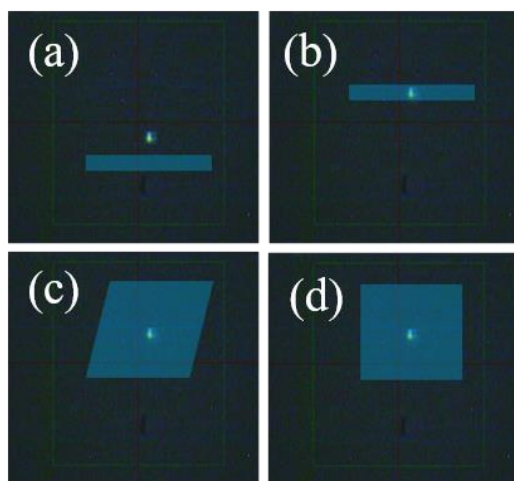


Figure 3-8. (a) Before and (b) After alignment. Higher order rotational aberration: (c) before and (d) after correction.

Figure 3-8b shows a corrected higher order translational aberration where the line focus does not steer away from the spot focus [125]. Figure 3-8c shows higher order rotational misalignment which is corrected by rotating lenses 2 and 3 till a rectangular focus, as shown in Figure 3-8d, is achieved. Following this alignment procedure, a beam focusing of  $18 \times 32 \text{ nm}^2$  was obtained for 2 MeV protons for an object slit opening of  $8 \times 4 \mu\text{m}^2$  and collimator slit opening of  $30 \times 30 \mu\text{m}^2$ .

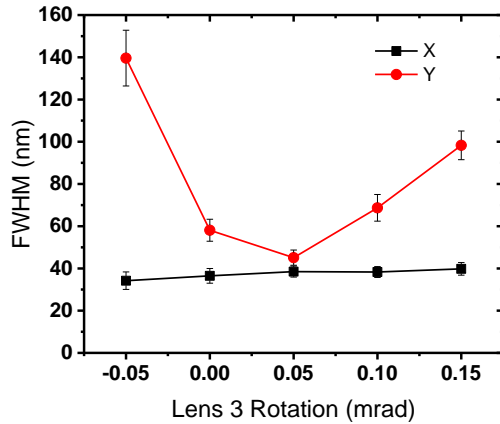


Figure 3-9. Correction for rotational misalignment by fine tuning lens 3 rotation

Next, with a beam size closer to the expected value, based on system demagnification in Y direction, a fine tuning of lenses 1 and 3 was carried out for rotational misalignment correction. Figure 3-9 shows the variation of beam size as a function of rotation of lens 3. Over the range of rotation, a dip in Y FWHM is observed for a rotation of 0.05 mrad whereas X FWHM remains unperturbed. Rotating Lens 1 (not shown here) by -0.75 mrad to 0.25 mrad showed no effect on the beam spot size with beam FWHM remaining constant around  $(43 \pm 10) \times (57 \pm 12) \text{ nm}^2$ .

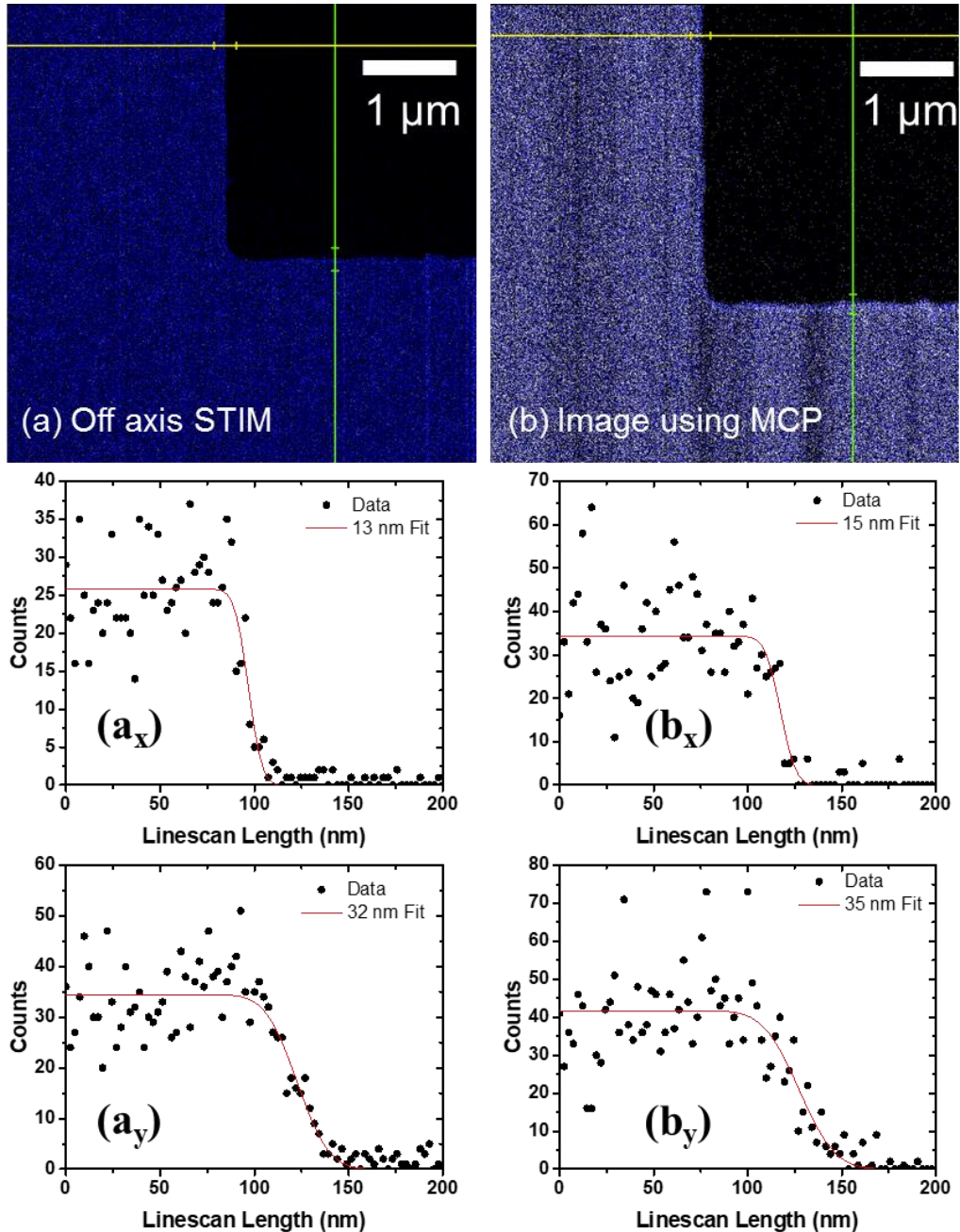


Figure 3-10. Optimal focus after quadrupole alignment. (a) Off-axis scanning transmission ion microscopy images of the Ni resolution standard with  $(a_x, a_y)$  extracted line scans by adding 200 neighbouring pixels. (b) Secondary electron image acquired using MCP with  $(b_x, b_y)$  showing extracted line scans by adding 120 neighbouring pixels. Images (a) and (b) were taken with scan size of  $5 \times 5 \mu\text{m}^2$

Finally, for 1 MeV  $\text{H}_2^+$  beam, at a reduced brightness of  $15 \text{ A}/(\text{m}^2\text{srV})$ , Figure 3-10(a) and Figure 3-10(b) show STIM image and MCP image of the grid respectively. Extracted line scans in X and Y directions for STIM, shown in

Figure 3-10a<sub>x</sub> and Figure 3-10a<sub>y</sub>, results in a focused spot of  $13 \times 32 \text{ nm}^2$ . Figure 3-10b<sub>x</sub> and Figure 3-10b<sub>y</sub> shows the corresponding X and Y extracted line scans for the secondary electron image acquired using MCP indicating a spot size of  $15 \times 35 \text{ nm}^2$ . Both Figure 3-10a and Figure 3-10b were acquired in integration mode of 4 frames with 2048 pixel resolution for a scan size of  $5 \times 5 \mu\text{m}^2$ . To ensure 70% or above goodness of fit for the error function, 100 neighbouring pixels were added to generate the line scans.

### 3.5 Automated slit control

The current manually controlled beam focusing is slow and requires skilled operators. Therefore, an automated system for proton beam collimation and focusing using precision slits, controlled using stepper motors is introduced.

In this section, we report fast automated slit positioning with developed hardware and software. Beam defining micrometres are coupled to stepper motors using 3D printed gears. An adaptive convergent algorithm is developed and implemented for fully automated slit control and manipulation. Key slit automation functions implemented include collimator and objective slit alignment using ion induced fluorescence and beam current as feedbacks respectively. Coupled with the autofocusing algorithm, we demonstrate focusing of a 2 MeV H<sub>2</sub><sup>+</sup> beam to a spot size of  $23 \times 32 \text{ nm}^2$  with a brightness of  $42 \text{ A}/(\text{m}^2\text{srV})$ .

### 3.5.1 Hardware design

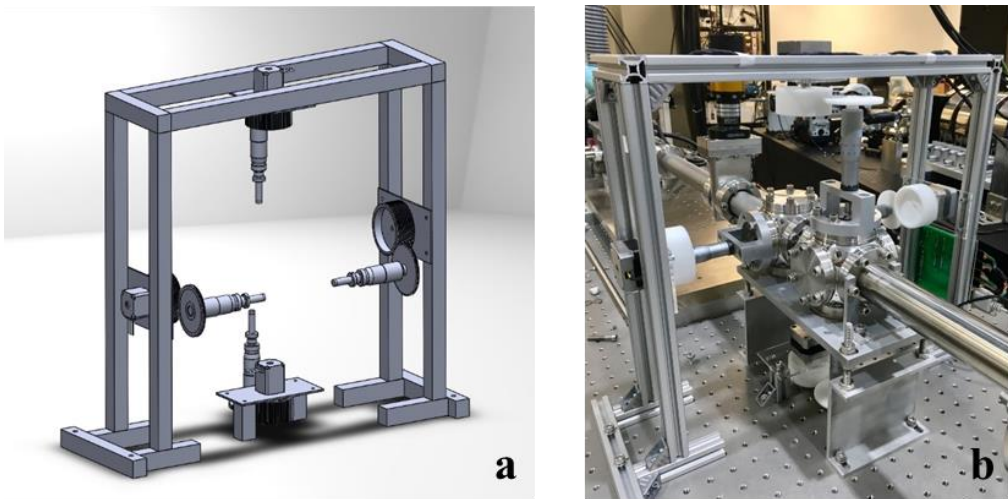


Figure 3-11. a) CAD Drawing of the motor housing made with aluminium profiles. Bottom motor is placed inverted due to space constraints. b) Housing with the motors mounted and coupled to the micrometres using 3D-printed gears.

A housing structure designed around the objective and collimator chamber respectively to mount the four DC stepper motors is shown in Figure 3-11. The housing is made from aluminium profiles and angle brackets. Motors are mounted onto a plate, and their position can be adjusted to make best contact between two gears to minimize backlash. The bottom micrometre is placed upside down due to space constraint, as shown in Figure 3-11.

The stepper motors are controlled by drivers placed on a custom designed printed circuit board (PCB). The micrometre thimble travels 25 mm forward or backward while the motor shaft only rotates. The stepper motor shaft is coupled to the micrometre thimble using 3D-printed gears on both. The gear thicknesses on micrometre thimble and motor shaft are 5 mm and 30 mm respectively. This is to accommodate the travel range of 25 mm by micrometre thimble. Both gears

are 55 mm in diameter and have 100 teeth in their circumference. Small teeth on the gear reduce backlash by decreasing the gap in between teeth.

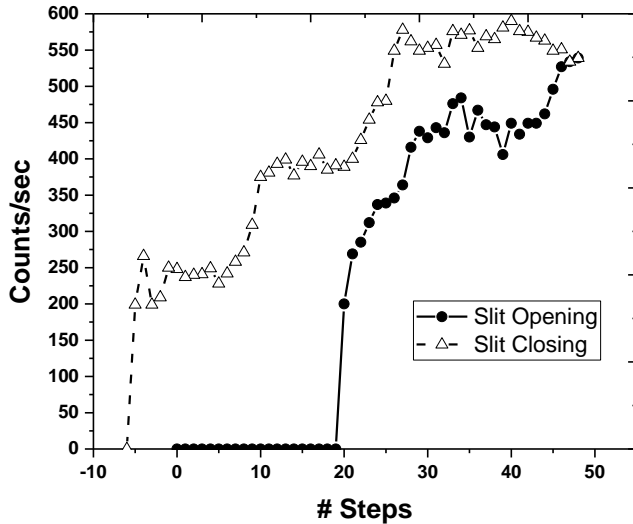


Figure 3-12. Study of micrometre backlash. Micrometre was moved by single step each time and beam current measured

We studied backlash of the gear coupling using the feedback from counts collected during off axis scanning transmission ion microscopy (STIM). Figure 3-12 shows the count rate as the micrometre gear system is moved by a single step (~62.5 nm). Repeatability in positioning was found to be 375 nm. The gear coupling backlash is negligible when the motors are moved in the one direction. A backlash of 1.375  $\mu\text{m}$  was determined when the motion direction is reversed which can be easily compensated via software control.

Effect of magnetic field intensity from the stepper motors was studied during motion and standby condition. An external DC field will lead to deflection of beam on the image plane based on the amplitude and direction. A stray alternating field will have an effect of broadening the objective aperture thereby leading to a degradation of the beam spot resolution [142]. DC stepper motors

were used for the project along with drivers to minimize the current drawn by the motors and switch the motors to standby condition wherein negligible current is drawn. No change in the background AC field was observed along the beam line while motors were switched from standby condition into operation. The background AC levels read using a magnetometer (Gaussmeter GM-2 from AlphaLab, Inc.) were  $60 \mu\text{T}$  throughout along the beam line. DC field along the motor axis was observed and recorded as function of position (refer to Figure 3-13) using DTM-151 from Group3 with LPT-141 Hall probe. Magnetic field intensity falls by two orders magnitude to the background level within 10 cm from the motor. No effect was observed on the final beam spot as the closest distance between the motor and the beam line is in bottom Y direction is 20 cm.

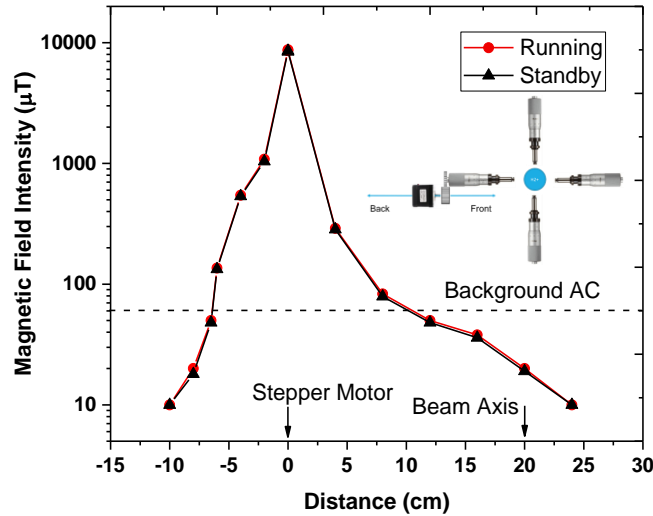


Figure 3-13. Magnetic field intensity along the motor shaft axis

### 3.5.2 Algorithm and control interface

The custom designed PCB interfaces with all the four motors for each aperture. Step and direction digital signals are generated from the PXI or Arduino carried on through DB25 and split to a DB9 cable controlling the objective slits. Enable

signals select the motor to be moved. Two motors, one from each direction, were paired to minimize the number of control signals running from the PC to the driver boards. Since these motors are not moved simultaneously, they also share the direction signal. In total 14 control signals are generated and controlled based on the algorithm stage. Schematic of the computer interface is shown in Figure 3-14.

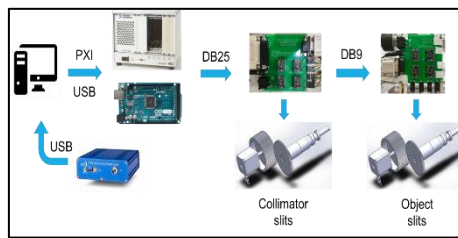


Figure 3-14. Computer interface to the stepper motors

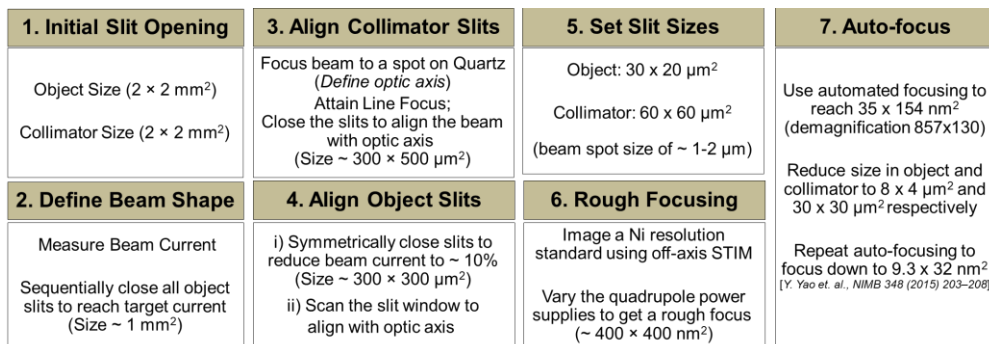


Figure 3-15. Automated alignment algorithm flowchart

The sequence of alignment and focusing algorithm is described in a flowchart (Figure 3-15). Step 1 fixes the initial objective and collimator sizes to allow tuning the beam in target chamber. In step 2, all the four objective slits are engaged with the beam thereby defining a rectangular aperture. Collimator slits are aligned in step 3 by aligning the line foci in horizontal and vertical direction to the quadrupole optic axis. In step 4i), the objective slits are closed

symmetrically in horizontal and vertical direction till the target beam current is achieved (i.e. reducing the slit size). Objective slit window is scanned sequentially in both horizontal and vertical direction mapping the beam current against slit position (step 4ii). Direction of the scan is reversed, and step size is reduced if the beam current drops for consecutive steps. The scanning is continued till the step size reaches  $1 \mu\text{m}$  level.

In step 5, size of the objective and collimator apertures are fixed to be followed by a rough focusing using STIM imaging of a resolution standard using PIN diode as detector (step 6). In the final step, automated focusing is now used by setting the range of current to locate the optimal current supplies for the two quadrupole power supplies. Using this method, we can typically reach spot size of sub-20 nm in one direction.

Each step in the algorithm is nested in a state machine. Figure 3-16 shows the interface for automated alignment developed using an even driven producer-consumer architecture with queue message handlers in LabVIEW 2011 [143].

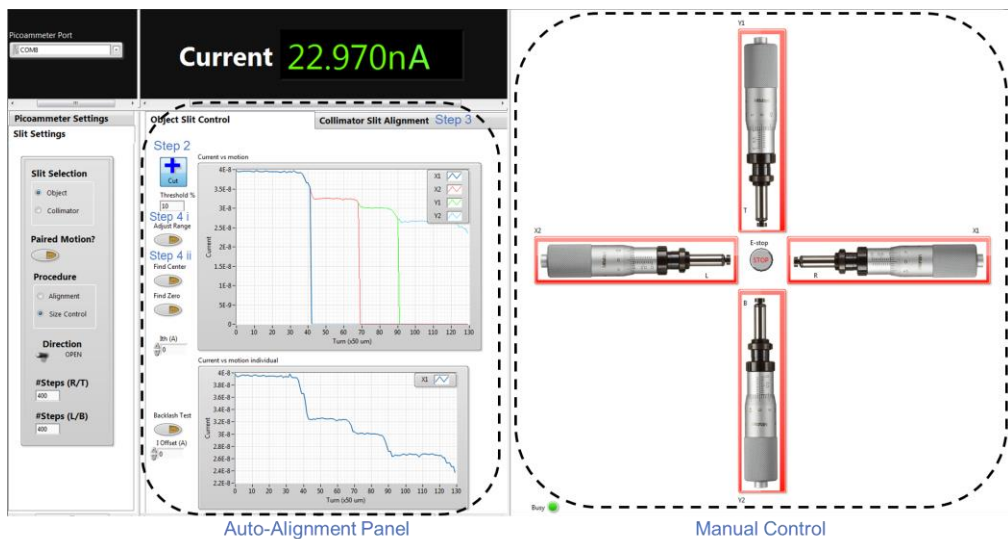


Figure 3-16. Control Interface written in LabVIEW 2011

### 3.5.3 Results

A beam of 2 MeV H<sub>2</sub><sup>+</sup> ions tuned in target chamber to get ~40 nA beam current.

Slits in objective were sequentially closed till the beam current reduced to 60%.

This threshold is user controlled and depends on the total current and beam stability. Figure 3-17a shows the beam current reduction measured using an RBD pico-ammeter (0.1 pA sensitivity) with beam parked on the resolution standard holder. Typical objective sizes after this stage is ~ 1 mm<sup>2</sup>.

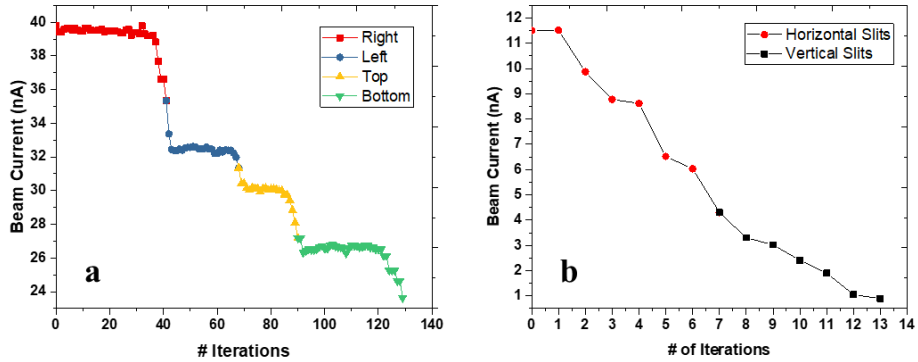


Figure 3-17. a) Defining Beam Shape in objective slit (step 2, Figure 3-15). A rectangular aperture is defined in objective slit after this step. b) Reducing objective size as per step 4i in Figure 3-15.

Figure 3-17b shows the closing of horizontal and vertical slits until the beam current is reduced to 1 nA. Typical range (1-2 nA) for this threshold depends on the beam stability ( $\pm 1$  to  $\pm 5\%$ ) and current measurement. At the end of this step the size of the objective slit is reduced to 300  $\mu\text{m} \times 300 \mu\text{m}$ .

To locate the centre (also the beam maxima) in objective slits, beam current is read at the beginning and assigned as maximum. Objective slit window is scanned across the horizontal direction such that the slits move in the same direction keeping the window opening fixed. As the current starts to drop from the maximum value, the gradient of the current vs position is tracked. Figure

3-18 shows the beam current vs iteration for the objective slits. Scanning is initialized in horizontal direction. Beam current of 1 nA at the beginning till maxima of 1.875 nA is achieved in x direction. Scan direction is changed several times whenever a negative gradient is established, and scan length is reduced to half. This process goes on till the scan length reduces to 1 $\mu$ m thereby setting the position accuracy across the beam centroid to be ~1  $\mu$ m and a maximum of 2.75 nA beam current is observed. Objective and collimator sizes can be set now to begin auto-focusing.

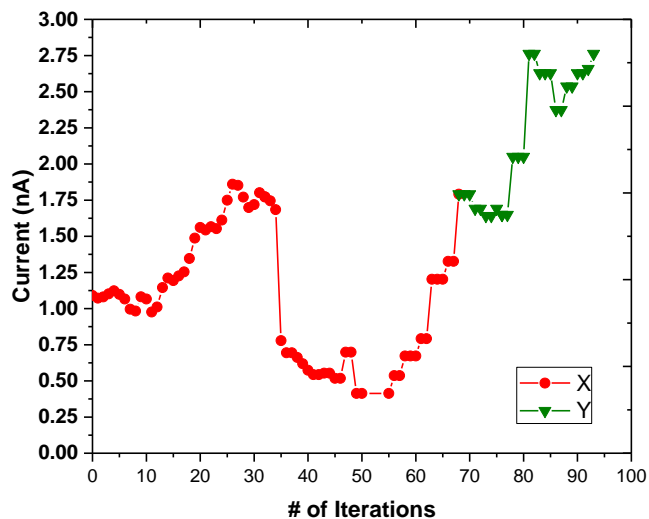


Figure 3-18. Objective slit alignment as per step 4ii in Figure 3-15. Slits are scanned with fixed opening till the maximum current position is found in both X & Y directions. Scan step size and direction are reduced and reversed respectively with negative beam current gradient

### 3.6 Autofocusing

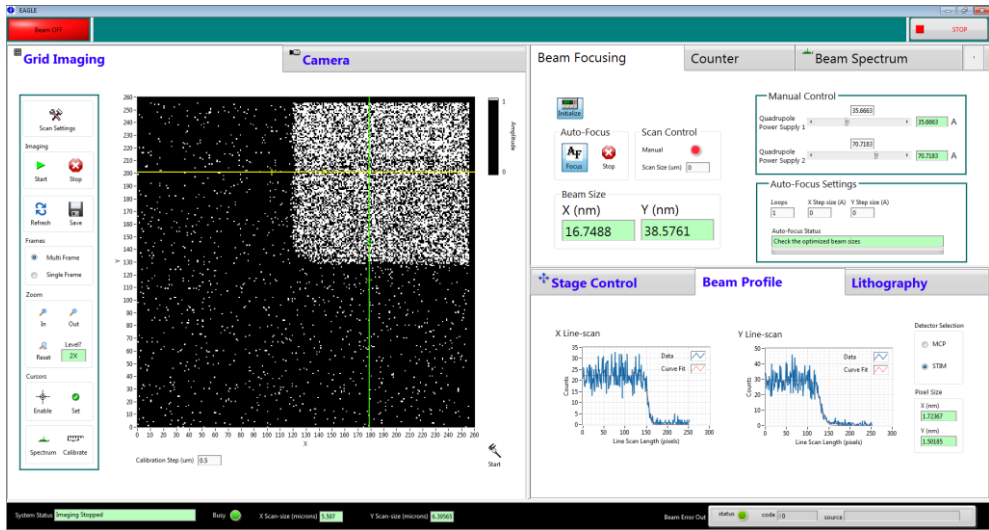


Figure 3-19. Control Interface developed in LabVIEW 2011. Shown are all the tabs with different functionality.

A user-friendly control interface, shown in Figure 3-19, written in LabVIEW using an event mode programming was developed following producer consumer loop with queue message handlers. The interface features STIM, and Ion induced secondary electron imaging, controls for beam scanning amplifiers, automated focusing, nano-positioning, automated scan size calibration and lithography operations. Each of these aspects are described in the following sections.

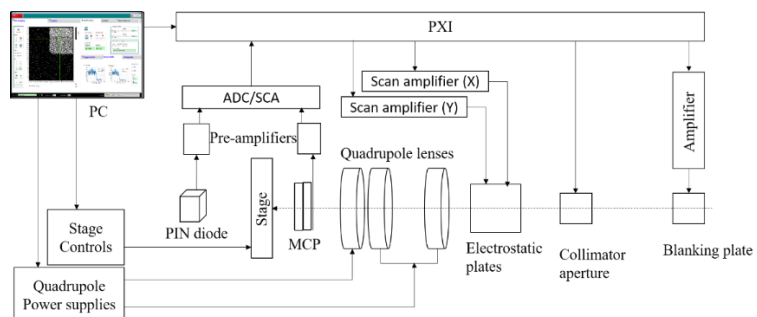


Figure 3-20. Layout of data acquisition for PBW

### 3.6.1 Grid imaging

Being able to image ions/secondary electrons emitted upon ion irradiation from a resolution standard is the key to beam focusing. Aspects of imaging involves scanning the beam over a field using electrostatic fields generated by parallel plates in orthogonal directions. Refer to Figure 3-20 for the layout of data acquisition for PBW. The scan voltage is provided by two individual voltage amplifiers in two ranges. Scan sizes of 130  $\mu\text{m}$  are provided using Trek, (609E6, +/-4kV) amplifier which provides a gain of 1000 at a slew rate of 150 V/ $\mu\text{s}$  and 50 mV rms noise. Scan sizes with 1 nm per pixel scan resolution are generated using AE Techron (6224, +/-220 V) with a total gain of 200 and 75  $\mu\text{V}$  output noise at a slew rate of 75V/ $\mu\text{s}$ . Scan settings control the input to the amplifiers. Two analog output voltages are driven from a PXI 6259 (1.25 MHz, 4 analog channels, +/-10 V, 16-bit DAC with 13-bit effective measured DAC resolution) and fed to the scan amplifiers to be amplified by 1000 or 200 based on the resolution intended for scanning. The scan frequency decides the pixel dwell time during scanning. Raster scan pattern can be generated in two ways with either of the X and Y analog outputs set as slow scan direction. Fast scan direction sweeps the analog output voltage in steps defined by the scan resolution. Edge blurring of the resolution standard can be decoupled from scan voltage noise by comparing the images from two modes of raster scans.

Imaging begins with a counter index recorded for every pulse received from the counting set-up in STIM/electron detection mode. The counter index is then mapped to generate a 2D image with pixel intensity representing number of counts detected at each individual pixel (method described in [136]). This method of imaging allows for faster scan at the expense of being asynchronous.

Two modes of image mapping can be used while active scanning. Multi frame mode allows for integrating counts at each pixel for every scan thereby showing higher contrast images. Single frame updates the counts per pixels for every scan. Refresh control restarts the scanning from the start of the frame and resets the pixel intensity for multi frame mode. Zoom control defines the scan control without keying in the exact value of scan voltage needed. A maximum of 20x zoom is supported which is limited by the resolution of the DAC. Zoom level can be reset at any point during imaging. The status of the imaging is updated at the bottom status indicator of the system. An average count rate is displayed to the right tab during imaging.

The imaging control also allows the possibility of aiming the beam at particular spot. One usage of this capability is in determining the cut-off levels for detector noise and distinguishing between forward scattered ion and ions with no energy loss through the resolution standard. Using the spectrum control, a beam energy spectrum is collected from an ADC that digitizes the signal coming from the detectors after pre-amplification and pulse shaping. This spectrum determines the cut-off levels.

Scan size calibration thus far had been done by marking edge positions before and after moving the grid in orthogonal directions. Here we use an automated approach with higher resolution. A line scan is generated for both X and Y directions sequentially. Based on the user directed calibration step in  $\mu\text{m}$ , the nano-positioning stage is moved in the corresponding axis and another line scan is collected. The edge locations of the two scans are compared and equated to

the motion of the stage. Figure 3-21 shows the result of scan size calibration in X (a) and Y directions (b).

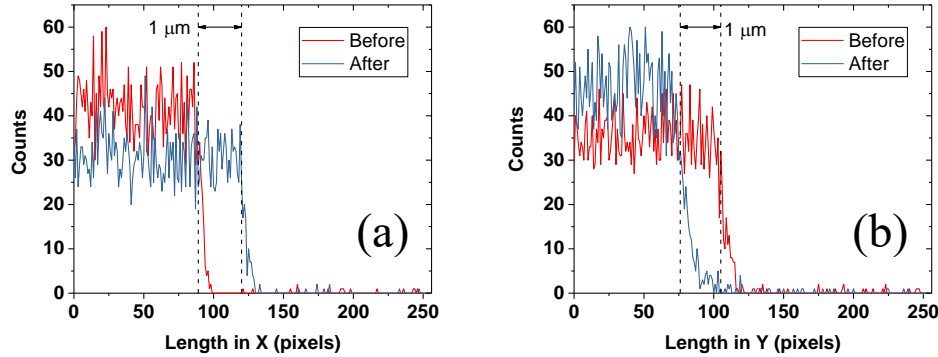


Figure 3-21. Automated Scan size calibration. (a) Scan calibration in X direction with 1  $\mu\text{m}$  stage motion corresponds to 31-pixel difference in the edge position (120-89) resulting in Pixel size of 32 nm. Calculated X FWHM = 262 nm; (b) Scan calibration in Y direction with 1  $\mu\text{m}$  stage motion corresponds to 29-pixel difference between the edge locations (105-76) at a Pixel Size of 34.5 nm and calculated Y FWHM of 448 nm.

Edge locations of the before and after scans are compared to the stage motion, and scan size is calculated for the total scan voltage from the DAC. This method results in an improved resolution for measuring the scan size with resolution limited by the beam focus and line scan pixel resolution. Typically, scan size calibration resolution using this method is of the order of 4-5 nm per scan pixel for stage motion of 200 nm.

### 3.6.2 Automated focusing

Collimator slits are aligned by looking at the ion induced fluorescence on the quartz sample mounted on the sample holder. The beam spot can be viewed using the camera control tab wherein beam spot location can be fixed and alignment performed by defining cross hairs for line focusing. After the slits are aligned using the automated alignment interface and the size of the slit openings

are defined, auto-focusing algorithm is employed to focus beam down to sub-20 nm level.

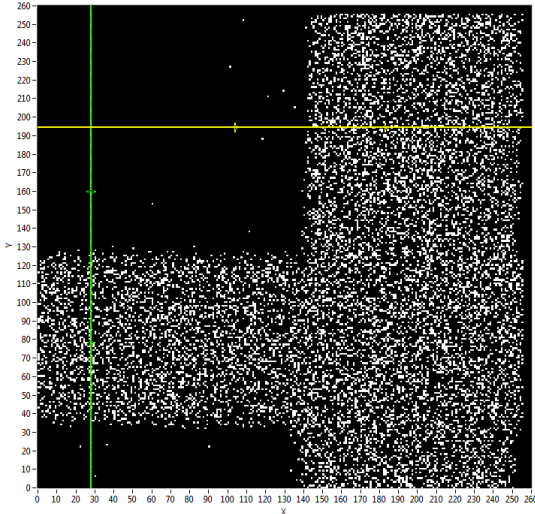


Figure 3-22. Rough Focusing using STIM Image and manually adjusting quadrupole lenses.

During the manual focusing, a sharp grid image (off-axis STIM) is obtained by manually adjusting the quadrupole power supplies. Quadrupole excitation can be adjusted using a serial interface to the power supplies (120 A at 2 ppm stability from Bruker, W1214496). Through this remote control, current output can be initialized and changed through steps of 0.02 A or 0.04 A or any user defined value in the output range. Rough focusing can be achieved down to sub-micron beam spot sizes. Figure 3-22 shows a resulting grid image of Ni resolution standard with a spot size of  $265 \times 365 \text{ nm}^2$  measured for a 2 MeV H<sup>+</sup> beam by manually varying the quadrupole power supplies using Trek and Techtron amplifiers for X and Y directions respectively. A scan size calibration was performed before the beam spot size measurement.

Autofocusing algorithm is based on finding the quadrupole currents required to attain smallest beam spot defined by system demagnification. Automated focusing is done in iterative mode wherein number of loops indicate the number of iterations required for autofocusing. For every successive iteration, the step size in amperes of the corresponding power supplies is reduced to half of the previous iteration. The number of iterations is limited by the noise level of the power supply (0.001 A). The algorithm has been shown to focus beam down to  $9.3 \text{ nm} \times 32 \text{ nm}$  for a 2 MeV proton beam [134].

An auto focusing step begins after defining the edge locations to be scanned on the resolution standard image by drawing cursors (shown in Figure 3-23 as Yellow and Green marker lines). A line scan is acquired in each direction for the corresponding quadrupole current and beam FWHM is extracted. Each loop in the iteration sweeps the quadrupole currents by half the step size of the previous iteration. Using this method, system reaches the defined minima in the search space.

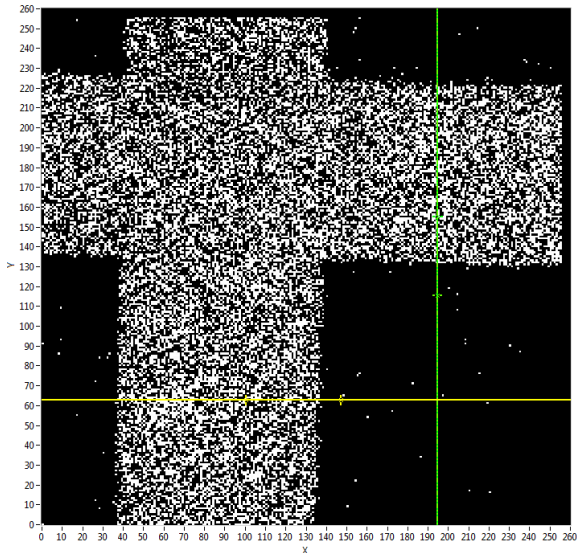


Figure 3-23. STIM Image of Ni Resolution standard after autofocusing with objective and collimator opening of  $30 \times 20 \mu\text{m}^2$  and  $60 \times 60 \mu\text{m}^2$  respectively.

The voltage required to scan along the edge is determined from the cursor positions and digitized, but limited by the noise level of the analog output that can be generated by the data acquisition card. Figure 3-23 shows an off-axis grid image after autofocusing with objective and collimator apertures set to  $30 \times 20 \mu\text{m}^2$  and  $60 \times 60 \mu\text{m}^2$ . FWHM measured from Figure 3-23 are  $56 \times 160 \text{ nm}^2$  close to the demagnification value of the system ( $857 \times 130$ ). Pixel resolution of the line scans used for autofocusing were 11 nm and 9 nm in X and Y directions respectively.

Smaller spot size is then achieved by reducing the objective and collimator apertures to  $8 \times 4 \mu\text{m}^2$  and  $20 \times 20 \mu\text{m}^2$ . The final autofocusing is done by reducing the scan size to  $2.95 \times 2.57 \mu\text{m}^2$  using Techron amplifier for both scan directions to lower the noise and improve the pixel size to 1 nm.

Line scans are displayed at the bottom right tab in Beam Profile (Figure 3-19). For every value of change in quadrupole current, a line scan is generated and

displayed. The line scan is fitted using Levenberg-Marquardt Algorithm (non-linear curve fitting) using equation 2.19 for STIM and equation 2.21 for edge enhanced secondary electron detection. Beam FWHM is extracted from the line scan and displayed on the beam size indicators. Ion induced secondary imaging shows an edge enhanced line scan due to electrons emitting from the grid bars adding to the line scan. Therefore, the fitting function control (detector selection) is modified to consider the edge enhancement for secondary electron imaging. Pixel size for the line scan is displayed along with the line scan to show the accuracy of extracting beam FWHM. This pixel size is limited by an effective DAC resolution of 13 bits. Apart from an automated scan calibration, a manual control for scan size control is implemented as an override in case the automated scan calibration doesn't work.

Figure 3-24 shows an on-axis image of a Ni resolution grid (1  $\mu\text{m}$  thickness) taken with scan area of  $800 \times 800 \text{ nm}^2$  and 256 pixels (3.25 nm per pixel). Also shown are the line scans extracted from the image. A spot focus of  $17 \times 35 \text{ nm}^2$  with object sizes  $8 \times 4 \text{ } \mu\text{m}^2$  and collimator of  $20 \times 20 \text{ } \mu\text{m}^2$  with a reduced brightness of  $6.99 \text{ A}/(\text{m}^2\text{srV})$ . Beam focusing is close to the expected beam spot size of  $9.3 \times 23 \text{ nm}^2$  based on the demagnification of the optical configuration of the spaced oxford triplet. Limitations of the focusing depends on the quality of the slits, reduced brightness, and motion of the stage during image acquisition as well as thermal stability of the quadrupole lenses.

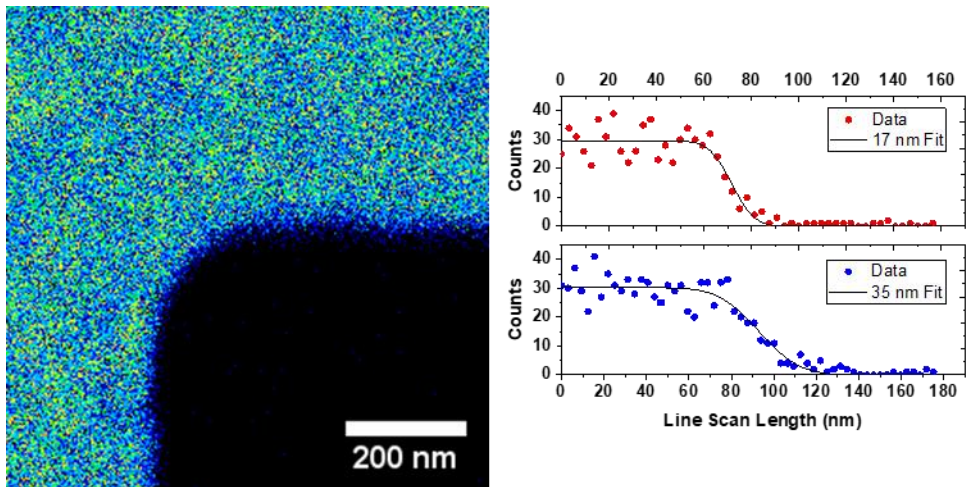


Figure 3-24. Off-axis STIM image of Ni resolution standard images using  $800 \times 800 \text{ nm}^2$  scan area at 256-pixel resolution

Table 3-2. Beam parameters used for focusing

Beam, Energy	$\text{H}^+, 2 \text{ MeV}$
Object Slit opening	$8 \times 4 \mu\text{m}^2$
Collimator Slit opening	$20 \times 20 \mu\text{m}^2$
Expected Beam Size	$9.3 \times 23 \text{ nm}^2$
Scan Size (256 pixels)	$800 \times 800 \text{ nm}^2$

### 3.7 Writing strategy

The interface also integrates nano-positioning control for the PI stages in a single interface. Stage control allows user to position the samples/grid in scan field. Lithography tab allows users to use any of the two modes of lithography (stage scan or beam scan). The tab allows user to upload the files for writing either using beam scanning or stage scanning (refer Figure 3-25).

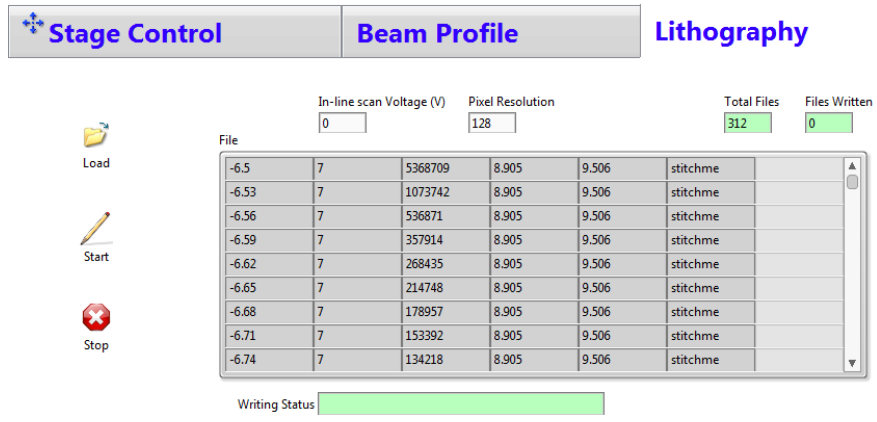


Figure 3-25. Lithography tab from the interface for step and repeat, and stage scan

There are two modes of writing available in the beam line. For writing arbitrary feature with limited scan fields (up to  $130 \mu\text{m}$ ), beam scanning is employed wherein an input scan pattern is generated using either bmp file/EPL scan format developed earlier ([144]). Writing rectangular features over mm range can be done using stage scan. During such a scan the stage is moved from one end of the rectangle length and beam is scanned orthogonal to the stage motion.

### 3.7.1 Step and repeat

An input file with a list of X and Y coordinates of the centre of the scan fields is uploaded to the lithography tab. Multiple scan files can be loaded in one go to be scanned and written. This method allows the user to employ a step and repeat lithography for writing features in an area up to  $130 \times 130 \mu\text{m}^2$  over stage travel area of  $20 \times 20 \text{ mm}^2$ . In this function, the beam is typically scanned up to  $130 \mu\text{m}$ , limited by beam spot deterioration, then the stage is stepped or positioned to the next centre. There is always a stitching factor involved in the stepping of the stage. Stitching error is defined as the gap or overlay of the two adjacent scan fields. An alignment error is estimated from the stitching error in

orthogonal direction for each direction. The input parameters for the step and repeat method are the field centre coordinates, digitized pattern to scan, frequency of scanning (equivalent of dwell time per pixel) and voltage range in X and Y to be amplified by the amplifiers. A scan pattern is generated in bitmap format and converted to an EPL format using Ionutils program developed by Andrew *et. al.* [145]. This scan pattern contains the digital map of the pattern to be scanned and beam blanking information. The system supports a maximum of 13-bit scanning limited by the DAC resolution of the scan amplifier input. During scanning the uploaded scan pattern is converted to a scan voltage map with beam blanking signal corresponding to every pixel being either 1 or 0 (an equivalent of 5 V or 0 volt input to the Fischer amplifier, slew rate of 1000V/ $\mu$ s). Maximum frequency allowed for scanning is dependent on the slew rate of both the scanning and blanking amplifier which limits the scan frequency at 1 MHz (1  $\mu$ s per pixel). Pixel size in scanning is determined by the resolution of the scan pattern file. For instance, a 4096 resolution for a 4  $\mu$ m scan size implies 0.97 nm per pixel. Dimension of the feature defines the number of pixels required for the feature. For uniform dose deposition, it is required to have pixel size smaller than the beam size such that two adjacent pixels have overlapped scanning. The dwell time (frequency) is calculated from the required dosage, pixel area required to reach the target dose.

### 3.7.2 Stage scan

Rectangular features can be written over mm lengths by moving the stage at appropriate velocity that corresponds to the dose required to fabricate structures. In stage scan method, initial and final position of the coordinates are given with velocity and scan voltage control. During the stage travel, beam can be scanned

in orthogonal direction allowing to fabricate rectangular lines or channels for the photo-resists. Typical applications that benefit with stage scanning include nanoimprinting, waveguide fabrication, resolution standard writing and mask fabrication.

Factors limiting the writing capability that we found include the uniformity of stage velocity. If the beam size in stage travel direction doesn't overlap for the time it takes to deposit the dose in orthogonal directions, gaps or wavy structures will be fabricated. Figure 3-26 shows a grid pattern fabricated in 2  $\mu\text{m}$  thick PMMA spin coated on top of Cr-Au-Cu written using 1 MeV alpha focused to 106 nm  $\times$  361 nm with a reduced brightness of 2.96 A/m<sup>2</sup>srV. Bar width was intended to be 4  $\mu\text{m}$ .

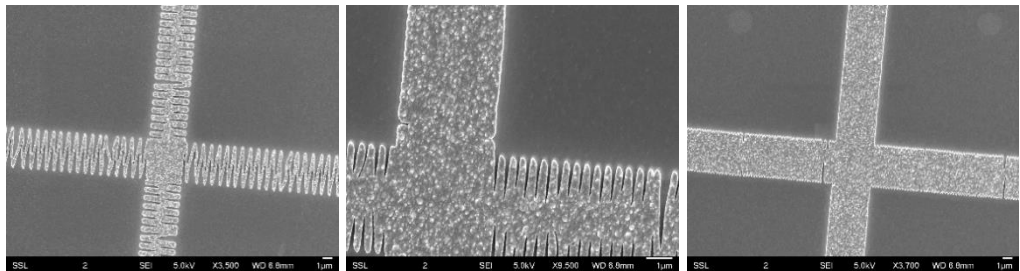


Figure 3-26. Effect of stage velocity on pattern writing in resist. Non-overlapping beam scans lead to gaps in resist region expected to be exposed.

When the time required to scan from top to bottom or left to right is more than the time stage moves more than the beam size in the direction of stage motion, features are non-overlapping. This adds to the sidewall roughness in the structure on the edge as also noted by Sum *et. al.* [146]. Table 3-3 lists the parameters for the writing and stage motion during single beam scan length. As the scan window becomes comparable to the beam size, the period of the triangular wave diminishes. This should be considered for writing structures

such as waveguides where transmission losses are increased owing to higher edge roughness.

Table 3-3. Stage motion for single beam scan length

Dose (nC/mm <sup>2</sup> )	Pitch X (nm)	Pitch Y (nm)	Stage Velocity (μm/s)	Stage motion per scan (nm)
7.5	832.61	765	40	409.6
15.1	382.7	0	20	204.8
22.6	278.29	0	13	133.12

Besides the beam scan parameters required to overlap features, non-uniformity of stage velocity limits the line width across the length of the scan and might leave gaps during writing. This limitation can be observed across photo-resists with negative and positive tone. Figure 3-27 shows the frequency of these gaps or patches in photo resists left after development along the length of the scan. These gaps can be explained from the varying stage velocity. PI controllers used for the positioning are designed for positioning and not scanning. Thus, as the stage is scanned, the position is tracked. Due to the controller lag in tracking current position, the velocity profile is not uniform throughout the scan length. This acceleration and deceleration leaves the photo-resists unexposed in parts where the dose deposited is below the critical dose.

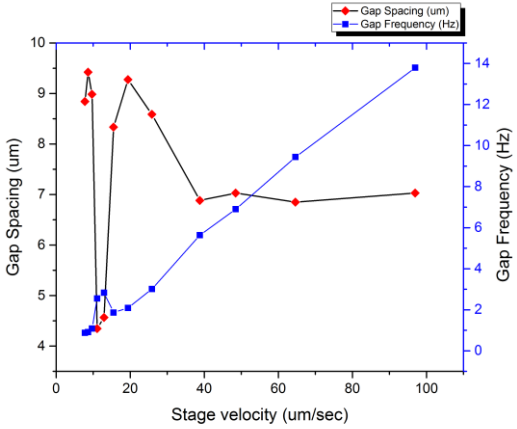


Figure 3-27. Gap spacing and frequency observed in PMMA after development.

### 3.8 Stitching

Limited by the maximum scan size, larger fields can be written with step and repeat method as described in the earlier section. However, positioning accuracy and alignment of the scan fields with the stage motion axis limit the accuracy of the stitching of two adjacent scan areas. To test the stitching error, we fabricated four scan fields each of  $50 \times 50 \mu\text{m}^2$  area. Each scan area contained two orthogonal lines. A beam of 2 MeV  $\text{H}_2^+$  ions was focused to  $100 \text{ nm} \times 400 \text{ nm}$  using a reduced brightness of  $2.8 \text{ A/m}^2\text{srV}$ . Figure 3-28 shows the image of the Ni grid using on-axis STIM with a scan area of  $25 \mu\text{m} \times 25 \mu\text{m}$  at a pixel resolution of 12.2 nm.

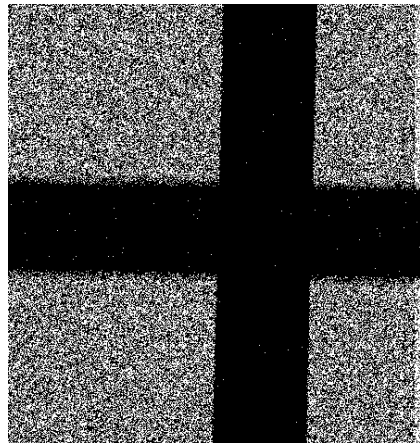


Figure 3-28. On-axis STIM image of Ni resolution standard.

Dose was varied from 6,000 protons/ $\mu\text{m}$  to 200,000 protons/ $\mu\text{m}$ . The sensitivity of this batch of HSQ was found to be 50,000 protons/ $\mu\text{m}$  equivalent of 80 nC/mm<sup>2</sup>. A typical SEM image corresponding to a dose of 240 nC/mm<sup>2</sup> is shown in Figure 3-29 with the four cross regions written using step and repeat. After writing the top left cross, the stage was positioned at the bottom left, followed by bottom right eventually exposing the top right scan region.

Table 3-4 shows the average stitching error measured across 5 dose regions. An overall stitching error of  $97 \pm 23$  nm in X direction and  $523 \pm 115$  nm has been achieved with the step and repeat method. Stitching error in Y direction is the result of stage moving against gravity and the alignment error can be attributed to rotational misalignment of the electrostatic scanner with respect to the quadrupole.

Table 3-4. Summary of stitching error with step and repeat lithography

	Stitching X (nm)	Stitching Y (nm)	Alignment error X in Y	Alignment error Y in X
Average	97	523	495	307
Standard Deviation	23	115	91	207

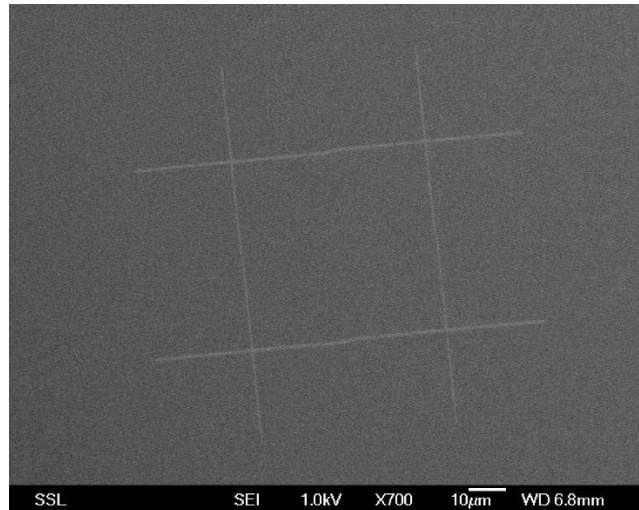


Figure 3-29. SEM image of developed cross written at dose of 240 nC/mm<sup>2</sup>.

### 3.9 Fabrication of resolution standard

Beam focusing is dependent on the side wall slope of the resolution standard. Resolution standards fabricated using proton beam writing have vertical side walls and smooth edges due to the limited extent of secondary electrons along the track of protons. Secondary electron yield for Au is higher than for Ni for keV to MeV ions due to higher electronic stopping power. We combined the two advantages and fabricated a Au resolution standard.

### 3.9.1 Fabrication of Au resolution standard

A modified process for fabrication of a resolution standard is described in this section. A silicon wafer was cleaned in acetone and IPA, next it was baked at 200° C for 2 minutes followed by 10 nm Cr, 30 nm Au and 50 nm Cu coating using magnetron sputtering. 2  $\mu\text{m}$  thick PMMA A11 950k was spin coated at 4000 RPM after metal coating. A 2 MeV beam of proton focused to 400 nm  $\times$  400 nm was used to expose a 300  $\mu\text{m}$   $\times$  300  $\mu\text{m}$  field of grid pattern with 5  $\mu\text{m}$  bar width and 25  $\mu\text{m}$  pitch in 2  $\mu\text{m}$  thick PMMA. With a count rate of 1.05  $\times$  10<sup>8</sup> protons/s, a dose of 250 nC/mm<sup>2</sup> corresponding to a stage velocity of 13.5  $\mu\text{m}/\text{s}$  was used for stage scanning while the beam was scanned perpendicular to the stage scan direction. Beam scan area was set by the scan voltage corresponding to a scan area of 5  $\times$  5  $\mu\text{m}^2$ . Following exposure, the sample was developed in IPA:DI water (7:3) for 5 minutes. A Au coating of 180 nm thickness was sputter deposited after sample development. PMMA was stripped using acetone, resulting in Au lift-off leaving only the Au grid bars on the sample. A thickness ratio of 1:10 (Au:PMMA) is empirically found to be a safer limit for Au lift-off with PMMA.

A 30  $\mu\text{m}$  thick layer of AZ-40XT was used to expose a supporting grid structure and Ni electroplating (Technotrans AG, RD. 50 at a current density of 10 mA/cm<sup>2</sup>) was carried out after UV (365 nm) exposure and sample development. After Ni electroplating, AZ-40XT layer was stripped in acetone for 40 minutes at room temperature. Finally, the sacrificial Cu layer was etched at room temperature using a mixture of acetic acid (5% vol): hydrogen peroxide (5% volume): DI water (90% volume). The etching takes 45 minutes with no effect on both Au and Ni features. Figure 3-30 shows SEM images of the fabricated

Au grid. The grid bars are orthogonal, and thickness was confirmed to be 190 nm  $\pm$  10 nm based on the method described earlier [147].

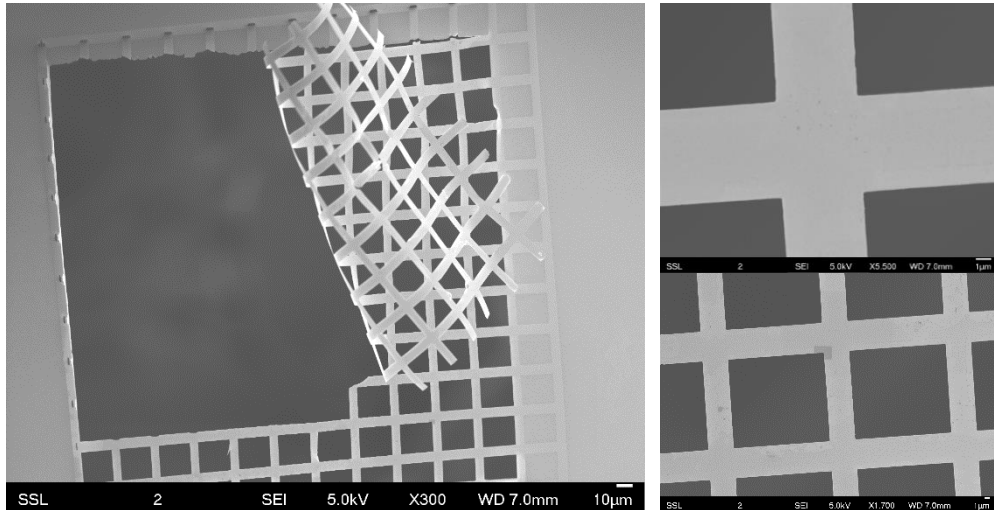


Figure 3-30. SEM images of Au grid. (a) Full grid image showing the portion of grid folds on itself due to stress owing to poor support from the Ni frame. (b) and (c) shows high resolution images of the bottom right corner of the resolution which can be used to focus ion beams using STIM and Secondary electrons.

On axis STIM spectrum with a beam of 500 keV H<sub>2</sub><sup>+</sup> is shown in Figure 3-31. This is the thinnest grid fabricated so far using proton beam writing and can be used to focus MeV ion beams. The Ni supporting grid adhered properly to the Au grid till it was mounted on the holder. One corner of the grid peeled off from the Ni layer. This can be either due to lattice mismatch between Au and Ni or due to stress from the supporting Ni structure on the thin Au grid or due to the limited overlap during supporting Ni grid alignment. More experiments are planned to test the minimum thickness allowed by maintaining proper support from the adjacent Ni grid.

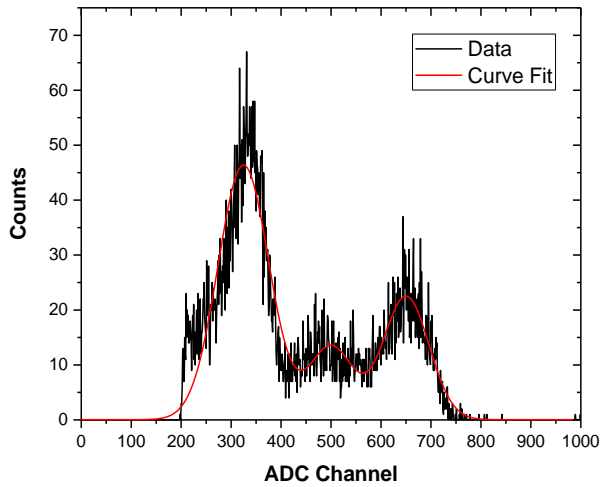


Figure 3-31. Thickness measurement of Au grid using method described in section 2.3

### 3.10 Secondary electron efficiency from Ni and Au grid

Ability to focus ion beams with a given demagnification is limited by the source brightness [148]. Additionally, chromatic aberration of the beam, partially induced due to slit scattering, adds a halo to the beam spot in the image plane [130]. The transparency region in slits [130], was measured to be  $\sim 20 \mu\text{m}$  with no focusing action by quadrupole lenses [149]. However, in active focusing scenario, we observed a narrow transparency region ( $\sim 1 \mu\text{m}$ ) for molecular beams (refer Figure 3-12). Molecules dissociated through slit scattering are filtered out by the quadrupole lenses, thereby reducing the beam halo. At smaller slit openings, ion count rate reduces to a few thousand ions per second. This increases the time to acquire the image during which time stage motion makes it difficult to focus the beam with a 70% or higher goodness of fit. To alleviate this, an annular Micro Channel Plate (MCP) detector in Chevron configuration [150] was installed in the end station [138] in the hope to get a better collection efficiency and estimate the beam size faster. Secondary

electrons induced by ions hitting the grid bars are collected by the MCP connected to a pre-amplifier and counter.

Secondary electrons emitted from metal resolution standards can be used to image and focus ion beams. The energy transmitted to the electrons of the metal goes towards generation and transport of the delta electrons. These electrons then overcome the barrier on the surface and escape to the vacuum. Channel Electron Multiplier (CEM) detectors have been used in the past to collect these secondary electrons and for focusing. However, they offer low electron yield per protons and is susceptible to magnetic fields around the chamber.

MCP offers higher gain by reducing the size of the channels and having large number of these parallel channel to detect and amplify the charge through the accelerating field applied across the plates. A typical MCP plate has 15  $\mu\text{m}$  diameter channels of high electron yield material coating on the interior of the channels. Besides the gain of the plate exponentially varies with the applied voltage across the plate. Chevron configuration stacks two such MCP and apply voltage to further increase the gain. Typical gain ranges from  $10^6$  to  $10^7$  for a bias of 1 kV per plate. The geometry of the anode plate (collector) defines the mode MCP plates are used. Mesh anode plates are used for position sensitive imaging wherein imaging resolution is defined by the spacing between two microchannels. A solid blank collector plate detects only the total charge amplified by the MCP. This results in loss of position sensitivity. However, for applications such as proton beam writing, scan resolution of few nm is required. Therefore, using an MCP in imaging mode is not applicable. Furthermore, using MCP as charge collector simplifies the collection as it is synchronized with the

beam scanning control. This method is although sensitive to a broad range of electrons which are incident on the front plate but offers higher gain for operation.

Electron detection efficiency of an MCP is highly sensitive to the bias voltage applied and the inter-plate acceleration voltage [150] (refer Figure 3-32 inset for MCP schematics). More electrons are accelerated and collected on the front plate leading as the bias voltage is increased. However, the gain of the MCP reduces since the voltage across the two is reduced. This leads to a competing effect and thus optimization of the bias and applied voltage is required to achieve higher collection efficiency. A 1 MeV  $H_2^+$  beam was used to image the Ni grid with a molecular count rate of 3400 per second. MCP bias voltage to the front plate was varied from 0 to 800 V in steps of 50 V at a fixed back plate voltage of 2800 V. Figure 3-32 shows the variation in secondary electron detection per proton, collected by the MCP as a function of bias voltage.

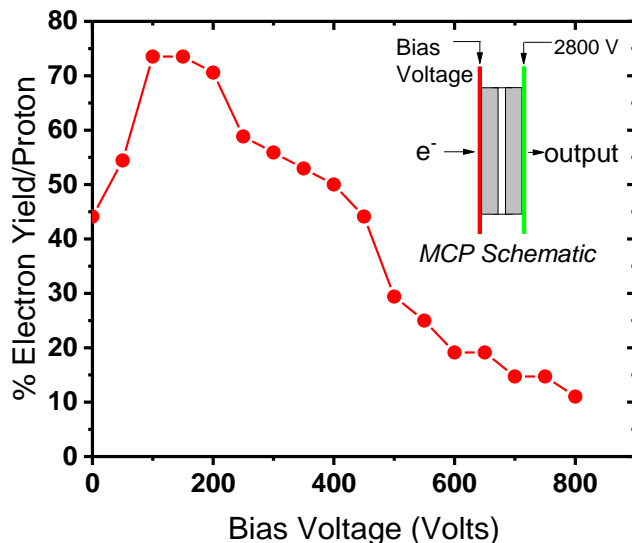


Figure 3-32. Collection efficiency of MCP as a function of bias voltage

For an applied bias of 100-150 V, there is an enhancement in detection as more secondary electrons are attracted towards the front plate of the MCP. Further increasing the applied bias voltage, beyond 150 V, reduces the inter plate accelerating voltage, and thereby reduces the yield of secondary electrons within the micro channels. Therefore, an optimal bias of 100-150 V at a back-plate voltage of 2800 V results in improved [22] detection efficiency (75%) of secondary electrons per proton. Tuning the bias voltage of the MCP is advantageous over STIM using PIN diode which is prone to detector damage at high count rates.

Empirical models have been suggested for the emission of secondary electrons from different materials. Metals are known to have lower secondary electron yield compared to insulators owing to higher concentration of electrons in the conduction band. This results in increased number of collisions for the electrons emitted due to ion collision, and the delta rays interact more with the conduction band electrons. This causes the emitted electrons to lose more energy, thereby lowering the number of electrons that can overcome the surface potential barrier required for emission into the vacuum. However, metal resolution standards are easier to fabricate due to optimized processes and methods available to deposit metal layers after lithographically defining the features in a photo resist post development. Methods such as electroplating and sputter deposition are common practices to deposit metal layers down to 200 nm thicknesses.

Hasselkamp *et. al.* [151], [152] demonstrated the variation of secondary electron yield versus atomic number for various metallic substrates. The conclusion does not follow a general trend that could be explained based on

empirical model developed by Sternglass [153]. This can be explained due to the lack of free electron model applicability for the metal substrate, which could predict the yield to be lower as the density of electrons in metal substrate increases. However, the ratio of secondary electron yield and the stopping power of the ion in the material stays constant for varying energies [154]. This leads to a possibility of higher secondary electron emission yield induced by ion beams if the stopping power of the ions in the material is higher. Also measured experimentally by Hasselkamph [151], one can see using the trend observed by Hasselkamp, that since the stopping power of protons is higher in Au than Ni. This should lead to an increased electron yield. Also, as the energy of the ion is increased, the stopping power for proton decreases. This should lead to a reduction in the secondary electron yield.

We measured the secondary electron collection efficiency of MCP for Au and Ni resolution standard for varying incident proton energies. Figure 3-33 shows the collection efficiency of protons at various energies for Au and Ni resolution standard fabricated using proton beam writing.

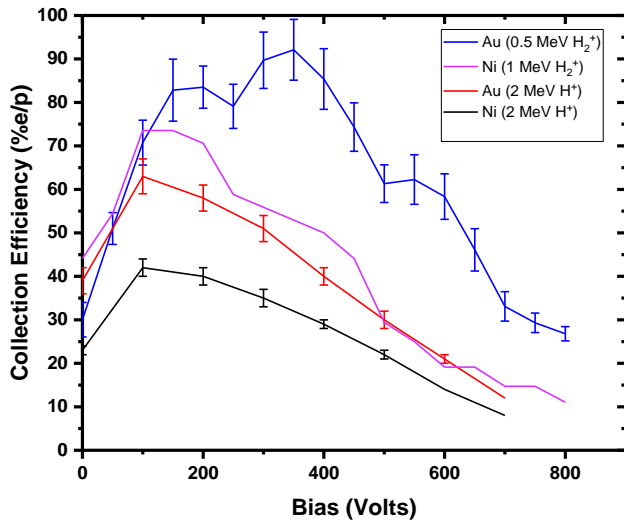


Figure 3-33. Collection Efficiency as a function of bias voltage applied to the front plate for increasing incident beam energy

As is evident from the graph, the collection efficiency of lower energy protons is higher than that of higher energy protons. Also, it should be noted that the electronic stopping power of protons in Ni and Au decreases with increasing energy. This observation combined with ratio of the true yield and stopping power should imply that the yield for Au is higher than that of Ni. This should be advantageous for imaging in proton beam writing or any proton beam application at lower energies. Figure 3-34a shows the image of the Au resolution standard imaged using 350 V bias voltage at a collection efficiency of 92% electrons per proton. Line scans were extracted from the image that shows a beam focus of  $46 \times 78 \text{ nm}^2$ . Figure 3-34b shows the STIM on-axis image of the same spot, also showing the same beam size estimation.

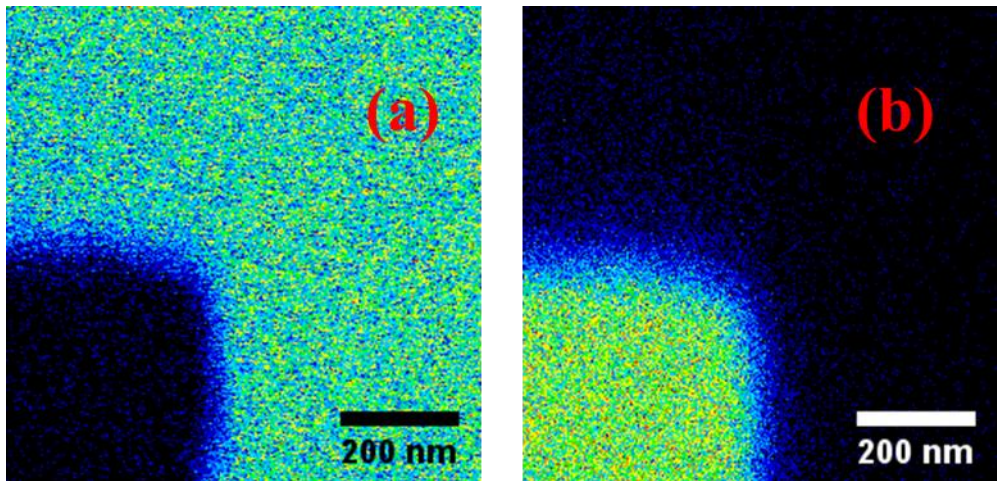


Figure 3-34. (a) MCP image for  $500 \text{ H}_2^+$  (350 V bias, 2800 V accelerating voltage, 3800 cps). (b) On-axis STIM image of the same spot.

### 3.11 Summary

In this chapter we showed a closed loop implementation for positioning sample in focal plane with a resolution of 500 nm. Through STIM characterization, we experimentally measured the thickness of Ni resolution standard to be  $0.9 \pm 0.1 \mu\text{m}$  and a side wall slope estimate of  $6.0 \pm 0.6 \text{ nm}$ . A quadrupole system alignment using STIM was described which is shown to be effective in removing higher order misalignments. A beam focusing of  $13 \times 32 \text{ nm}^2$  was achieved in agreement with the system demagnification. Using automated slit alignment and focusing, we showed an optimal focusing of  $23 \times 35 \text{ nm}^2$ . Performance of step and repeat down to sub-100 nm stitching error was discussed. Fabrication of 190 nm thick Au grid was described. Enhanced secondary electron collection of 92% electrons per proton was shown.

## 4 Applications of PBW in Resist Materials

Proximity free and high aspect ratio nanofabrication has been shown in HSQ and PMMA down to 19 nm and 65 nm. Smallest spot size shown for a focused beam is 9 nm x 32 nm. In this chapter, we discuss nanofabrication in resists using the optimization discussed in last chapter. Fabrication of 30 nm channels in PMMA and subsequent ridge transfer through Ni plating will be discussed in section 4.1. Nanoimprinting master fabrication for single DNA extension will be discussed in section 4.2. Using resist molds, we demonstrate pattern transfer to Ormostamp ridges down to 42 nm. PBW combined with electrochemical etching will be shown in Si down to 100 nm. Optimization of waveguide in STO will be discussed.

### 4.1 General processing for PBW

Here we describe typical proton beam writing experiment and highlight the critical steps which pose limitation towards nanofabrication.

#### 4.1.1 Sample preparation

Photoresists are typically spin coated on top of Si wafer. Wafers are typically cleaned in acetone and IPA for 30 seconds each and baked at 150° C to get rid of all the moisture. Samples are handled in class 1000 cleanroom to avoid contamination of the substrate. PMMA and HSQ are the widely used resists which are used to fabricate high resolution nanostructures. Resist is spin coated on the substrate and pre-baked on top of a hot plate. For instance, 2  $\mu\text{m}$  thick PMMA (Microchem, 950k, A11) is spin coated at 4000 RPM and pre-baked at 180 °C for 180 s. Depending on the intended thickness, different composition of HSQ (XR-1541) in MIBK is used. XR-1541 002 has been used to get a film

thickness of 80 nm. HSQ samples are pre-baked at 95 °C for 1 min. Although HSQ has been shown to give higher resolution than PMMA, its dose response is not reproducible from batch to batch due to cross-linking and higher temperature sensitivity. Limited shelf life of the resist also causes loss of sensitivity over time. Besides, delay between coating and exposure has been shown to degrade contrast [24].

#### 4.1.2 Metal seed layer deposition

PMMA films are used towards resolution standard fabrication and require a seed electroplating layer. This electroplating seed layer is coated using a DC magnetron sputtering machine which can coat layers of Cr, Au, Cu, Ti and C with deposition rates of 1 nm/sec. Typically, a 30 nm Cr and a 30 nm layer of Au leads to better conductive surface during electroplating. For fabrication of free-standing stencils and grid, a 50 nm sacrificial layer of Cu is deposited on Au. Ti was used a base layer to improve adhesion of HSQ on Si substrate. Adhesion of PMMA films on various substrates have been known to be challenging.

#### 4.1.3 Proton beam writing

$H^+$  or  $He^+$  ions are accelerated in the energy range of keV to MeV. A transmission ratio of 50-60% is observed for  $H_2^+$  ions from Faraday cup 1 to faraday cup 2.  $H^+$  beam was observed to have a maximum of 50% transmission with longer running of the RF ion source. Automated alignment and focusing are used to focus beam down to sub-20 nm using STIM or ion induced secondary electrons, with typical reduced brightness of  $10 \text{ A/m}^2\text{srV}$ . The focusing performance of ions is limited by the reduced brightness and quality

of the slits used as objective and collimator apertures. Scan size is calibrated using automated routine discussed previously.

#### 4.1.4 Exposure files

Arbitrary nano/micro-structures can be fabricated using step and repeat which employs beam scan and stage stepping. Linear structures can be written using stage scan combined with beam scan in the orthogonal direction. Scan patterns for beam scan are generated by writing an EMC file [144], or a monochrome bit-map file. The resulting file is then converted into a binary file of coordinates with blanking index (EPL) to scan the beam in the area of interest using Ionutils [144]. Multiple such files can be written in a single exposure by defining the stage coordinates, dwell frequency, and EPL file path. Stage scan is done by defining the direction of motion, initial and final coordinates, and scan size of beam in orthogonal direction.

#### 4.1.5 Electroplating and copper etching

PMMA samples are developed in IPA:DI water (7:3 volume ratio) for 2.5 mins. To make good contact with the seed layer, sample edges are exposed with UV (365 nm) and developed in PMMA. Samples are mounted on a Pt chuck and copper tape makes the seed layer conductive. Ni electroplating is done using Technotrans AG which supports DC and AC electroplating with a noise level of 1 mA upto a maximum of 4 A. Typical plating rates are 200 nm/min at a current density of 10 mA/cm<sup>2</sup>. A plating bath composition is nickel sulfamate, nickel chloride and boric acid such that the concentration of Ni is 90 g/l, Cl is 4 g/l and B is 6.96 g/l at a pH of 3.5. After electroplating and stripping resist, sacrificial copper layer is etched using a mixture of acetic acid: hydrogen

peroxide: DI water (5:5:90 volume ratio). The etchant is selective to copper and etching rates of 200 nm/min are reported.

## 4.2 PBW in PMMA

### 4.2.1 Nanograting fabrication

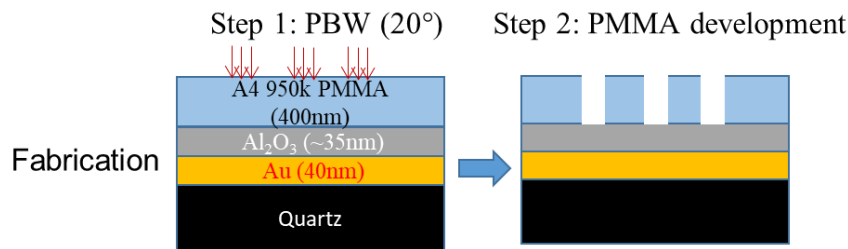


Figure 4-1. Fabrication flow of a nanograting in PMMA

PBW was performed in PMMA for testing resolution and beam uniformity over larger scan sizes for the 20° PBW beamline. Step and repeat scheme is demonstrated in 400 nm thick PMMA (A4 950k) spin coated on the sample prepared in Graphene Centre, NUS for the deposition of Al<sub>2</sub>O<sub>3</sub> and Au layer (refer Figure 4-1) using atomic layer deposition. Nanograting with lines of 200 nm and 300 nm spacing were written using a beam of 1 MeV H<sub>2</sub><sup>+</sup> ions focused down to 100 nm.

Figure 4-2 shows a schematic of the structures written in a 400 nm thick PMMA. The nanochannels are 200 nm wide at 500 nm pitch written in a total area of 500 μm by 100 μm. Each scan field was kept 100 μm by 100 μm and stage was stepped 100 μm to the next centre field. Pattern was digitized to 1024 × 1024 pixels equivalent of 100 nm × 100 nm pixel area.

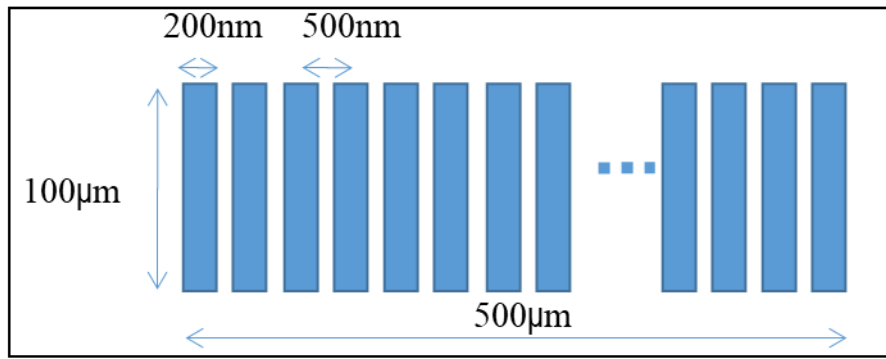


Figure 4-2. Figure schematic for the step and repeat algorithm

Each line was two-pixel wide and a space of 3 pixels was maintained between two lines. For a dose ‘D’ (nC/mm<sup>2</sup>), channel width ‘W’ (mm) and length ‘L’ (mm), time to write one channel, t (s) can be calculated from the equation:

$$t(s) = D \times W \times \frac{L}{C \times 1.6 \times 10^{-10}}$$

A summary of fabrication parameters for the nanograting in PMMA is described in Table 4-1. A high-resolution SEM image is shown in Figure 4-3 of the fabricated structure developed in IPA: DI water 7:3 ratio by volume. Also shown is a larger region showing the uniformity of writing field and beam stability for fabricating larger scan areas over time.

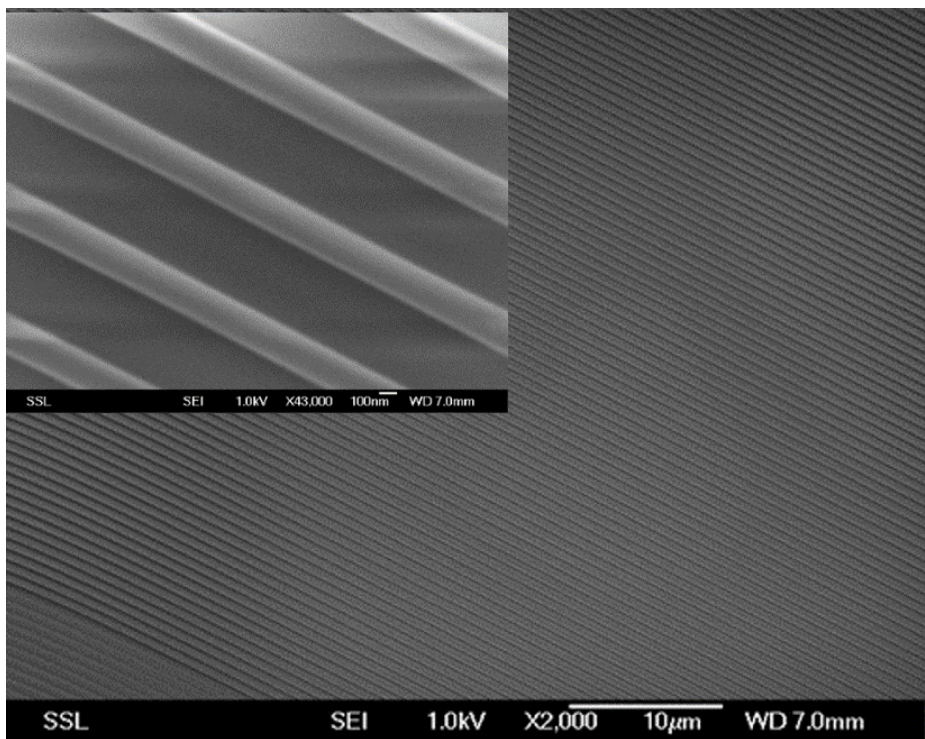


Figure 4-3. Nanograting (200 nm channels and 300 nm spacing) fabricated using Step and repeat algorithm. A field of 100  $\mu\text{m} \times 100 \mu\text{m}$  is scanned for grating and the stage is stepped 100  $\mu\text{m}$  for writing the next field

Table 4-1. Step and repeat in 400 nm PMMA

Energy & Particle	1 MeV, $\text{H}_2^+$	1 MeV, $\text{H}_2^+$
Beam Size	$100 \times 450 \text{ nm}^2$ (3nm/pixel for measurement)	$100 \times 400 \text{ nm}^2$ (4nm/pix res.)
Count Rate	$4.29 \times 10^6$ protons/sec	$4.84 \times 10^6$ protons/sec
Reduced brightness ( $\text{A}/\text{m}^2\text{srV}$ )	4.55	10.23
Object Aperture ( $\mu\text{m}^2$ )	$44 \times 30$	$36 \times 24$
Collimator Aperture ( $\mu\text{m}^2$ )	$80 \times 80$	$70 \times 70$
Scan Size ( $\mu\text{m}^2$ )	$109.23 \times 98.86$	$101.156 \times 99.897$

Stage movement for stitching in X direction	100 $\mu\text{m}$	101.156 $\mu\text{m}$
Dose	150 nC/mm <sup>2</sup>	150 nC/mm <sup>2</sup>
Number of pixels per channel	2048 (2×1024)	2048 (2×1024)
Update time	60 $\mu\text{s}$	37.8 $\mu\text{s}$
Total time taken to write	1.77 hr	1.11 hr

In a separate experiment, similar nanograting were fabricated in 400 nm thick bi-layer PMMA (A4 950k on A4 495k) spin coated directly on Si wafer. Figure 4-4 shows the schematic of intended nanograting with 300 nm channels in PMMA and 200 nm spacing written in a field of 100  $\mu\text{m} \times$  130  $\mu\text{m}$ . The scan fields were separated by 20  $\mu\text{m}$  and scan size was kept at 130  $\mu\text{m} \times$  130  $\mu\text{m}$ . The stage stepping between the fields were kept 120  $\mu\text{m}$ . Furthermore, connecting micro-sized pads and lines were written using stage and beam scanning. Here the optimal dose was found to be 60 nC/mm<sup>2</sup> using a beam of 1 MeV H<sub>2</sub><sup>+</sup> focused to a spot size of 100 nm  $\times$  300 nm. Each channel was written with 3 pixels thereby showing an overlapping beam spot or pixels result in uniform lines over larger scan areas besides showing the reproducibility of the step and repeat method (optical image shown in Figure 4-5). The pattern collapse induced due to developer surface tension is observed in the centre of each exposed field after cleaning with DI water and drying with N<sub>2</sub>.

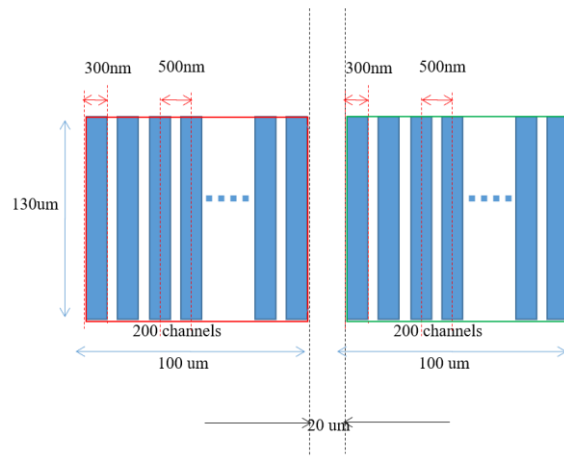


Figure 4-4. Schematic of nanograting (300 nm channels and 200 nm spacing)

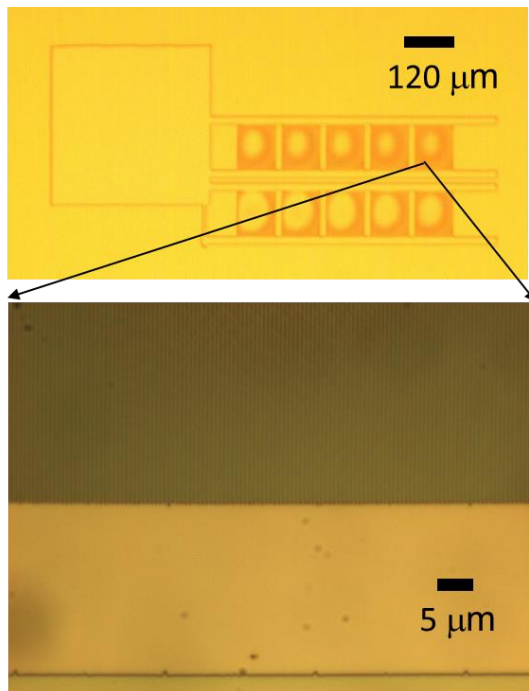


Figure 4-5. Fabricated Nanograting using step and repeat (full device view)

#### 4.2.2 High aspect ratio nano-channels fabrication

Electroplating seed layer of 30 nm Cr, 30 nm Au and 50 nm Cu was sputter deposited using magnetron sputtering. A 2 μm thick layer of PMMA 950k A10 was spin coated at 4000 rpm and pre-exposure done at 180° C for two minutes. Features down to 30 nm were written in PMMA using a beam of 2 MeV protons

focused to  $30 \text{ nm} \times 73 \text{ nm}$  beam spot. Object size was kept at  $16 \mu\text{m} \times 8 \mu\text{m}$  with collimator opening of  $30 \times 30 \mu\text{m}^2$  and a reduced brightness of 5.44 A/m<sup>2</sup>srV was measured. Five lines were exposed with a pitch of  $1 \mu\text{m}$  and  $15 \mu\text{m}$  long in a scan area of  $15 \mu\text{m} \times 15 \mu\text{m}$ . Scan file was defined in an EPL file with a scan resolution of  $512 \times 512$  pixels, equivalent to a pixel size of  $30 \text{ nm} \times 30 \text{ nm}$ . A single pixel was used to define the line width. To ensure uniform dose deposition, each dose was deposited in 10 passes. The dose was varied from  $5 \text{ nC/mm}^2$  to  $390 \text{ nC/mm}^2$  in steps of  $5 \text{ nC/mm}^2$ .

Sample was developed in 7:3 IPA:DI water mixture for 180 s. Ni electroplating was done to a thickness of 500 nm at a plating rate of 250 nm/min and current density of  $10.6 \text{ mA/cm}^2$ . SEM images were taken before and after stripping PMMA using acetone for 20 mins. Figure 4-6a and b show high-resolution SEM images of the 30 nm and 50 nm channels written using doses of  $85 \text{ nC/mm}^2$  and  $285 \text{ nC/mm}^2$  respectively showing the feature sizes close to the focused beam spot replicated in PMMA. This is the smallest feature size written in PMMA using proton beam writing so far.

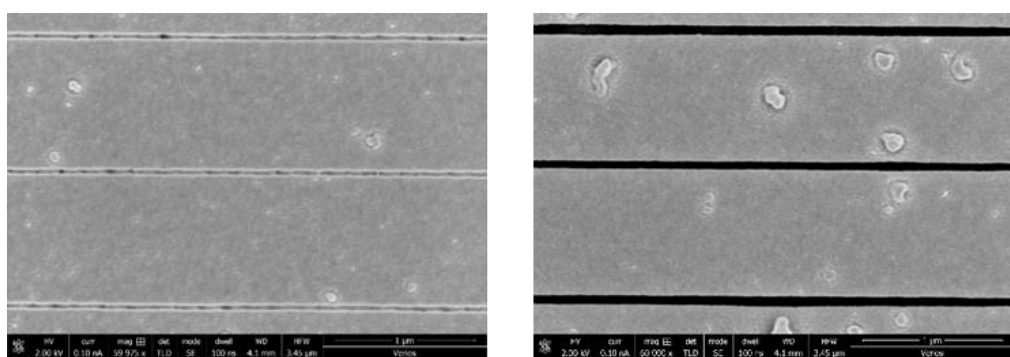


Figure 4-6. 30 nm channels in PMMA. 30 nm Channels in 2  $\mu\text{m}$  PMMA, 2MeV protons written using  $85 \text{ nC/mm}^2$

SEM images shown in Figure 4-7 post development and Ni plating showed Ni lines down to 40 nm width making the aspect ratio of (12.5 height : width) corresponding to a dose of 95 nC/mm<sup>2</sup>. Channels of 30 nm were not seen after PMMA stripping implying the channels were under-developed and thus, Ni plating could not be done in the channels due to lower exposure dose. The line width saturates as the dose increases implying the extent of the tail of the Gaussian beam profile which results from scattering of the slits used to define the beam shape in object and collimator limits the resolution for larger dosage.

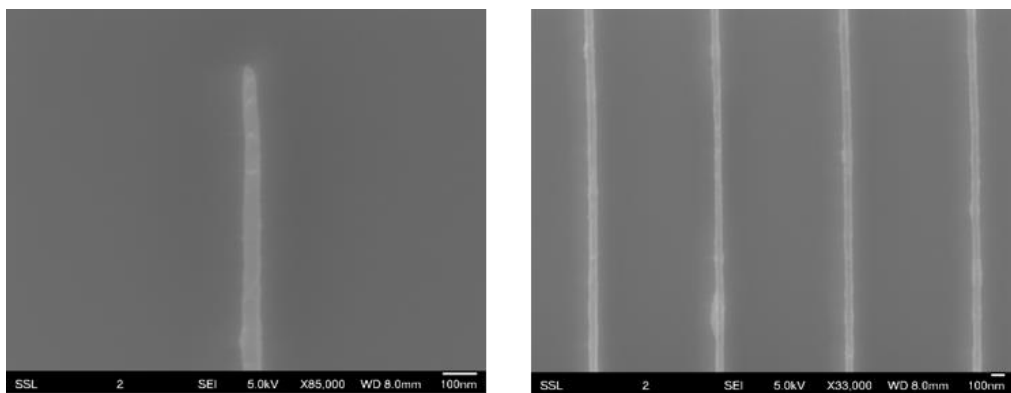


Figure 4-7. Ni lines after stripping PMMA. 40 nm ridge are seen in the image on the left, 50 nm ridges shown on the right at a dose of 285 nC/mm<sup>2</sup>

In a separate experiment stage scanning was used with 2 MeV proton beam focused down to 30 nm with the same sample geometry. A test was done to compare the performance of adhesion of PMMA on the resolution for electroplating. With the electroplating seed layer deposited on silicon wafer as described earlier, 2 μm PMMA layer was spin coated using spin coater which had been known to have poor adhesion of photo resists due to spin coating of Teflon for imprinting masters. Another sample with same seed layer was deposited with spin coater of no known Teflon usage. Same features were written on both the samples using the same beam using stage scan. To avoid

issues with the irregular stage motion discussed in section 3.7.2, the required line dose was deposited in four passes to get rid of the gaps due to non-uniform stage velocity during scanning. The stage was moved in Y direction while the beam was scanned in X direction corresponding to line widths of 30 nm, 50 nm and 150 nm at a dose of 100 nC/mm<sup>2</sup>. Both the samples were developed in IPA:DI water mixture with a 7:3 ratio by volume. 1 μm thick Ni electroplating was carried out at a plating rate of 500 nm/min using Technotrans plating machine. Acetone was used to strip the PMMA layer for 20 mins at room temperature. SEM images in Figure 4-8a and b show the Ni lines in the two samples. The sample which has better adhesion results in a resolution close to the beam spot size (~30 nm). Whereas, the sample which had poor adhesion to the substrate showed poor definition of the line width (200 nm). The Ni deposition is triangular on the poor adhesion sample as opposed to a well resolved line width. The aspect ratio of this feature is approximately 33. The periodic ripple or bumps in the line width are possibly due to stage rocking when the control accelerates to reach the target position leaving a higher dose deposition in the gaps. Since, two scans were done with the stage back and forth, synchronization of the gaps cannot be achieved. Implying the gap location is not periodic but has a range defined based on the velocity of the motion.

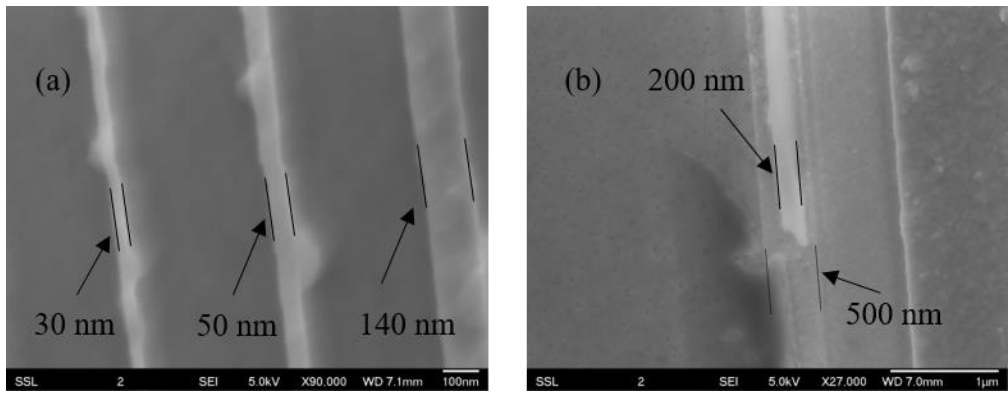


Figure 4-8. (a) 30 nm channels in 2  $\mu\text{m}$  PMMA, 2MeV protons written using 100 nC/mm<sup>2</sup>, 1  $\mu\text{m}$  Ni Plating – image after removing PMMA (b) Ni under-plating of 500 nm at the base

Poor adhesion leads to poor line width resolution defined after electroplating. Thus, adhesion of the resist film is an important consideration for both positive and negative resists.

#### 4.2.3 Nano-grating fabrication in PMMA

Nano-grating fabrication in PMMA for a pitch of 500 nm was shown in 400 nm thick PMMA resist (both bi layer and single layer) using a beam of 1 MeV  $\text{H}_2^+$  ions and written using step and repeat method. Here we show the resolution test of 2  $\mu\text{m}$  thick PMMA and the same pitch (500 nm). 2  $\mu\text{m}$  PMMA was spin coated on Si/Cr/Au/Cu substrate. A beam of 2 MeV protons was focused to 29 nm  $\times$  453 nm with a reduced brightness of 9 A/m<sup>2</sup>srV. A grid pattern with 5  $\mu\text{m}$  bar width and 25  $\mu\text{m}$  pitch was written using stage scan.

Gratings were written by positioning the grid window at the centre of beam scan (refer Figure 4-10 for layout). A scan size of 15  $\mu\text{m}$   $\times$  18  $\mu\text{m}$  was used to write gratings with line widths of 30 nm (1 pixel), 50 nm (2 pixels), 100 nm (3 pixels), 200 nm (6 pixels) and 300 nm (9 pixels). Two different pitches (500 nm and 1  $\mu\text{m}$ ) were selected per scan field. Ten lines were written for every dose, dose

was varied from 20 to 350 nC/mm<sup>2</sup>. Figure 4-11 shows the overall SEM of the sample after development and before Au sputtering of (200 nm on top). Au deposition was done to fabricate resolution standard using lift-off and Cu etching.

Figure 4-9 shows a high-resolution SEM image of the 200 nm channels written using 200 nC/mm<sup>2</sup> (2 pixel). It could be noted that as the aspect ratio increases, surface tension during drying leads to pattern collapse of the structure. Figure 4-9a shows resolved features and Figure 4-9b shows collapsed channel during rinsing as the aspect ratio of the PMMA lines increases above 10.

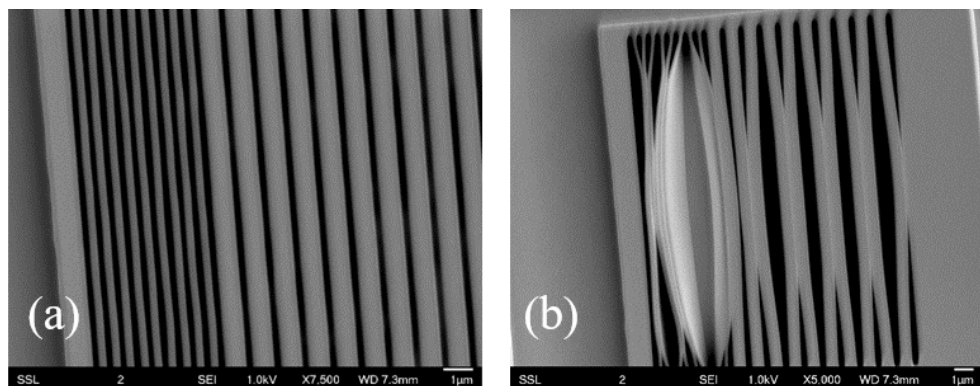


Figure 4-9. (a) 200 nm (2 pixel) channels in 2  $\mu$ m PMMA and (b) 320 nm channels (9 pixels) written using 2MeV protons written using 200 nC/mm<sup>2</sup> and 120 nC/mm<sup>2</sup> respectively (500 nm and 1  $\mu$ m pitch grating)

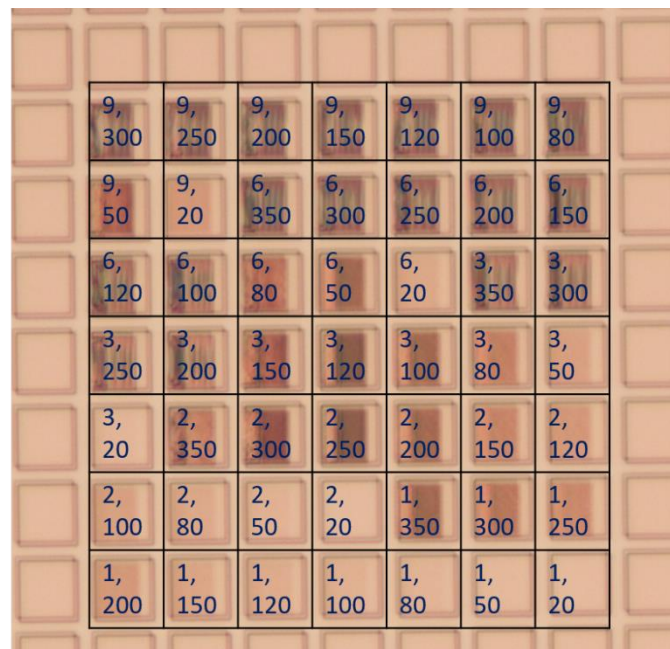


Figure 4-10. Nanograting in 2  $\mu\text{m}$  thick PMMA. Optical image of the sample after development. Channel width (pixels) and Dose ( $\text{nC}/\text{mm}^2$ ) is superimposed on the image for every region between grid bars.

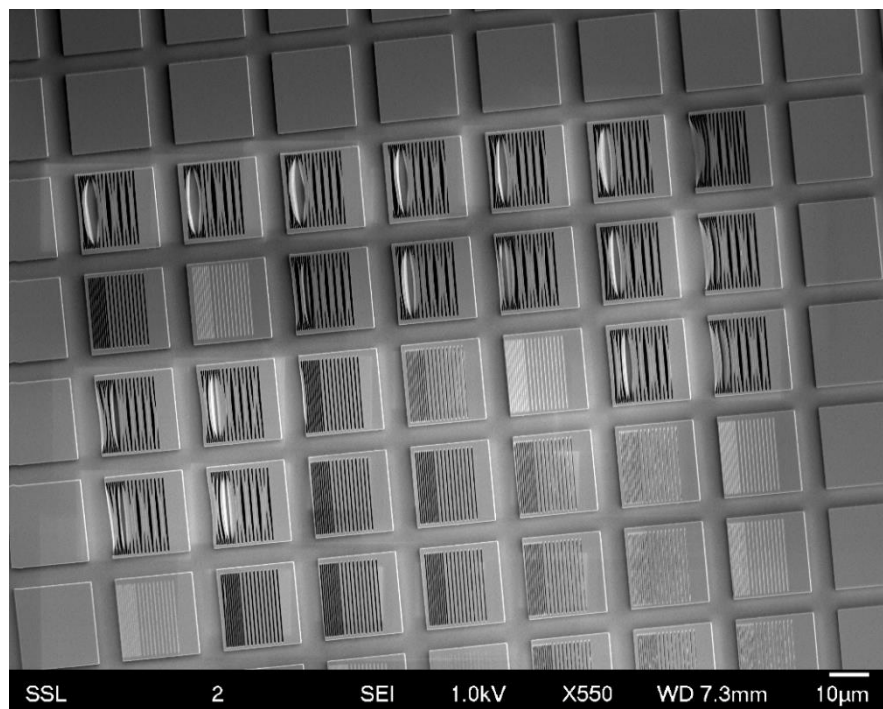


Figure 4-11. SEM image of the developed sample with the full field showing the grating areas within the grid windows

#### 4.2.4 Metal lift-off for graphene deposition

PMMA is an excellent resist for pattern transfer to metal when combined with electroplating or sputter deposition. Using acetone, PMMA can be easily stripped off, as the negative behaviour of PMMA starts off only at about 6-times the critical dose. Channels were written in PMMA using a beam of 1 MeV H<sub>2</sub><sup>+</sup> ions focused to a spot size of 140 x 318 nm. 500 nm pitch grating was written with a beam focused to 140 nm × 318 nm with a reduced brightness of 11.08 A/m<sup>2</sup>srV. Scan size was fixed at 130 × 130 μm<sup>2</sup> digitized with 4096 pixels. Single pixel lines were exposed at varying dose at a pitch of 16 pixels corresponding to 508 nm for dose varying from 60 nC/mm<sup>2</sup> to 150 nC/mm<sup>2</sup>.

After development in IPA:DI water (7:3), a layer of 10 nm Cr and 30 nm of Cu was sputter deposited at a base pressure of  $2.3 \times 10^{-5}$  torr was deposited on the PMMA layer. Subsequently, PMMA was stripped using acetone for 30 mins. These Cu lines can then be selectively used to grow graphene/graphite directly on Cu nanolines. The AFM images (Figure 4-12) were taken after the graphene deposition, in a laser assisted indirect annealing method used to deposit graphene layer. These lines are intended to study the difference of graphene work function due to selective graphene growth compared to bulk Cu. A line width of 174 nm can be seen from the extracted line scan close to beam size, written with one pixel scanned 10-times, to deposit uniform dose in the scanned area at a dose of 80 nC/mm<sup>2</sup>.

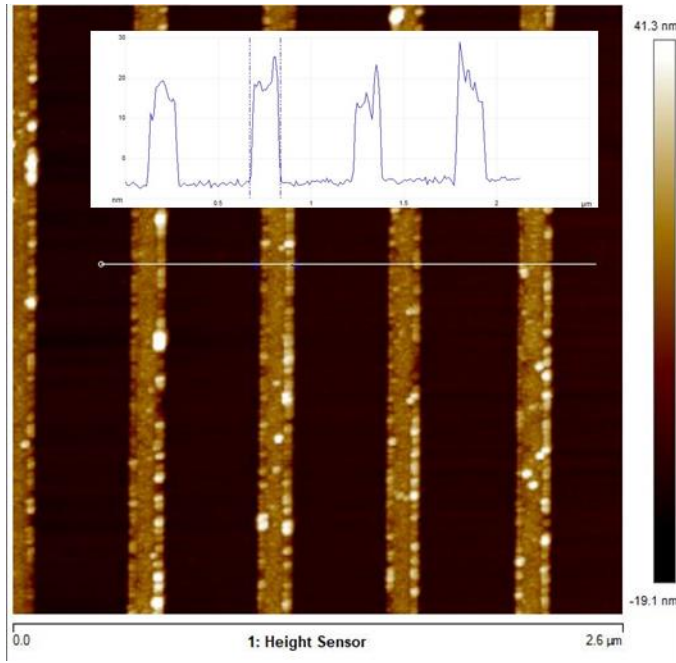


Figure 4-12. 30 nm Cu lines on Si after PMMA stripping. Inset shows the line scan of 174 nm line widths.

#### 4.3 PBW in HSQ

HSQ is a high contrast negative resist for charged particle lithography [24], [56], [57]. Feature sizes down to 19 nm levels have been fabricated using proton beam writing [155] whereas EBL and HIM have shown features down to sub-5 nm resolution. Chains in HSQ crosslink upon ion irradiation which doesn't dissolve in the developer (TMAH, 2.38%). Besides, HSQ has been routinely used to define the master pattern for nanofluidics through nano-imprinting [72]. In this section we show fabrication of nanostructures down to 30 nm using focused proton beams and discuss the pattern transfer to imprint master.

##### 4.3.1 Nano-imprinting mask fabrication

HSQ (XR1541-002, Dow corning) was spin coated at 4000 RPM for 1 min and pre-baked at 150 °C for 1 min. The thickness of the photoresist was found to be 80 nm using SEM imaging upon arrival of the photoresist. Proton beam writing was done one day after spin coating. A beam of 2 MeV protons was focused

down to  $46 \text{ nm} \times 280 \text{ nm}$  with a reduced brightness of  $6.57 \text{ A/m}^2\text{srV}$ . The object and collimator opening were kept at  $24 \times 18 \mu\text{m}^2$  and  $40 \times 40 \mu\text{m}^2$  respectively.

Both beam scan and stage scan were tested for writing features down to the beam spot resolution of 46 nm. Stage scan was used to write a 500 nm line by scanning beam in orthogonal direction, which then connects a 50 nm line.

#### 4.3.1.1 Beam scan

Beam scan was used to write two scan fields; one with tapered channel of 500 nm width at the entrance and  $25 \mu\text{m}$  long joined to a 200 nm line of  $25 \mu\text{m}$  length. A 46 nm line was intended to align and stitch in another exposure with step and repeat. Scan area of  $80 \times 80 \mu\text{m}^2$  was digitized to 4096 pixels corresponding to pixel size of 20 nm. The wider line (500 nm) at the entrance of the tapered line was written using 25 pixels and 10 pixels were used to expose for 200 nm. Single pixel line of length 3584 pixels was written corresponding to a length of  $70 \mu\text{m}$ . Dwell time was calculated based on the number of pixels occupying the total area of the exposed lines in each scan field and the dosage required. Stage was stepped in Y direction by  $80 \mu\text{m}$  to stitch to the next area. Then the cycle was repeated with stage stepped in X direction by  $3 \mu\text{m}$ . Five lines were written per dosage, per scan field. This was done to compare directly to the stage scan approach of writing a 500 nm line connecting a 50 nm line. To deposit uniform dose in the single pixel scan field, pattern was repeatedly scanned 5 times faster for the same number of times to average out the beam intensity fluctuation. Dose was varied from  $100-700 \text{ nC/mm}^2$ . Figure 4-13 shows the SEM image after development. It is noteworthy that only the dose  $> 350 \text{ nC/mm}^2$  showed the desired features with the same dimensions. The

remaining dosages had under exposed features. This anomaly is only seen with HSQ resist where batch to batch critical dose variation is observed for all the charged particle lithography.

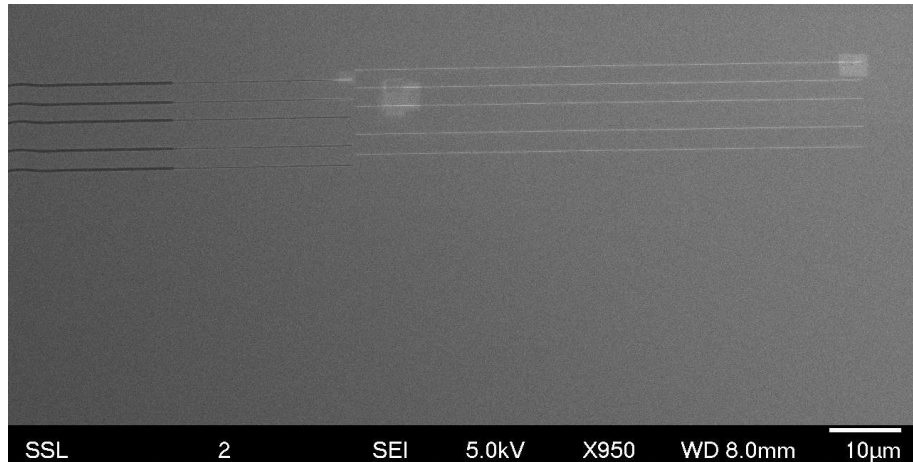


Figure 4-13. SEM image of full area written using step and repeat

Figure 4-14a shows a high resolution of the line of 44 nm measured width closely matching the beam spot measurement of 46 nm. The lines are uniform for the 70  $\mu\text{m}$  length showing the uniformity of the scan profile. However, due to a stitching error of 256 nm in Y direction and an offset of 1.4  $\mu\text{m}$  offset in X direction, it is observed that the two scans do not stitch well. This offset can be explained with an out of tune controller, which leads to an irregular stepping and positioning of the stage. The middle line is pitched 3.8  $\mu\text{m}$  instead of the intended 3  $\mu\text{m}$ . Experiments described later in this section will show results with regular stepping of the stage.

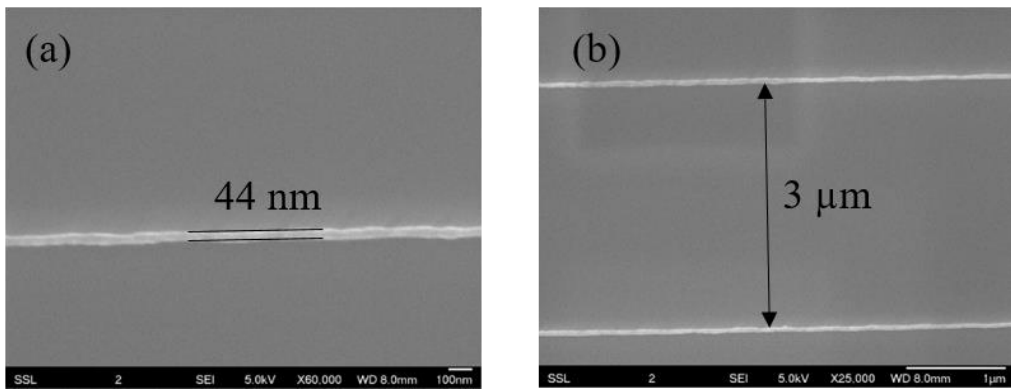


Figure 4-14. (a) 44 nm line, 70  $\mu\text{m}$  long; (b) 44 lines, 3  $\mu\text{m}$  spacing and 70  $\mu\text{m}$  long

#### 4.3.1.2 Stage scan

The stage was scanned in Y direction and beam scanned orthogonally corresponding to 500 nm for a length of 50  $\mu\text{m}$ . A subsequent line (100  $\mu\text{m}$  long) was then written with no beam scanning which corresponds to the beam spot size. The scan frequency was kept at 50 kHz with 128 pixels in X direction to get a smooth line. Dose was varied from 10 nC/mm<sup>2</sup> to 700 nC/mm<sup>2</sup>. The first dose resolving the line with no scan was observed at 400 nC/mm<sup>2</sup> with smallest line width measured to be 80 nm. Thus, stage scan for this experiment gave twice the line width compared to the beam scan result. The stage velocity to write this feature was 0.8  $\mu\text{m}/\text{s}$ . Since a single scan was used, there were gaps in the line which correlates with other photo resist experiments. Implying the stages are not optimized for scanning, but positioning. Moreover, the minimum velocity of the stage also limits the resolution possible. Figure 4-15 shows the SEM image of the written features using a scan velocity of 8  $\mu\text{m}/\text{s}$  and scan voltage of 1 V in X direction (corresponding to 500 nm) for 50  $\mu\text{m}$ , and later a 100  $\mu\text{m}$  line, written at a velocity of 0.8  $\mu\text{m}/\text{sec}$ .

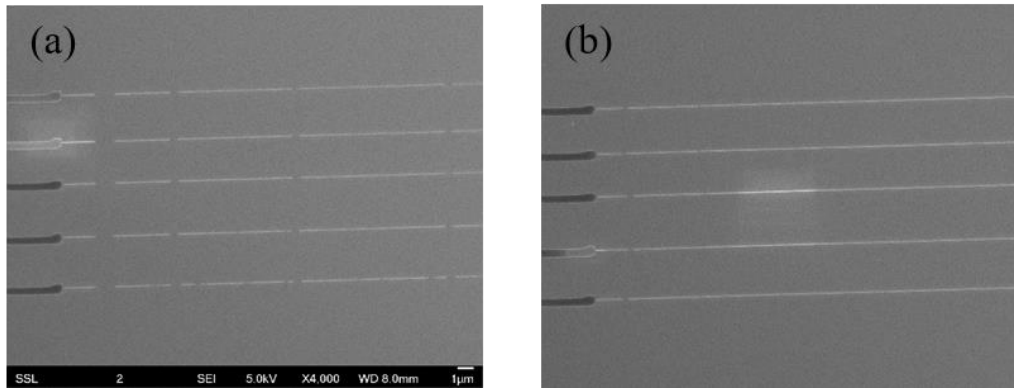


Figure 4-15. Lines written using stage scan showing the gaps left due to non-uniform stage motion

#### 4.3.2 Stamp fabrication

Resist mold with 44 nm lines fabricated using beam scan was spin coated with mr-DWL 5 at 3000 RPM for 40 s aiming at a thickness of 5  $\mu\text{m}$ . The sample was then baked at 50 °C for 2 mins followed by 70 °C for 1 min and then the temperature was raised to 90 °C for 4 mins. A micro-channel was written using a laser writer (Heidelberg,  $\mu\text{pg}$  101) to align the edges of the 44 nm lines at 5 mW power and 50% duty cycle. The sample was post baked at 50 °C for 2 mins followed by 85 °C for 6 mins. The sample was then developed in mr-Dev600 for 5 mins till the unexposed resist dissolved in the developer. Figure 4-16a shows the optical image of the sample after development.

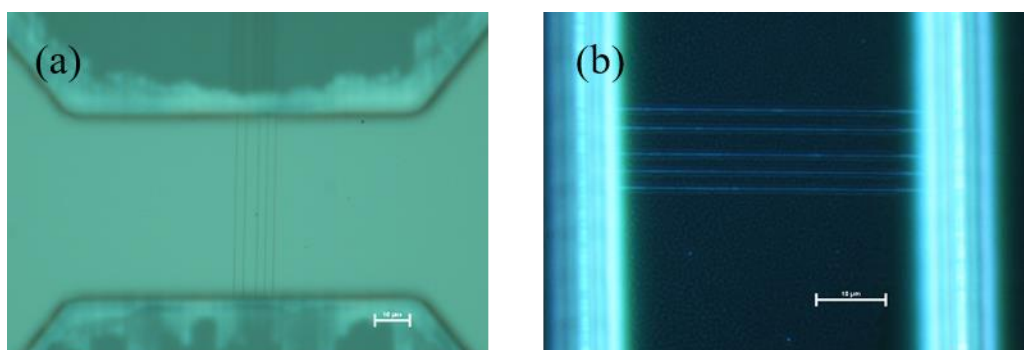


Figure 4-16. Optical image of the HSQ lines aligned with the DWL micro lines. (b) Features transferred to Ormostamp after two copies showing Ormostamp ridges

A fresh glass slide was plasma cleaned at 300 mTorr, 18 W (High) for 30 s. Plasma cleaning the glass slide improves hydrophilicity of the glass slide. OrmoPrime 08 was then spin coated at 4000 RPM for 1 min, soft baked at 150 °C for 5 mins. OrmoPrime coating improves adhesion of the subsequent ormostamp layer after crosslinking. Teflon AF 0.1% was next spin coated on the PBW resist mold at 2000 rpm for 30 s to assist in demoulding the ormostamp master copy after crosslinking. 1 drop (<0.5 ml) of Ormostamp was dropped on the Teflon coated resist mold. Using excess Ormostamp leads to bump in the stamp at the edges after covering with the plasma cleaned glass slide. Ormostamp will be sandwiched between glass slide and resist mold, covering should be done from the edges to minimize air pockets. The sandwiched stack is then exposed to UV (365 nm) for 5 mins. This crosslinks the Ormostamp and allows demoulding using a sharp knife. Figure 4-16b shows an optical image of the second-generation Ormostamp copy made from the Ormostamp master copy following the same copying process as for replicating the HSQ resist master. A 2 nm layer of carbon was sputtered for about 2 mins using Filtered Cathodic Vacuum Arc (FCVA) to protect the 2<sup>nd</sup> generation Ormostamp copy. Carbon coating prolongs the lifetime of the 2<sup>nd</sup> gen Ormostamp mold for usage in thermal imprinting of PMMA. At the same time, release of X-PDMS is aided through this layer as well. Without carbon coating, the X-PDMS usually adheres strongly to the mold.

#### 4.3.3 Linearization of single stranded DNA

Nanoimprinting master fabrication process described above was used in fabricating stamps for linearization of single stranded DNA strands. Due to confinement in the nano channels, DNA strands are stretched, paving way for

application such as gene mapping. Large arrays of nano channels can be fabricated and used as lab-on-chip devices for such applications.

Master stamps for this experiment were fabricated in HSQ using proton beam writing. Three channel cross sections were intended for the experiment:  $250 \times 250 \text{ nm}^2$ ,  $170 \times 250 \text{ nm}^2$  and  $100 \times 100 \text{ nm}^2$ . For the first two cross sections, HSQ XR1541-006 was spin coated at 4000 RPM to get 250 nm thickness after spin coating. Third cross-section was achieved in HSQ XR1541-002, spin coated at 4000 RPM for a target thickness of 100 nm.

2 MeV proton beam focused to 80 nm using a 500 nm thick Ni resolution standard with under plating of 1  $\mu\text{m}$  was used. Stage scan in Y was used to write channels of the required dimensions in the three samples at varying dosage (100-400 nC/mm<sup>2</sup>). Lines were pitched at 5  $\mu\text{m}$  and written with dimensions of 250 nm, 170 nm, and 100 nm for the respective samples. Beam was scanned orthogonally to the stage movement at a pixel resolution of 40 nm. Samples were developed in 2.38 % TMAH without surfactant for 1 min. Stamps were made later using the process described in section 4.3.1.

The Ormostamp copy masters with 250 nm and 170 nm channels were coated with a 2 nm layer of carbon using FCVA before transferring the patterns on to PMMA. For the 100 nm channels, PDMS-X was used as a master. Figure 4-17 shows the SEM image of the line array indicating the uniformity of the fabricated lines. Features with these dimensions are routinely fabricated with reproducible linewidths. Figure 4-17 shows the extension of a single DNA strand shown with the Lab-on-Chip devices made using PBW. As the dimension of the channel decreases, extension of the DNA strand increases.

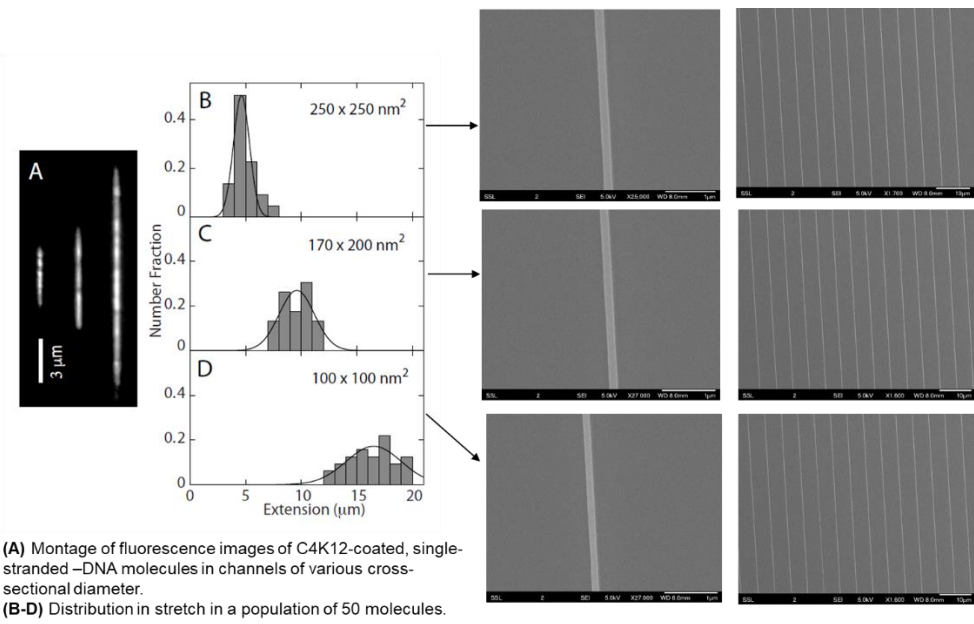


Figure 4-17. Linewidths of 250 nm, 170 nm and 100 nm in HSQ shown in high resolution SEM images and full area features used for the experiment on the left

#### 4.3.4 Pillar fabrication in 100 nm thick HSQ

Using automated alignment and focusing, shown in chapter 2, a beam of 2 MeV H<sub>2</sub><sup>+</sup> ions was focused down to 23 × 32 nm<sup>2</sup>. This beam was used to write single pixel width lines and pillars. Resolution of HSQ is dependent on the adhesion of the substrate with the photo-resist. Gorelick *et. al.* [156] reported use of Ti layer on Si to improve adhesion on the sample. Following this method, we deposited ~3 nm thick layer of Ti using FCVA deposition, with no bias applied to the sample, for a duration of 3 minutes. A 100 nm thick layer of HSQ XR1541-002 was spin coated on the sample at 4000 RPM, followed by a pre-exposure bake at 95 °C. Proton beam exposure was carried out the next day.

Two features were written on the same sample using beam scan. Scan size was kept at 5 × 5 μm<sup>2</sup> with 256-pixel resolution. Each pillar was kept for one-pixel irradiation with exposure carried out at 50 multiple passes to allow even dose

deposition. A 20-pixel pitch was chosen in both X and Y directions that corresponds to  $390 \times 390 \text{ nm}^2$  array of 100 pillars. Dose was deposited by counting ions per pillars to get the sensitivity of the resist layer. Dose ranging from 100 protons/pillar to 6500 protons/pillar at a count rate of 46,000 protons/s as measured using STIM. The total time for exposure was 5.26 minutes. After exposing each beam field, stage was stepped 20  $\mu\text{m}$  in X. The sample was later developed in 2.38 % TMAH without surfactant for 1 min. Figure 4-18a shows the SEM image of the pillars written using 2000 protons/pillar equivalent of 434 nC/mm<sup>2</sup> dose. FWHM of the pillars are quantized from ImageJ analysis. Figure 4-18b shows the pillars fabricated using the highest dose of 6500 protons/pillar equivalent of 1413 nC/mm<sup>2</sup>. The smallest feature written is 25 nm  $\times$  65 nm using a beam focusing of 23  $\times$  32 nm<sup>2</sup>. The smallest feature in X direction matches the measured beam width. However, resolved feature width in Y direction is twice the measured beam Y-FWHM. This can be explained based on the scattering from the collimator slits in Y direction. For this focusing, an opening of  $8 \times 3 \mu\text{m}^2$  in object slits and  $20 \times 10 \mu\text{m}^2$  in collimators was selected. The smaller collimator opening in Y direction results in a halo around the focused spot due to larger scattering from the edges of the slits. Upon higher dose irradiation, the area under the scattered halo reaches the critical dose needed for exposure, thereby leading to wider feature sizes. It should be noted that the critical dose required for writing pillars is higher than writing line features in HSQ or any resist, since there are no overlapping spots during beam scanning. This leads to accurate analysis of the sensitivity of the photo resist. Figure 4-19 plots the FWHM of the developed features measured using ImageJ as a function of ion dosage. At higher dose, the pillar dimension saturates to 50

nm in X direction and 80 nm in Y direction. The aspect ratio of the pillar ranges from 2-4. This graph can be used as a quantification of the resist sensitivity when plotted with a normalised FWHM, with respect to the estimated beam FWHM. A slight tilt in the pillar images can be seen with respect to the beam scan direction as evident from the SEM images of the pillars (Figure 4-18). This tilt is attributed to a slight rotational mis-alignment of the second quadrupole lens which rotates the beam profile. This effect can be seen with patterns written with non-overlapping pixels for scanning, such as pillars.

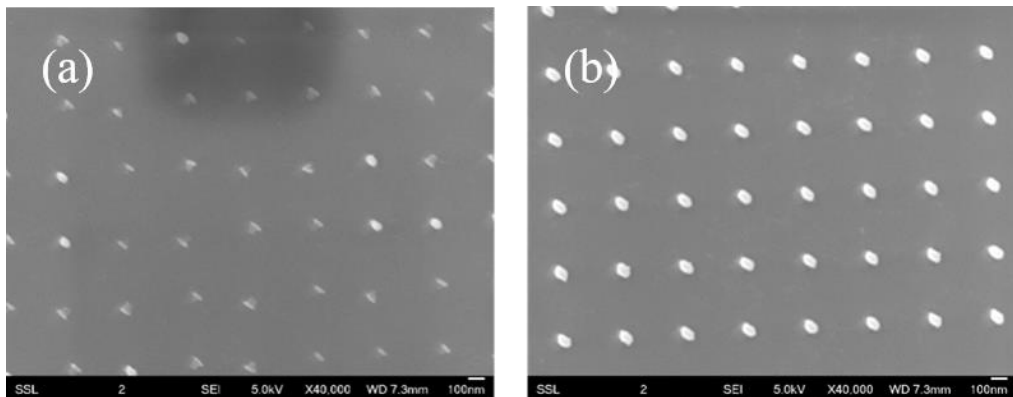


Figure 4-18. 30 nm pillars (a), 50 nm pillars (b)

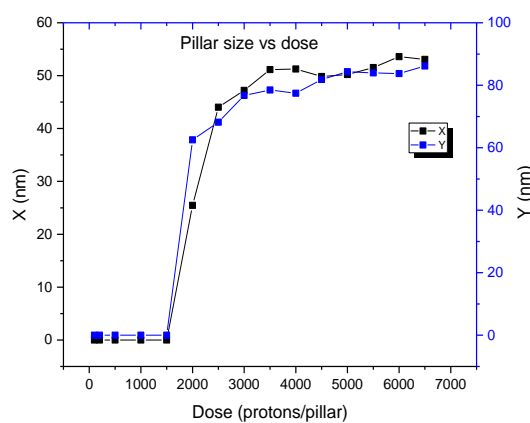


Figure 4-19. Pillar size vs Dose written using beam of 2 MeV H<sub>2</sub><sup>+</sup> focused to 23 nm × 32 nm

#### 4.3.5 Line fabrication in 100 nm thick HSQ

Using the same beam and the same sample, single pixel lines were also written to test the line width resolution. With a scan size of  $5 \times 5 \mu\text{m}^2$  and pixel digitization of 1024 (4.88 nm/pixel), 5  $\mu\text{m}$  long lines in Y direction were written with a pitch of 204 pixels corresponding to a pitch of 996 nm. 5 lines were written using beam scan and stage was stepped for the next scan field in X direction by 20  $\mu\text{m}$ . Dose was varied from 5 nC/mm<sup>2</sup> to 390 nC/mm<sup>2</sup> in steps of 5 nC/mm<sup>2</sup>. The scanning per field was repeated 10 times at 10x larger dwell time per pixel to deposit uniform dose. The dwell time ranged from 9  $\mu\text{s}$  to 69  $\mu\text{s}$  per pixel. The writing took a total of 26.2 minutes. SEM images in Figure 4-20 show the developed features for two different doses. The image on the left shows lines written with a dose of 385 nC/mm<sup>2</sup> with a feature FWHM of 52 nm. On the other hand, image on the right shows a dislocated line width of 30 nm written with a critical dose of 320 nC/mm<sup>2</sup>. This critical dose for writing a line is a factor of 1.35 times of the dose required to write pillars on the sample. Figure 4-21 plots the normalised linewidth (FWHM) as a function of log dose. Just as in the case of pillars, line width saturates at higher dosage and this plot can be used as a direct resolution performance of the photoresist. However, the smallest linewidth 30 nm does not adhere to the sample completely. This can be explained based on the surface tension acting on the line that remains standing which is rocked by the developer. In the case of the pillars, they can sustain the rocking to a greater extent allowing features down to 25 nm to be measured. The feature width which are slightly wavy start appearing at a dose of 350 nC/mm<sup>2</sup> when the feature width is 52 nm. Due to slight rotational mis-alignment

when overlapping pixels are used in writing patterns such as lines overlapping tilt leads to a wider linewidth for lines after development.

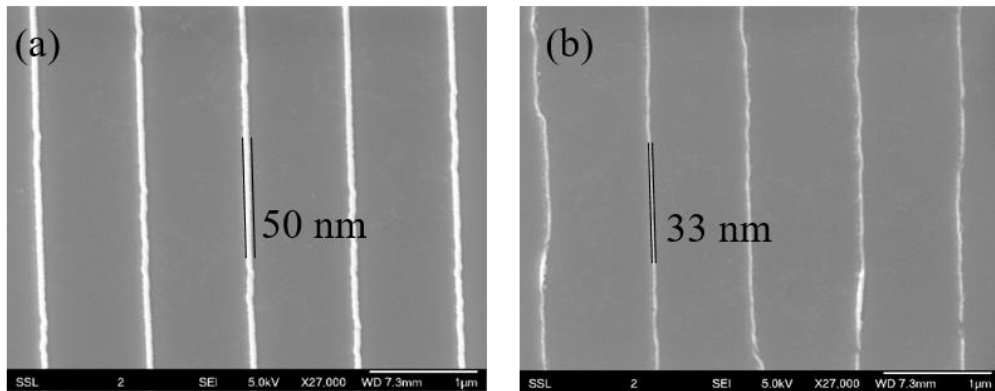


Figure 4-20. 50 nm lines (left) and 33 nm lines (right) using the same beam as pillars

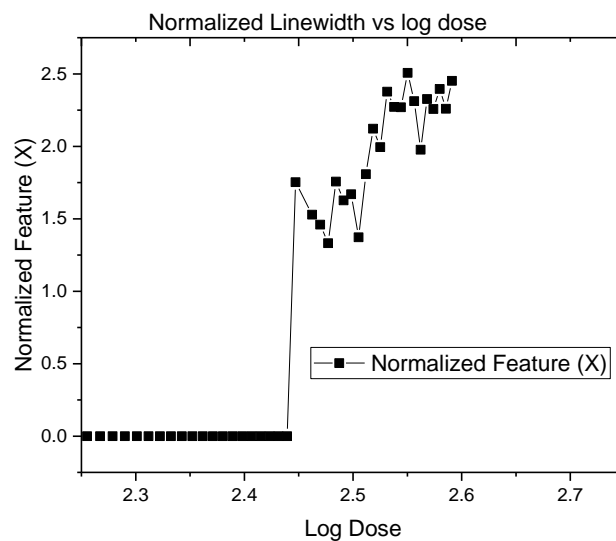


Figure 4-21 Line width vs log dose

#### 4.3.6 Pillars written with focused 1 MeV He<sup>+</sup>

A faster approach to write pillars, is to avoid blanking the beam, but scan with a pixel resolution larger than the beam spot size. A 1 MeV alpha beam focused to  $52 \text{ nm} \times 254 \text{ nm}$  at a reduced brightness of  $5.86 \text{ A/m}^2\text{srV}$  was used to write pillars in 200 nm thick HSQ. Scan size was kept at  $100 \times 100 \mu\text{m}^2$  with a pixel

resolution of 128. This corresponds to a scan resolution of 781 nm. A BMP file was written with  $128 \times 128$  pixels, with all pixels to be exposed. This method writes 16,384 pixels ( $128 \times 128$ ) which is two order lesser pixels to write (228 times lower, to be precise) than a file written with a pixel size same as the beam size. Dose range was varied from 100 alpha particles per pixel to 6500 alpha per pixel same as the proton exposure earlier. The critical dose, as seen from the image (Figure 4-22), demonstrates that the sensitivity for alpha in HSQ is 8.18 times higher than with protons. This matches with the sensitivity ratio of 7.94 expected from the ratio of electronic stopping from SRIM for 1 MeV proton in HSQ (25.43 keV/ $\mu\text{m}$ ) and 1 MeV alpha in HSQ (201.9 keV/ $\mu\text{m}$ ).

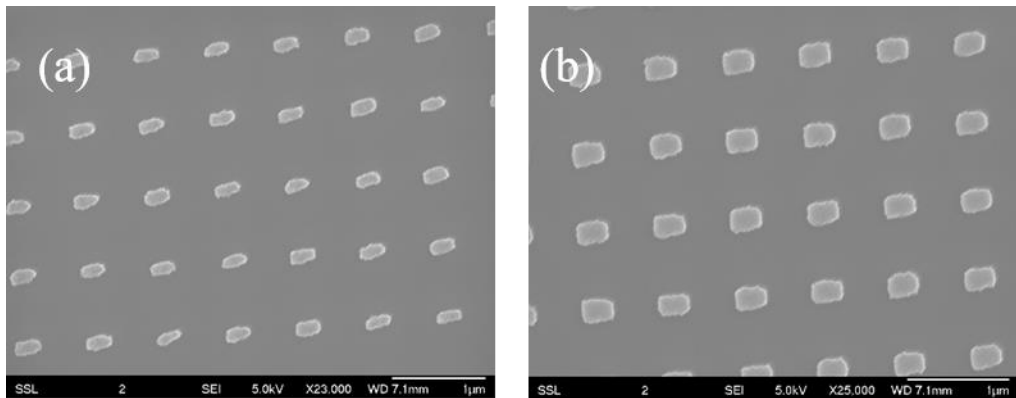


Figure 4-22. Pillars written using 1 MeV Alpha in HSQ. (a)  $100 \times 200 \text{ nm}^2$  pillars written at  $1000 \text{ He}^+/\text{pillar}$  ( $\sim 53 \text{ nC/mm}^2$ ). (b)  $200 \times 200 \text{ nm}^2$  pillars written using 6500 alpha/pillar ( $\sim 346 \text{ nC/mm}^2$ )

The pattern in the previous alpha beam experiment was repeated with reduced scan size. The pitch was reduced to 300 nm with a beam of  $58 \times 207 \text{ nm}^2$ . The same exposure dose range was employed. In this case we observed an overlapping of the pixels in Y direction. Figure 4-23 shows a resulting nano grating from spot irradiation with focused helium beam of 1 MeV energy at a dose of 5000 ions/pixel. This overlap is determined based on the sensitivity of HSQ for alpha exposure and increased scattering of helium from the beam

defining slits. The damage induced on these WC slits by helium is more than protons, and thus the scattering from the slits edges increases.

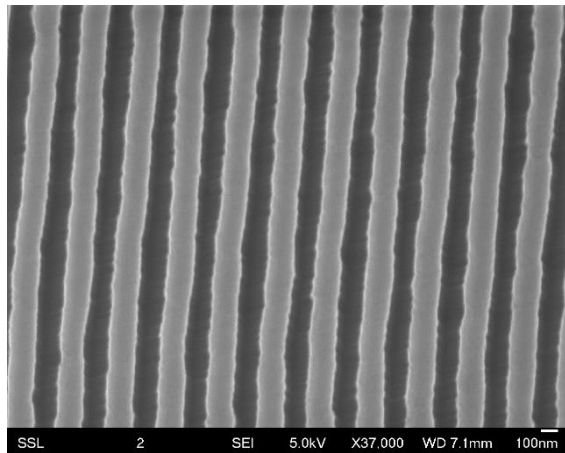


Figure 4-23. 200 nm lines and 100 nm spacing written by overlapping spot irradiation in Y direction at a dose of 5000 ions/pillar

#### 4.4 PBW in non-resist based substrates

In the previous section, PBW down to 30 nm was demonstrated in resist based substrate. Here we discuss writing in Silicon for fabrication of high aspect ratio channels, and Strontium Titanium Oxide (STO) for fabrication of waveguides with low transmission loss.

##### 4.4.1 Silicon

Using MeV proton beam focused to nanometre dimensions and a subsequent electrochemical etching, high aspect ratio channels can be fabricated in Si [157].

A beam of 2 MeV  $\text{H}_2^+$  was focused down to 50 nm by 200 nm with object and collimator apertures sizes of  $16 \times 12 \mu\text{m}^2$  and  $20 \times 20 \mu\text{m}^2$  respectively at a reduced brightness of  $7.58 \text{ A/m}^2\text{srV}$ . Ni resolution standard image (Figure 4-24) shows a focusing of  $17 \text{ nm} \times 102 \text{ nm}$  with the object sizes closed to  $8 \times 6 \mu\text{m}^2$  and  $10 \times 10 \mu\text{m}^2$  (reduced brightness of  $7.46 \text{ A/m}^2\text{srV}$ ).

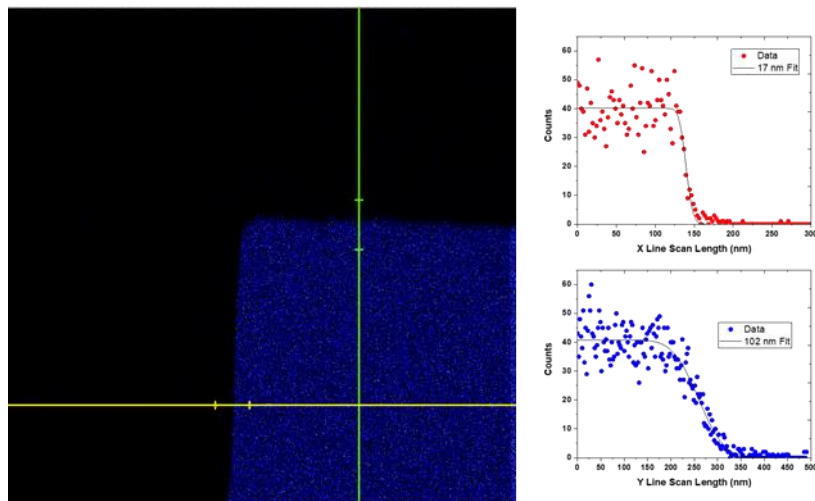


Figure 4-24. On-axis STIM Image of Ni resolution standard. Also shown are the line scans extracted from the image showing a focus of  $17 \times 102$   $\text{nm}^2$

As the collimator size was increased, the beam size increases. Larger object and collimator sizes (12 and 20  $\mu\text{m}$  respectively) in Y direction were used to accommodate high fluence exposure in reasonable time. Scan size was kept at  $10 \times 10 \mu\text{m}^2$  with  $1024 \times 1024$  pixel resolution. 10 sets of lines were written with three dose values ranging from  $10^{16}$  protons/ $\text{cm}^2$ ,  $2 \times 10^{16}$  protons/ $\text{cm}^2$  and  $3 \times 10^{16}$  protons/ $\text{cm}^2$  at a count rate of 130,000 protons/s. The line was defined as a single pixel scan file using EPL format, with scanning repeated 10 times. Stage was stepped 10  $\mu\text{m}$  following every exposed field. The etching process is described by Breese *et. al.* [157]. SEM Image (Figure 4-25) shows the surface and cross section of the fabricated 100 nm etched channel to a depth of 5-8  $\mu\text{m}$ . This corresponds to an aspect ratio of 50-80.

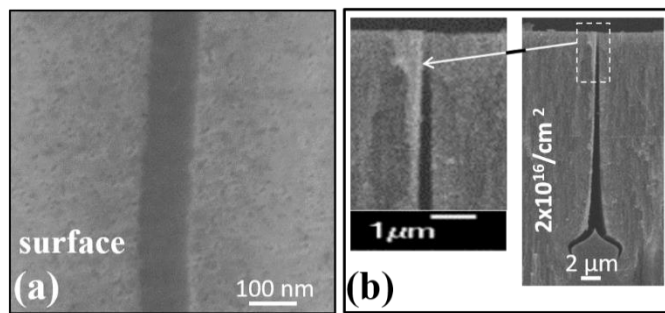


Figure 4-25. 100 nm channel etched in Si. (a) plan view SEM of a 100 nm wide channel with a 1 MeV proton fluence of  $2 \times 10^{16}/\text{cm}^2$ . (b) Cross-section SEMs of similar channel as in (a), showing (right) the full anodized depth beyond the end-of-range at 15  $\mu\text{m}$  and (left) the top 5  $\mu\text{m}$  where a channel width of 150 nm is produced

#### 4.4.2 STO

Direct writing using protons lead to waveguide fabrication in oxides. A 1.5  $\mu\text{m}$  strontium titanium oxide (STO) layer was grown on  $\text{YAlO}_3$  using pulsed laser deposition in oxygen environment at 760  $^\circ\text{C}$  at T-Lab, NUS. A 500 keV  $\text{H}_2^+$  beam was used to write waveguides in the sample. The waveguide is formed in the region between two exposed lines. Three different pitches with four different fluences were tried to calibrate the dose needed for waveguide fabrication. The pitches tried were 2.5  $\mu\text{m}$ , 5  $\mu\text{m}$  and 7  $\mu\text{m}$  and the four fluence used were  $5 \times 10^{15}$ ,  $1 \times 10^{16}$ ,  $5 \times 10^{16}$  and  $1 \times 10^{17}$  protons/ $\text{cm}^2$ . The stage was scanned more than the length of the sample (5.5 mm) and beam was scanned in orthogonal direction to fix the size of the exposed region to 4  $\mu\text{m}$ . SEM image (Figure 4-26) shows the exposed lines with the fluence shown in increasing order from left to right. To avoid gaps in the stage scan as mentioned earlier, stage was scanned twice over each line with twice the speed. The corresponding stage velocity varied from 53  $\mu\text{m/s}$  for the lowest fluence to 2.7  $\mu\text{m/s}$  for the highest fluence. Figure 4-27 shows the line scan extracted from the image below for a fluence of  $5 \times 10^{16}$ . Matching pitches and scan sizes can be seen from the graph.

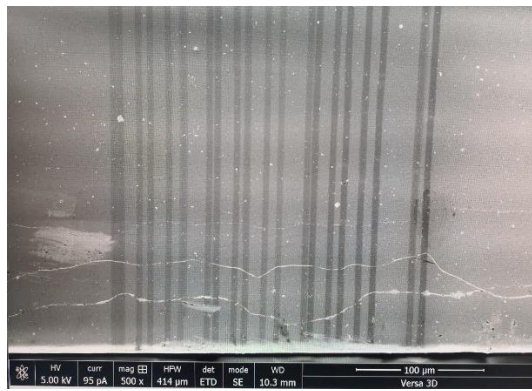


Figure 4-26. SEM image of the waveguides in STO

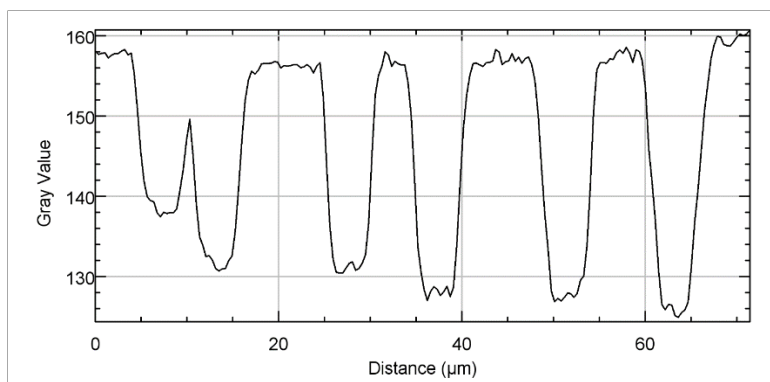


Figure 4-27. Line width and pitch matching the target stage motion

#### 4.5 Summary

Nanograting fabrication in PMMA with 200 nm lines and 300 nm spacing over scan size of 100  $\mu\text{m}$  was demonstrated. Fabrication of 30 nm channels in 2  $\mu\text{m}$  thick PMMA with an aspect ratio of 67 was shown. This is the smallest feature size written in PMMA. Replication of 30 nm channels to Ni lines was demonstrated using electroplating. Nano-grating fabrication of 200 nm channels (aspect ratio 10) was shown in 2  $\mu\text{m}$  thick PMMA at pitches of 500 nm and 1  $\mu\text{m}$ . Using metal lift-off on 400 nm thick PMMA, we showed fabrication of 174 nm wide Cu lines of 30 nm thickness and a Cr base of 10 nm. In HSQ, we demonstrated fabrication of 30 nm pillars, and 50 nm lines. A nano-imprint mold with 42 nm lines was fabricated in HSQ and copied twice in Ormostamp

for nanofluidics. High aspect ratio channels with dimensions of 100 nm were fabricated in Si using PBW and electrochemical etching. 5 mm long waveguides were fabricated in STO at varying pitches using stage scan.

## 5 Simulation of Masked Ion Lithography

### 5.1 Introduction

High throughput batch fabrication using focused proton beam is limited by the brightness of ion sources currently employed. Three major characteristics need to be optimised for reproducible fabrication of structures which require longer exposure timings. First, lower thermal instability of the lenses, typically magnetic, used for focusing protons. This ensures minimal variation in the beam spot size over time thereby allowing minimum achievable critical dimension. Second, lower current density fluctuation to prevent uneven dose distribution in the writing field leading to line width variation. Last, lower accelerator terminal voltage fluctuation to achieve smaller chromatic aberration, and therefore, the smallest possible spot size while focusing a beam of protons.

To speed up fabrication of nanostructures, a stencil mask with critical features defined by a focused proton beam can be used for faster replication of nano-structures. The beam characteristics described above can be relaxed in lieu of a stencil mask which blocks the protons in the mask and, offers wider process latitude for photo-resists and yield enhancement. Such a stencil mask would feature smooth side wall slope with the thickness defined by the energy of protons to be blocked. Features are defined as the transmission opening for protons to reach the sample in the back plane. An ideal stencil would stop all the protons going through the mask allowing transmission only through the defined openings. However, grazing angle scattering or near edge scattering broadens the post transmission spatial ion distribution thereby increasing the feature size on the sample placed behind the mask.

Stencil mask fabrication and nano-replication can be applied for various techniques, be it for photoresist or resistless. In the former case, a broad beam of proton can be blocked in the mask and edge scattered; and the divergence-limited structures can be replicated in photoresist. In the latter case, a stencil mask is used as a physical blockade for applications involving metal deposition or reactive ion etching. The feature sizes by this method are limited by the penumbra broadening/shadowing of the deposited material/etchant.

Earliest application of masked ion exposure was demonstrated in continuously varying threshold voltage in metal oxide semiconductor (MOS) architecture was attained by masked doping of the MOS active region. This was done by employing molybdenum masks which moved with a speed corresponding to the dosage required to achieve a continuously varying charge concentration under the mask region [158]. Advantages of such a technique is understood by the faster processing, and immunity to current fluctuation during implantation. Besides, the method doesn't require a focused beam, thereby allowing a wider region of exposure. Applications of the method include voltage variable resistor, capacitor, remote cut-off field effect transistors (FET) and clock-less ADC. In addition, a computer controlled doping to achieve lateral doping, showed that the brightness limitation can be overcome by careful writing schemes with a focused beam [159].

Pattern transfer using resist stencils was shown by Selinger et. al. [160]. A focused beam of gallium ions was used to machine line widths of 40 nm in PMMA resist which were later transferred into Au by RF – sputter deposition. On the other hand, patterns were etched into a Au coated Al<sub>2</sub>O<sub>3</sub> membrane,

which was later used as a stencil for pattern transfer to PMMA. A beam of 150 kV protons was used to expose and replicate high aspect ratio structures in PMMA using the transmission mask to stop a beam of collimated protons. Structures as small as 500 nm were replicated using the technique with challenges being listed as wafer scale uniformity and mask fabrication, and competency with respect to focused ion and electron beam lithography for the semiconductor industry.

As early as 1985, nano-patterning using masks to write features as low as 30 nm has been demonstrated by Adesida et. al. [161]. Linewidths of 30 nm were transferred to Si<sub>3</sub>N<sub>4</sub> after EBL patterning in resist and subsequent reactive ion etching. A layer of Au and Pd was coated to limit the range of transmitting ions through the stencil. Pattern replication in PMMA was demonstrated for the linewidths of 30 and 80 nm using a beam of 35 keV protons. Besides the resolution of the masked lithography, the study also showed an order of magnitude higher sensitivity of PMMA for protons than EBL. Furthermore, fabrication of masks with linewidths of 150 nm and 400 nm was replicated in PMMA using a beam of 120 keV protons demonstrating the reliability of the technique and its applicability towards fabrication GaAs FET.

An important advantage of masked ion beam lithography (MIBL) can be understood from the linewidth variation in developed lines. Randall *et al.* [162] showed the line width variation with MIBL, and compared it to optical lithography. Besides a wider process latitude, they also showed a dose region for positive and negative behaviour.

Pang *et. al.* [163] showed structures down to 150 nm, replicated in PMMA using MIBL, followed by subsequent dry etching using the same mask for making GaAs MESFETs.

Building on the resolution shown by direct MIBL with 1:1 mask to substrate replication, an ion projection lithography (IPL) system was developed [164]. The system reduced the stringent requirement of high aspect ratio sub 100 nm mask features by introducing focusing lenses between the mask and the substrate. A beam scanner scans over the substrate which is then stepped to achieve wafer scale fabrication. Features down to 100 nm were fabricated using 73 keV helium ion directly on silicon dioxide using chemical etching. A major advantage of this technique is the high depth of focus that is achieved by the mask absorption of the ion beam.

Scattering issues from the mask edges can be resolved by increasing the thickness of the mask, thereby stopping the incident ions within the mask and reabsorbing the scattered ions from the mask edges. This technique leads to an increase in the structure density [165]. Besides increasing the thickness, energy of the incident ion and species can be varied based on the application and resist thickness. With controlled beam divergence, depth of focus for MIBL can be increased to 1 mm. fabrication of sub 100 nm features in photoresist was demonstrated with a silicon stencil fabricated by EBL and subsequent etching. High aspect ratio silicon openings in the stencil were reproduced up to a sample to mask distance of 1 mm [166].

Apart from the dedicated applications discussed above, MIBL makes resist characterization simple. AZ deep UV resists were characterized using EBL and

MIBL, wherein the silicon membrane was fabricated using EBL and etching. Slit of 150 nm was reproduced in the resist at sample to mask distance of 1 mm [167].

Fast writing times and development in fabrication of stencil led to an ion projection lithography system [66] which uses focusing lenses to expose samples at wafer scales by de-magnifying the stencil mask. Demagnification in the range of 3 to 10 were employed with mask features down to 150 nm attained with minimum line width of 70 nm, achieved using the system.

MIBL used in conjunction with highly charged ions can result in a very surface specific lithography with microscopic details.  $Xe^{40+}$  ions loses energy through potential interaction with the sample electrons thereby increasing the sensitivity for resists such as PMMA [168].

Stencil masks can also be used directly for device fabrication. Depositing metal through nano stencil could be a way to replicate nanostructure on sensitive substrates with poor or no adhesion to photoresist, or higher sensitivity to ion exposure. Features as small as 15 nm have been reproduced using metal evaporation through nano stencils [169].

Extensive study was performed to understand key challenges in mask fabrication for MIBL using IPL. Three important aspects / process control are critical dimension, image placement and defect density [170]. Ion implantation typically uses photoresist mask to stop the incident ions. However, this leads to an increase in the number of steps for a process. Replacing the resist coating, exposure and stripping steps by a stencil mask made of a silicon membrane, reduces the complexity of the process [171].

IPL made improvement in the critical dimension down to 50 nm achievable by employing high contrast resists [67]. With a demagnification of 4 and overlaying masks, a DRAM fabrication layout was also demonstrated.

Effect of shot noise, and its correlation with the line edge roughness (LER) and width roughness, was studied on chemically amplified resists. The study concluded that the LER beyond a certain dose threshold is independent of the shot noise, but dependent on the resist properties, development method and post-bake temperatures [172].

Nano replication using apertures in AFM cantilevers were demonstrated by Jamieson *et al.* [173] using a 1.5 MeV He beam. The study concluded that the dimension of the nano aperture defines the ultimate feature size replicated in the resist. On the other hand, beam to mask misalignment leads to a broadening of the feature size due to exposure from scattered ions. It is important to note that fabrication of the nano apertures was performed using FIB, which resulted in conical shaped apertures. In this regard, PBW has the advantage of fabricating high aspect ratio structures with vertical sidewall.

Stencils can also be used for etching the substrate materials with sub micrometre precision [174]. Fabrication of low stress silicon nitride membrane, coated with a protective layer of aluminium, when placed directly on top of a substrate acts as a mask for substrate etching. Features down to 200 nm were etched using this technique. However, challenges of this technique include - minimum feature size to withstand the stress in the SiN layer, mask to substrate gap and mask heating or alignment of the mask plane with respect to the sample plane.

## 5.2 Simulation of masked ion irradiation

Range of ions is well known based on the experimental data and analytical derivations. Simulation programs such as SRIM [141] and Geant4 [175], [176] are used here to simulate the masked ion beam lithography in PMMA using the stencil mask fabricated above. SRIM is used to predict the range of ions in various materials and end of the range straggling. However, SRIM can only be used for continuous geometries for the material. Complex geometries such as apertures cannot be simulated using SRIM. Geant4 has been developed to study the effect of ion interaction with materials with vast libraries and physics interaction models. Customized geometries can be defined and simulated for real beams.

Simulations of aperture ion lithography using movable apertures was done by Gorelick *et. al.* [128] and Alves *et. al.* [177], who simulated the performance of edge scattering from 60 nm apertures fabricated in Si stencils by using FIB to define aperture of 90 nm and reduce the aperture size to 60 nm by sputtering Au/Pd. We extend the study of edge scattering from apertures and lines written using proton beam writing in resist.

### 5.2.1 Geant4 simulation setup

Geant4 version 10.03 has been used for the simulations [175], [176]. Multiple scattering and ionization has been modelled using Mendenhall's correction [178] with binary collisions. Main elements of Geant4 are the user processes, geometry of the detector/sample and the physics processes used. User process handles each collision as an event and follows the ion till the defined level of energy required to be transferred is reached. This cut off is set as a distance

rather than energy, since minimum energy transferrable depends on the type of incident ion, material and physics processes used. Whereas, specifying a cut off length, will track and generate secondaries only when the secondary can travel at least the specified cut off length after collision. In our simulations we kept this cut off length to be 1 nm which is approximately the range of secondary electrons in materials with keV ion collision. This range is verified from CASINO simulation [179] for electrons with energy of 100 eV which is the maximum energy transferred to an electron from a beam alpha particle accelerated to 200 keV.

The tracking of ion and secondaries in the material is determined based on the step length given at the beginning of the simulation. This step length determines the position of the ions and tracks the number of collisions and energy loss the ion encounters within each step length. We used a maximum step length of 1 nm which is 1/500 times the range of 200 keV Helium ions in Ni used for masked irradiation.

#### 5.2.1.1 Geometry

We defined our geometry to be apertures of 60 nm, 250 nm, and 400 nm widths having a thickness of 1  $\mu\text{m}$ . We also took into account the 60 nm lines resulting from the poor adhesion. Besides we used the model to study lines and spaces down to 10 nm as a test for resolution with the masked ion irradiation for nano replication. Each geometry places a Ni foil (or slab) of thickness 1  $\mu\text{m}$  and size in orthogonal direction varying from  $500 \times 500 \text{ nm}^2$  to  $2 \times 2 \mu\text{m}^2$  based on the aperture width studied to increase the statistics of the ion collection and reduce the computation time. We keep the fluence a metric to determine the number of

ions to be simulated. A PMMA block is also defined with thickness of 400 nm kept after the Ni aperture with varying gap between the mask and sample to simulate real exposure scenarios. Figure 5-1 shows a geometry with Ni foil shown in red with a 60 nm aperture, PMMA layer placed right under the mask shown in green. Also shown are the 200 keV alpha particles normally incident on the Ni mask (in blue) with the scattering ions and secondaries generated shown in yellow. It can be observed that mask irradiation lets ion through multiple paths. Main regions are highlighted in the schematic below.

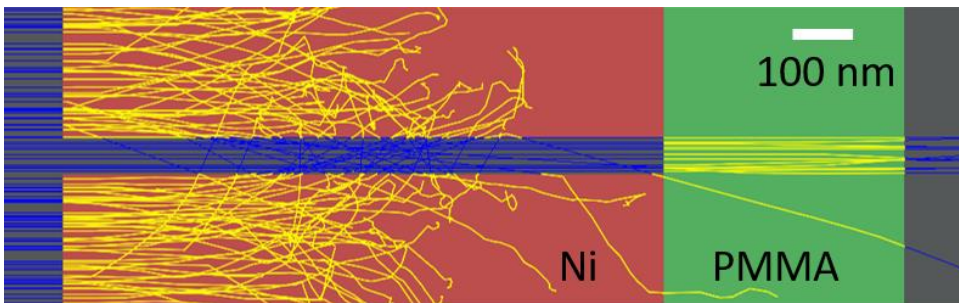


Figure 5-1. Mask and Sample geometry defined in Geant4. Also shown are 200 keV alpha ions incident on the mask plane from left. Scattering of the ions can be observed through the mask and further transmission through 400 nm thick PMMA layer kept right after Ni

#### 5.2.1.2 Beam definition

Realistic beams can be defined in Geant4 using General Particle Source which allows simulation of divergent beams, and different shapes of the beam. In our simulation we used General Particle source with divergences up to 100 mrad. Besides controlling the position of the beam centre and beam axis alignment, this method allows a simulation of tilting a divergent beam and testing the impact on the resolution of pattern transfer in photo resist.

### 5.2.1.3 Tracking and process

Beam incident particles exiting the mask and entering the PMMA layer were tracked. Position and energy of these particles were recorded in an ascii format. This file was then later analysed using a LabVIEW written imager where a 2 D image was generated from the array in ascii for the energy and particle intensity. Two plots can thus be analysed for the energy spread and the beam spread marking the resolution of the feature in the mask. The energy spectrum of the ions entering the PMMA layer after passing through the mask layer are also plotted from the collected data.

### 5.2.2 Range of ions in Ni

Range of alpha particles in Ni (density 8.9 g/cm<sup>3</sup>) is plotted as a function of energy in Figure 5-2. The range for GEANT4 and SRIM are compared. Geant4 model range differs from SRIM for energies lower than 40 keV. The difference in projected range is less than 5 % for energies above 40 keV.

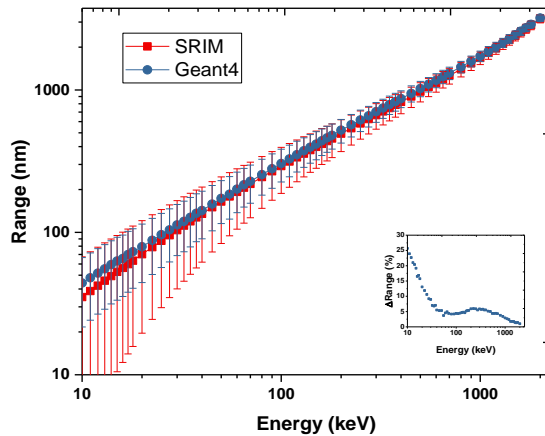


Figure 5-2. Projected range comparison from SRIM and Geant4 in Ni for helium in the energy range of 10 keV to 2000 keV

Masked irradiation using the Ni stencil was done at the broad beam exposure facility beam line ( $45^\circ$ ) using 200 keV alpha particles. The end of the range of alpha particle was compared between SRIM and Geant4, and it was found that they are both agreeable to within 5% with Geant4 predicting a bit longer range in Ni for alpha than SRIM. This could be due to different algorithms the two calculations work. SRIM considers the universal curve for energy loss and Geant4 works on the continuous slowing down approximation using Lewis' method [180]. The energy and the particle were chosen such that the ions end up approximately half way through the 1  $\mu\text{m}$  thick Ni stencil. Figure 5-3 shows a comparison of 10,000 alpha particles in a block of  $1 \mu\text{m} \times 1\text{um} \times 1 \mu\text{m}$  Ni. Also shown is the energy loss vs target depth.

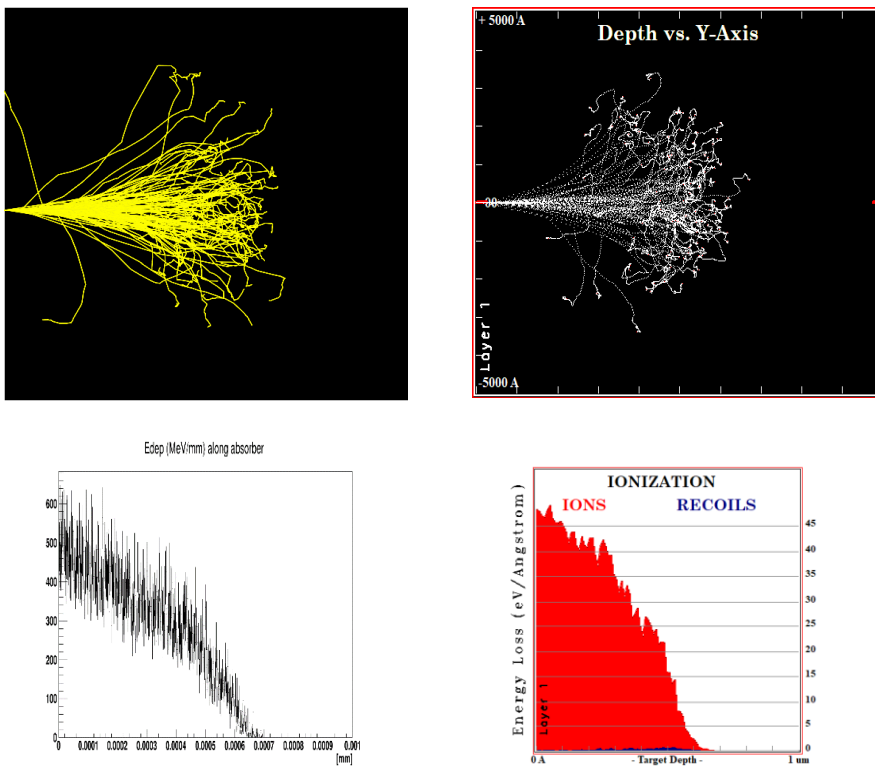


Figure 5-3. Range and scattering of 200 keV Alpha plotted in 1  $\mu\text{m}$  thick Ni from Geant4 (left) and SRIM (right)

### 5.2.3 Results

For the simulations, we chose a beam of alpha particles with energy 200 keV to correlate with the experimental results. Parameters varied in the simulations were the dimensions of the aperture or line width, incident angle of the beam, divergence of the beam to simulate realistic beam irradiation and gap between the mask and the resist plane.

#### 5.2.3.1 Simulation of 60 nm apertures

Figure 5-1 shows the geometry used for simulation. An aperture of 60 nm width was defined in a stencil of mask 1  $\mu\text{m}$  thickness. A PMMA sample of 400 nm thickness was placed in the back plane with varying distance between the mask and sample.

A simulation of 200 keV Alpha particle (100) is shown in Figure 5-4. Gap between Ni mask and PMMA is 0 nm. The position of the beam centre is kept 2 nm from the edge to show different scattering mechanism at play in the ion transmission through the mask. As can be seen, ions which are scattered upwards and come to rest within the mask layer. Some of the ions are scattered downwards and escape the mask layer only to be scattered again by the mask surface. There are multiple paths from here to be considered which also defines the resolution of the lithography using ions. Gorelick *et. al.* [128] used a similar strategy to test the level of scattering, which they concluded to be the limiting factor of the technique.

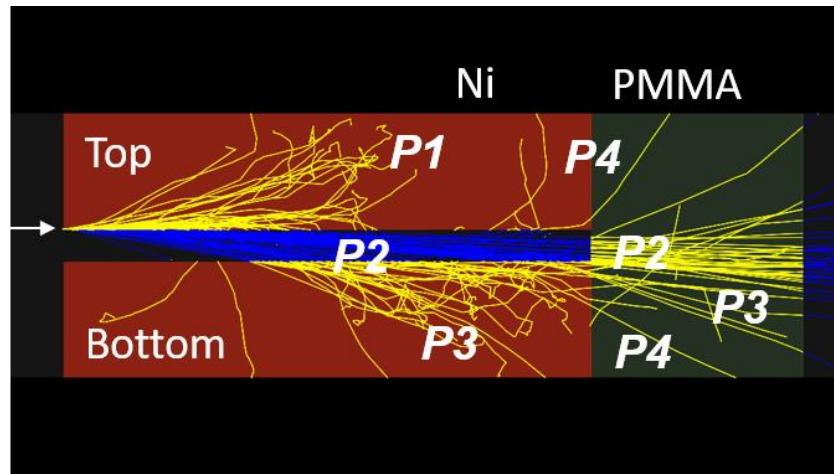


Figure 5-4. Edge scattering from the 60 nm aperture with a point beam of 200 keV alpha positioned 2 nm from the aperture edge.

Path 1 (P1): Large angle scattering events in the top layer of the mask results in these ions stopping within the mask layer.

Path 2 (P2): Low angle scattered ions; large proportion of these ions will escape the top layer only to be scattered from the bottom layer and lead to the paths discussed below. Rest of the ions that suffer large angle scattering further into the top layer will come to rest in the top layer. Based on the scattering angle, some of these ions will reach the resist plane or cross over to the bottom mask layer.

Path 3 (P3): Entering the bottom layer and large angle scattering; this will lead to ions either ending up in the bottom layer or again escaping the bottom layer

Path 4 (P4): Ions which are scattered at larger angle will make their way to the PMMA layer through multiple scattering in the bottom then top layer eventually reaching the PMMA layer or single interactions in the bottom layer and escape to the PMMA layer.

#### 5.2.4 Effect of edge scattering

Point beam of 200 keV alpha was placed at a distance varying from 2 nm to 200 nm and the ions reaching the PMMA surface were recorded for their energy and position. A 2 D image can be generated for the ion scatter position and energy map along with the energy spectrum.

Figure 5-5 shows the energy spectrum of the ions collected at the PMMA plane because of edge scattering as 100k particles are incident on the edge of the aperture. Yield is defined as the total number of ions collected in the energy bin of 1 keV normalized by the total number of incident ions (100k in this case).

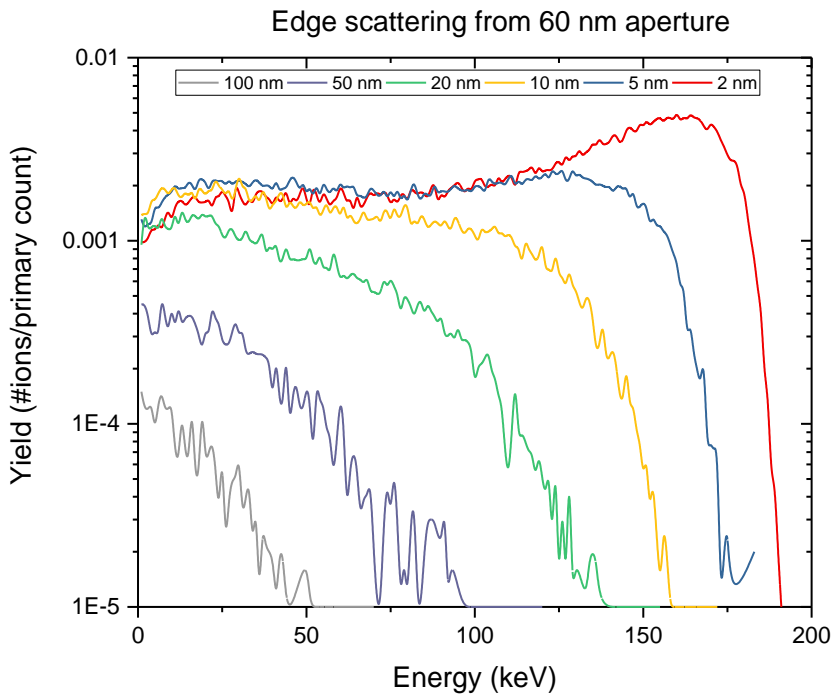


Figure 5-5. Edge scattering from the aperture edge with beam centre varied from 2 nm to 100 nm

The escape probability of the ions reaching the PMMA surface as a function of the beam centre position from the edge of the 60 nm aperture is plotted in Figure 5-6. The probability of the ions escaping reduced to <10% with the edge

position of 10 nm or more. It is noteworthy, to see the shift in the energy peak of the ions reaching the surface as function of the beam position from the edge. As the distance from the aperture edge increases, number of scattering for an ion within the mask layers increases. This leads to greater loss of energy through the mask layer. Besides the peak, the tail end of the spectrum reduces by an order of magnitude from the already 2 orders lower ions reaching the PMMA layer. Gorelick *et. al.* [128] modelled the edge scattering probability to be exponential decay. Fitting the exponential decay to the data, we arrive at a correction factor of 3.27 in the exponential decay parameter. This higher rate of reduction is expected due to the collimation provided by the two layers of the aperture as opposed to a single layer.

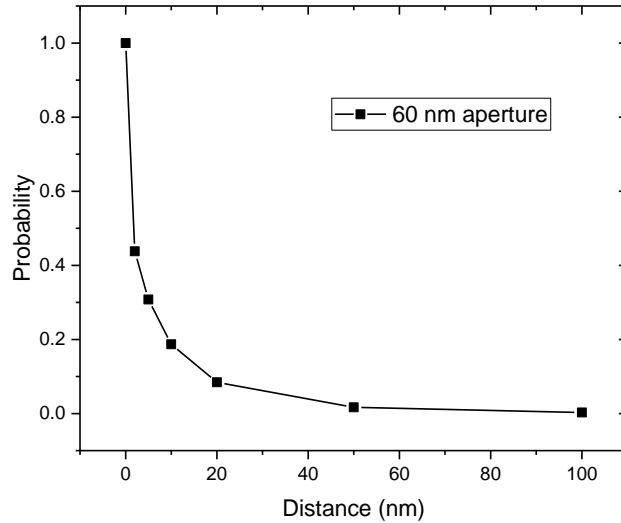


Figure 5-6. Escape probability of ions from the aperture with point beam centre moved away from the aperture edge.

Ions transmitting through the mask can be analysed for their energy and position upon reaching the PMMA surface. The scattering of ions can thus be plotted to extract spatial resolution of transmitted ions through the mask. On the other

hand, energy of the transmitted ions can be plotted as energy maps to represent the spatial distribution of ion energies reaching the PMMA surface. Both the scatter plots and energy maps are critical for quantifying the resolution of masked ion lithography. Figure 5-7 shows the scatter plots and energy maps of the case of edge beam scattering from the aperture for the case of 2 nm beam centre from the edge. As a comparison, scattering from 20 nm offset in the beam centre is also shown. The intensity as well as the average energy of the transmitted ions reduces as the incoming point beam is positioned further away from the aperture edge.

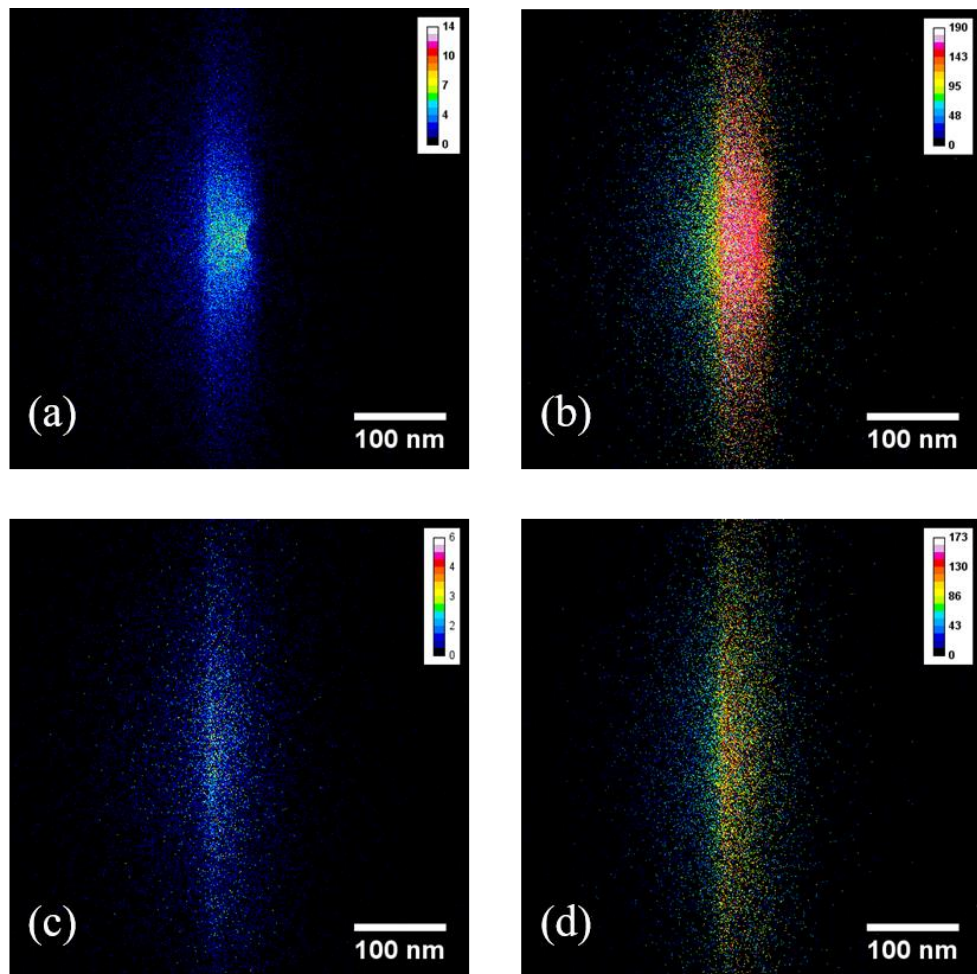


Figure 5-7. Scatter plot (a, c) and energy maps (b, d) shown for 2 nm (a, b) and 20 nm (c, d) from the aperture edge respectively

Next, a parallel beam of 200 keV alpha incident normally on the mask was studied for transmission with no gap between the PMMA and Ni mask. 100k alpha particles were simulated for the study. Figure 5-8 shows the scatter plot and the energy map of the transmitted ions through the Ni mask. The line profile across the aperture (refer Figure 5-9) is extracted from the image and averaged over the 490 nm length of the aperture. The line width of 60 nm is reproduced in the PMMA layer from the scatter plot.

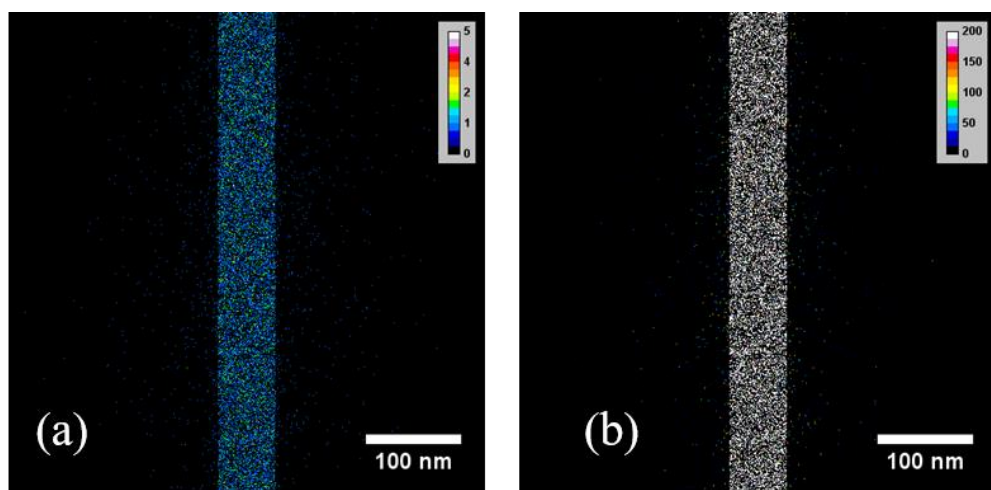


Figure 5-8. 200keV alpha transmission through a 60 nm aperture. (a) scatter plot, (b) energy map at the PMMA surface.

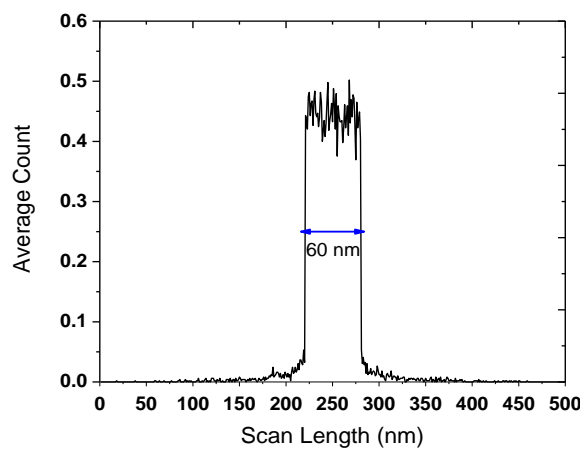


Figure 5-9. Line profile of the scattered ions on the surface of PMMA after transmission through the 60 nm aperture defined in Ni mask.

### 5.2.5 Simulation of 60 nm lines separated by 500 nm

The 60 nm lines from the mask separated by 500 nm spacing were simulated for the effect on the resolution. Factors affecting the resolution are edge scattering, beam divergence, incident beam angle and mask to sample gap.

A point beam is positioned 2 nm from the edge of the line. Figure 5-10 shows the scattering of 200 keV alpha incident normally on the line. The geometry is defined same as the mask features to study scattering and pattern transfer to the PMMA layer underneath encompassing an area of  $1.5 \times 1.5 \mu\text{m}^2$ .

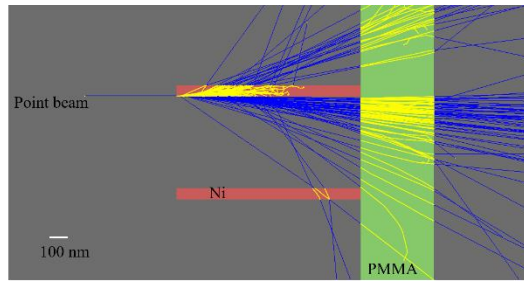


Figure 5-10. Geometry of two 60 nm lines spaced 500 nm centre to centre in Geant4.

A total of 100k alpha particle simulation was carried out by varying the distance from the edge of the line. Figure 5-11 shows the scattering yield from the lines. Yield is defined as the number of ions reaching the PMMA surface normalized by the total number of simulated ions.

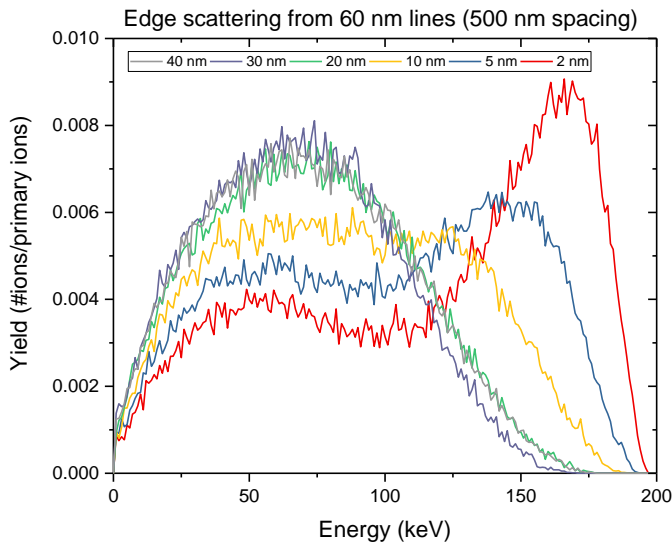


Figure 5-11. Edge scattering from the top 60 nm line with the point beam positioned at the edge of the line at varying distance.

Yield of ions close to the primary energy decreases as the position of the beam from the edge approaches the centre of the line (30 nm). Beyond that, due to symmetry, peaks shift back towards the incident energy. As seen from Figure 5-11, point beam positioned at 20 nm from the edge, gives a similar distribution as the beam positioned at 40 nm. Figure 5-12 shows the scatter plot and energy map comparison of 2 nm edge scattering to that of 20 nm.

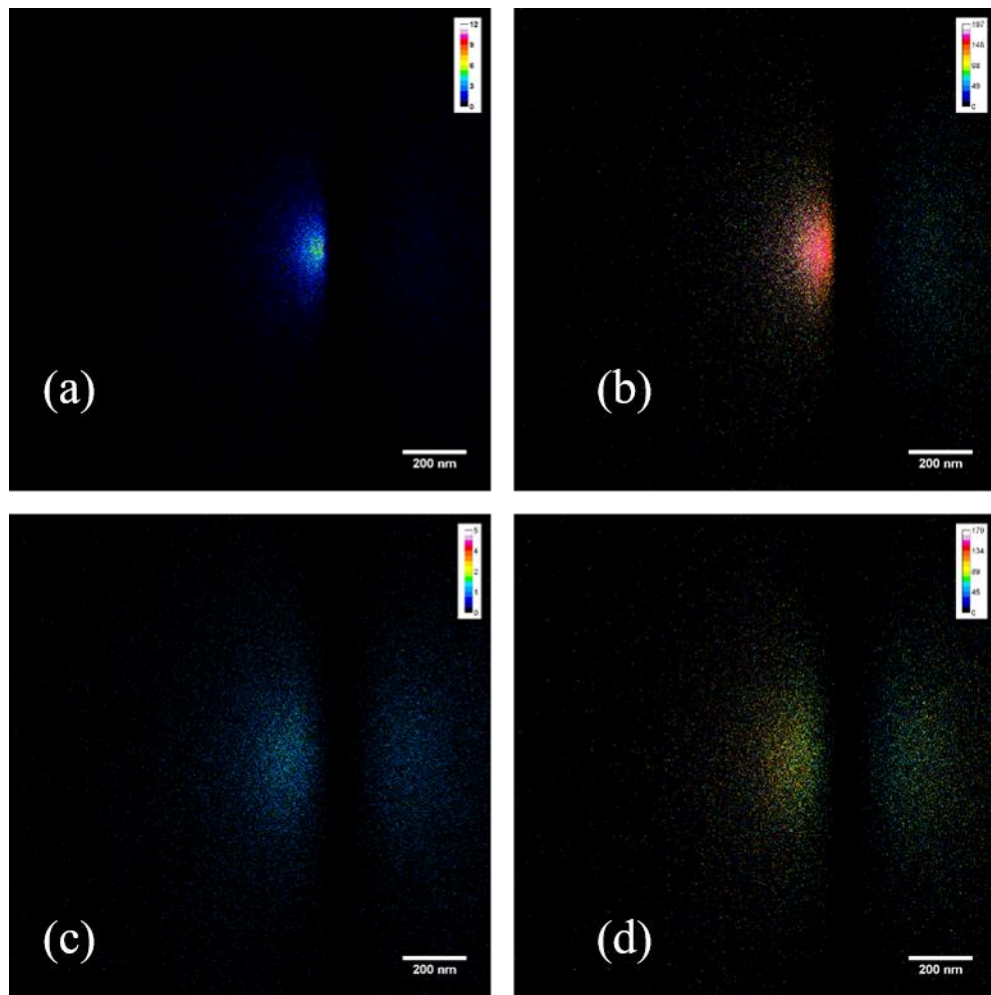


Figure 5-12. Edge scattering of 200 keV alpha landing on the PMMA surface. (a, c) shows the scatter plots and (b, d) images show the energy maps for the beam positioned at 2 nm from the edge and 20 nm respectively from the edge.

Escape probability of ions reaching PMMA is shown in Figure 5-13. Extent of the scattered beam 1  $\mu\text{m}$  below the mask on the PMMA surface is therefore beyond 60 nm under the line.

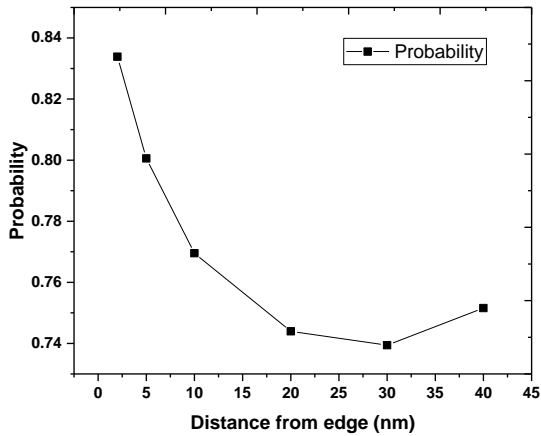


Figure 5-13. Escape probability of 200 keV ions at varying distance from the edge of the line.

Next, we simulate irradiation of a normally incident beam on the mask with no gap between the mask and resist layer. This is an ideal exposure condition with no beam divergence and beam tilt considered. Figure 5-14 shows the scatter plot and energy map of the simulation of 100k and 1 million alpha particles of 200 keV energy corresponding to dose irradiations of  $7.4 \text{ nC/mm}^2$  and  $74 \text{ nC/mm}^2$  respectively with a cut off 1 nm and step max of 1 nm. The total area is kept at  $1.5 \times 1.5 \mu\text{m}^2$ .

At  $74 \text{ nC/mm}^2$ , ten times the critical dose, the PMMA layer will get cross linked. However, for extracting line profile with decent statistics, we simulated for a higher dose. This serves two purposes- first it tells us what happens at higher ion dose in terms of the scattering; and secondly, it describes the energy distribution of scattered ions at the PMMA surface.

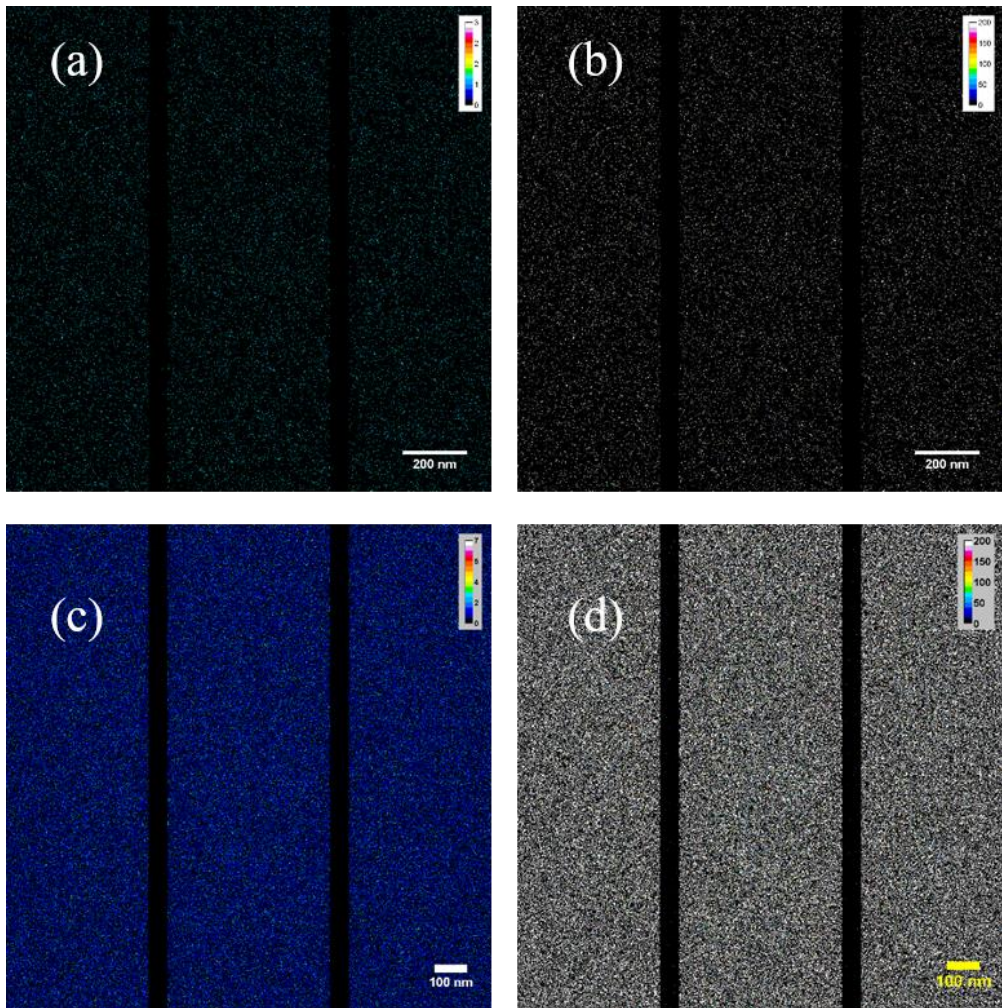


Figure 5-14. Scatter plot (a, c) of ions reaching the PMMA surface for 60 nm lines spaced 500 nm apart. Also shown are the energy maps (b, d) at the fluences for (a, b):  $10^5$  ions; (c, d):  $10^6$  ions

#### 5.2.6 Effect of beam divergence

Masked irradiation of PMMA was done using  $45^\circ$  beam line (previously  $30^\circ$  beamline [181]), which allows irradiation of wider areas. The distance from objective aperture to collimator aperture is 5.475 m. For the sizes of  $1.1 \times 1.1$  mm<sup>2</sup> and  $3 \times 3$  mm<sup>2</sup> of the object and collimator apertures respectively, a maximum beam divergence of 0.37 mrad can be expected. We simulated for the beam divergences ranging from parallel beam to 1 mrad when all the slits are fully open; the beam passes straight through the apertures and reaches the target chamber. Figure 5-15 shows the energy spectrum of the transmitted ions

reaching the PMMA surface at varying divergence. Number of particles simulated for this study was 1 million and the total area  $1.5 \times 1.5 \mu\text{m}^2$ .

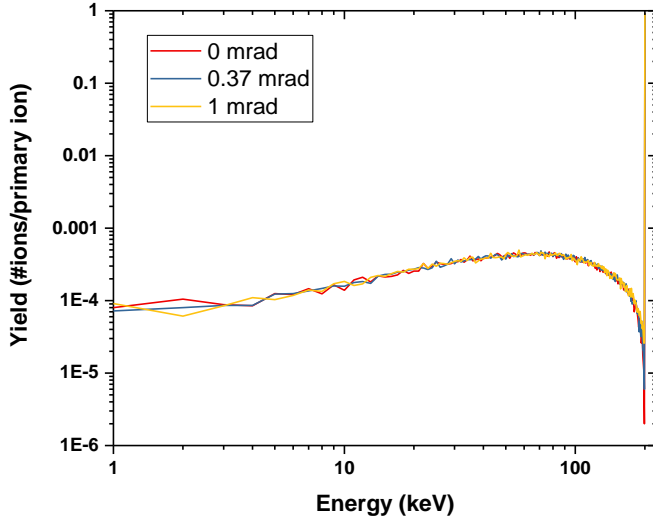


Figure 5-15. Effect of beam divergence on the energy spectrum of ions reaching the PMMA surface

The peak contribution to the spectrum at 200 keV reduces as the divergence increases since the ions encounter the mask features more. Besides, the contribution from ions losing less than 10 keV comes from the transmission of ions through the bottom layer of the masking lines due to increasing divergence. Thus, ions incident at grazing angles are scattered more. Figure 5-16 shows the scatter plot and energy map at beam divergence of 1 mrad. A line scan plotted in Figure 5-17 extracting the profile along the X direction shows minimal spread of the line feature as the beam divergence increases.

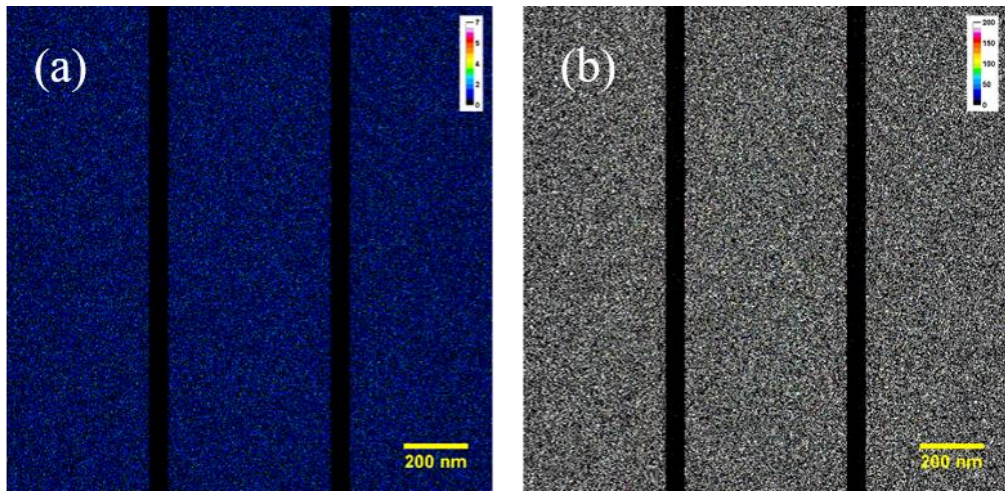


Figure 5-16. Scatter plot (a) and Energy map (b) for an incident beam divergence of 1 mrad

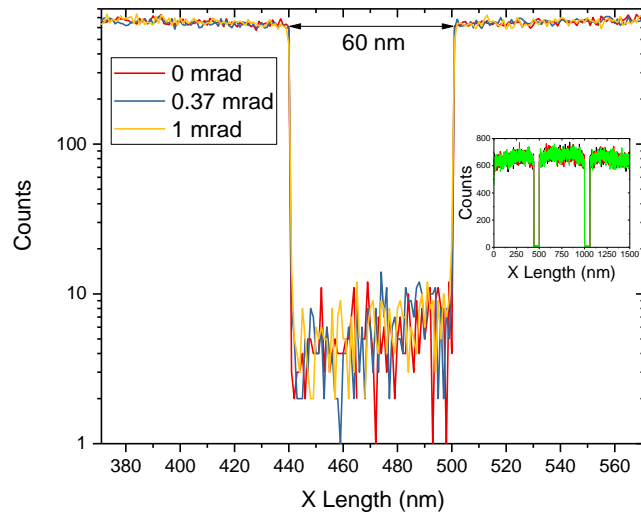


Figure 5-17. Line width variation as a function of incident beam divergence

### 5.2.7 Effect of mask-sample tilt with respect to beam

Table 5-1 below shows the critical angle for the feature size that is allowed, beyond which for apertures, no incident particle reaches the PMMA layer directly without being scattered through the mask. Figure 5-18 shows the line width reproduced in PMMA as a function of beam tilt with respect to the mask and sample stack. No gap was kept between the mask and PMMA for the

simulation. As is apparent, this is the most crucial parameter that limits the resolution of the pattern transfer. As the beam tilt reaches  $3.43^\circ$ , the transmission yield of the ions at lower energy increases as more scattering events are taking place.

Table 5-1. Critical angle vs aperture or line width.

Aperture/line size (nm)	Thickness (nm)	Critical angle (Degrees)
10	1000	0.57
60	1000	3.43
250	1000	11.31
400	1000	21.81

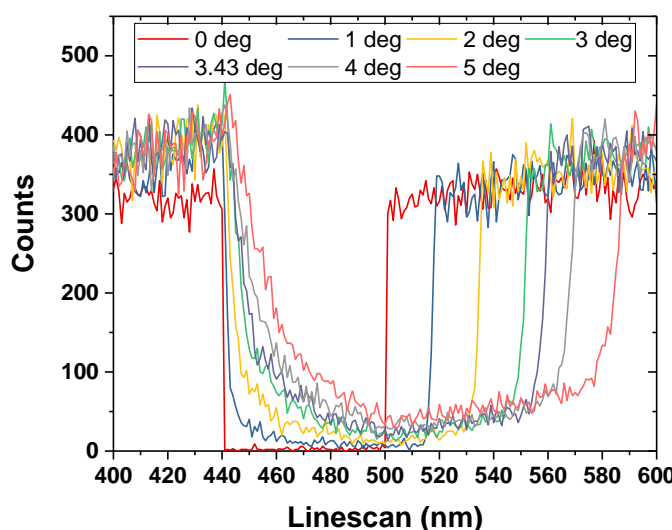


Figure 5-18. Line width vs beam tilt with respect to the mask-sample stack.

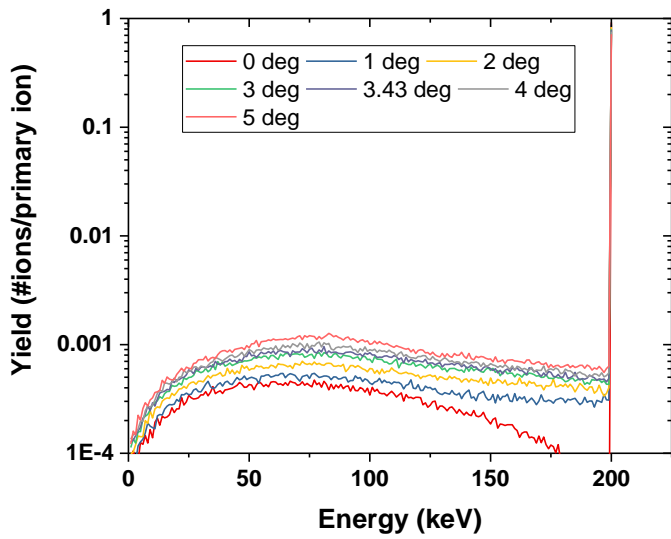


Figure 5-19. Energy spectrum of transmitted ions through the 60 nm lines at varying incident beam angle

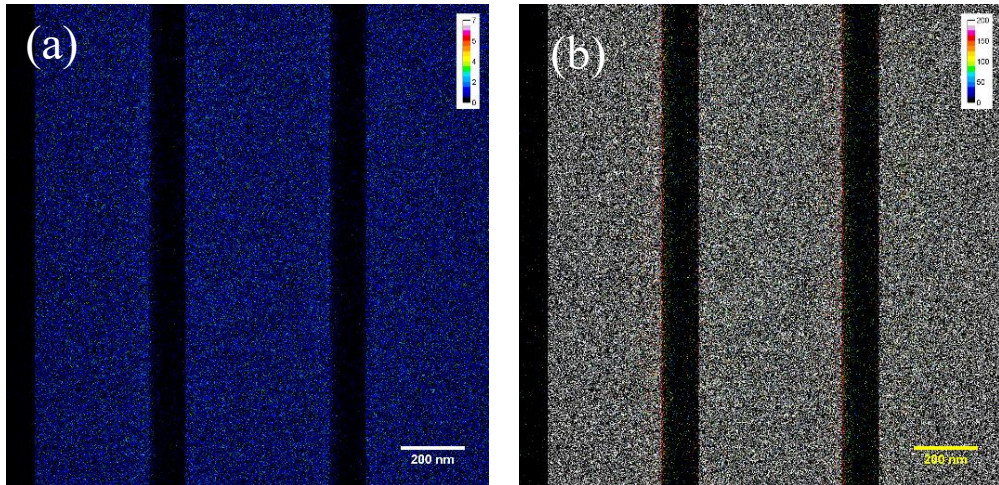


Figure 5-20. Scatter plot and energy map on the PMMA surface with beam tilt to  $3.43^\circ$

The line width increases as the beam tilt angle increases. Figure 5-19 shows the energy spectrum of the ions transmitted through the 60 nm lines at varying incident angle. As the beam tilt angle with respect to the mask-sample plane increases, more ions are scattered through the sidewalls of the line. Thus, contribution of low energy ions increases, which leads to an increase in the linewidth that is reproduced on the sample plane. Figure 5-20 shows the scatter

plot and energy map for the case of  $3.43^\circ$  beam tilt. A line width of 100 nm is observed.

#### 5.2.8 Effect of mask to sample gap

With the beam divergence set to 0.37 mrad corresponding to the experimental condition, we tested the model for the effect of gap between the sample and mask. Distances of 1  $\mu\text{m}$ , 10  $\mu\text{m}$  and 100  $\mu\text{m}$  were simulated for 1 million particles with an area of  $1.5 \times 1.5 \mu\text{m}^2$  for 200 keV alpha. No significant change could be found in the pattern transfer. Figure 5-21 shows the line scan extracted from the scatter plots as a function of varying space between sample and mask.

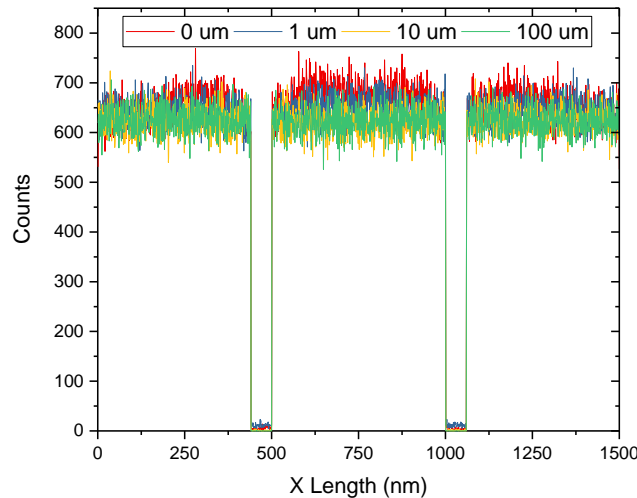


Figure 5-21. Effect of gap between mask and sample plane.

As seen from Figure 5-21, scattered beam composition is higher for close proximity of the sample and mask. As the mask to sample distance increases, scattered particles are diverged away, and as the distance increases, the average dose reduces by 10 %.

### 5.2.9 Simulation of 250 nm apertures

Similar sets of simulations were conducted for the 250 nm aperture and the limiting factor is still the beam angle alignment with respect to the mask-sample normal plane. Figure 5-22 shows the pattern transfer resolution with no gap between the sample and the mask for a simulation of perfectly collimated beam of 1 million alpha particles of 200 keV energy.

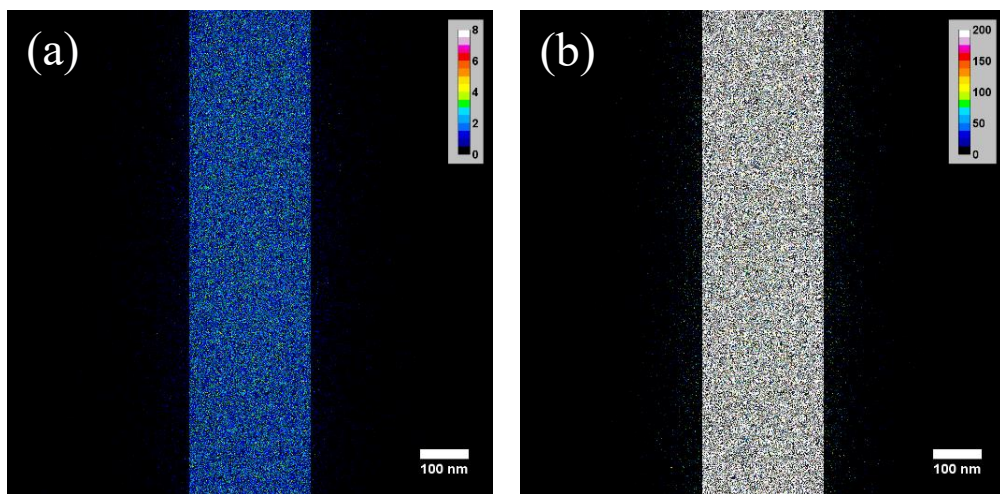


Figure 5-22. Pattern transfer of 250 nm aperture on the PMMA surface with irradiation of 200 keV alpha. (a) scatter plot and (b) shows the energy plot

### 5.2.10 Resolution test with 10 nm aperture

Simulation results with an aperture of 10 nm and 100k alpha particles of 200 keV is shown in Figure 5-23. An excellent pattern transfer is predicted from the model. These 10 nm apertures can be fabricated with straight and smooth vertical sidewalls using proton beam writing. Figure 5-23 shows the scatter plot and energy maps of the simulation performed.

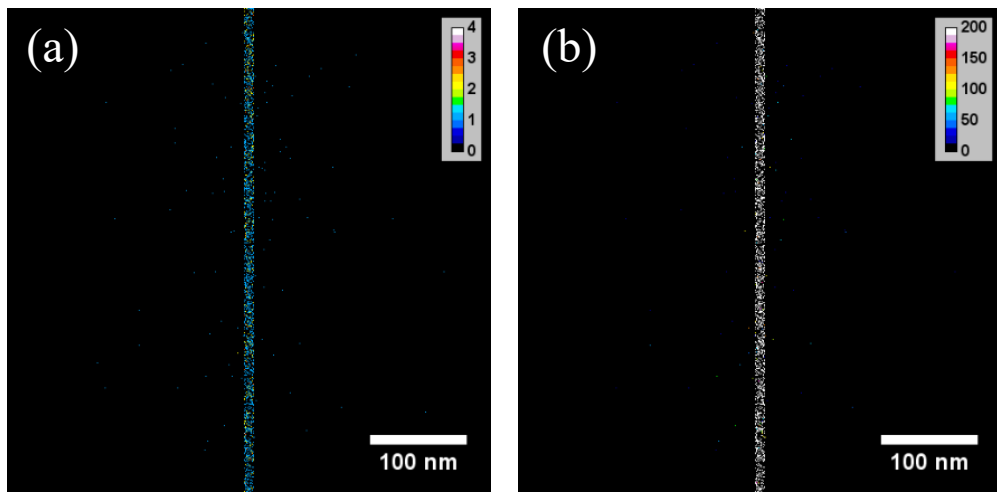


Figure 5-23. Simulation of ion transmission through a 10 nm aperture;(a) scatter plot and (b) energy map

#### 5.2.11 Simulation of lines and spaces

Simulations of 10 nm lines and spaces, and 60 nm lines and spaces are shown in Figure 5-24 and Figure 5-25 respectively, both of which indicate the resolution of the technique down to 10 nm mask features.

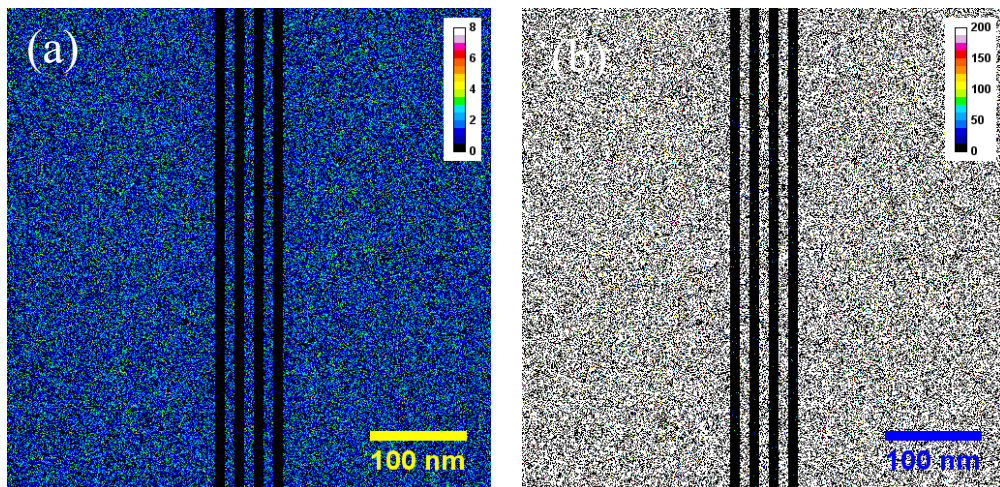


Figure 5-24. Simulation of 10 nm lines and spaces in 1  $\mu\text{m}$  thick Ni. ;(a) scatter plot and (b) energy map

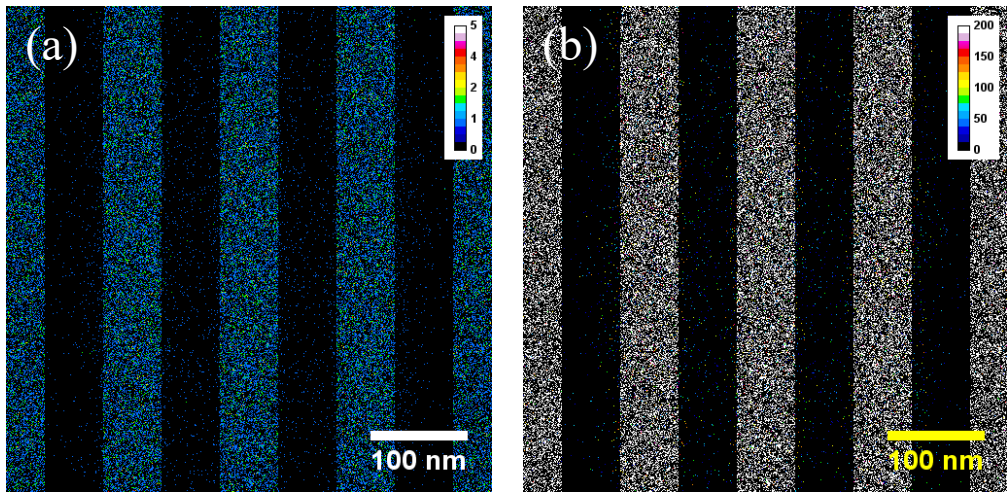


Figure 5-25. Simulation of 60 nm line and spaces in 1  $\mu\text{m}$  thick Ni; ;(a) scatter plot and (b) energy map

### 5.3 Summary

Proton beam writing using a focused beam is a serial process and therefore is slow due to lower reduced brightness of the RF ion sources. In this chapter we simulated the performance of masked ion lithography with the goal of higher throughput. A GEANT4 simulation was performed for apertures and lines in Ni with width ranging from 10 nm to 250 nm. A realistic beam of 200 keV alpha particles was modelled using General Particle Source to study the impact of parameters such as: edge scattering; beam incident angle; beam divergence; and sample to mask gap. The edge scattering through lines and apertures were analysed using point beam positioned at a known distance from the edge. It was found that smaller nano-apertures with vertical sidewalls offer reduced scattering compared to wider apertures. A lower fluence is observed with increasing beam divergence due to scattering within the mask. Similar observation is noted for increasing sample to mask gap wherein a lower fluence is registered at the sample plane to scattered ion trajectories. The most important parameter which affects the pattern transfer resolution is found to be the beam

incident angle with respect to the sample normal. The critical angle at which no (or all) particle from the incoming beam reaches the resist surface directly through the aperture (line) reduces for smaller linewidths. Masked ion beam through these simulations is predicted to be a viable method for pattern transfer of lines and spaces down to 10 nm. However, it is challenging to fabricate such 10 nm features with increased aspect ratios, approaching 100, required to stop the particles.

# 6 Masked Ion Lithography Experiments

## 6.1 Introduction

PBW has shown fabrication of high aspect ratio nano-structures with vertical sidewalls [182]. Nanoimprint molds fabricated from resist molds with features defined by PBW has shown promising pattern replication for higher throughput for nanofluidics [63]. Fabrication of high aspect ratio masks will thus enable to replicate pattern in both resist and non-resist based substrates at higher throughputs. In this chapter, we show fabrication process of high aspect ratio free-standing mask for the features simulated in chapter 5 with details down to 60 nm in Ni. We also characterize the performance of ma-N for high aspect ratio PBW. Finally, we validate the results from simulation detailed in chapter 5, through masked ion lithography performed using a broad beam of 200 keV alpha particles at 45° beamline in CIBA.

## 6.2 Mask fabrication in ma-N 2410

ma-N 2410 is a negative resist which has shown resolution down to 230 nm using Proton beam writing [183]. Parts of the resist exposed by protons get cross-linked and remain insoluble in developer. Using a negative resist also reduces the time to write the mask features due to reduced area required for exposure.

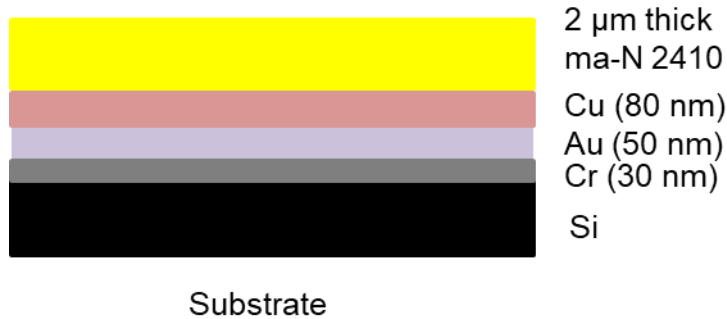


Figure 6-1.Sample for mask fabrication in maN 2410 and Ni plating

Schematic of the substrate prepared for mask (stencil) fabrication is shown in Figure 6-1. Silicon wafer was cleaned in acetone and IPA and blown dry using N<sub>2</sub>. The wafer was baked at 200°C to remove the moisture content from the surface. Electroplating seed layer was next deposited using sputter deposition. Layers of Cr (30 nm), Au (30 nm) and Cu (50 nm) were sputtered on top of the silicon wafer. ma-N 2410 was spin coated to a thickness of 2 μm on the sample. Proton exposure was done the next day. A PMMA sample was also prepared following the recipe described earlier (refer 4.1.1) for 2 μm thickness.

#### 6.2.1 Pillars written in ma-N

A beam of 2 MeV protons was focused to  $17 \times 35 \text{ nm}^2$  with the objective and collimator set at  $8 \times 4 \text{ } \mu\text{m}^2$  and  $20 \times 20 \text{ } \mu\text{m}^2$  at a reduced brightness of 6.99 A/m<sup>2</sup>srV (count rate of 20000 protons/s). We tried to test the resolution of ma-N resist by spot irradiation with the focused beam. An EPL format was written with a scan size of  $2.95 \times 2.574 \text{ } \mu\text{m}^2$  and pixel resolution of  $256 \times 256$ .

Two patterns were exposed with pitches of 100 and 200 nm. Table 6-1 lists the exposure parameters used for writing pillars in ma-N 2410. Dose was varied from 100 protons per pillar to 6500 protons per pillar. The sample was later

developed in maD-25 for 15s. Figure 6-2 shows the SEM image taken after 1  $\mu\text{m}$  Ni plating on the sample. Overlap of pillars can be seen from Figure 6-2 in Y direction and forming a line width of 50 nm written at a pitch of 100 nm. This is the smallest line width resolved in ma-N 2410 corresponding to an aspect ratio of 40. Although, no pillar row could be observed for the pitch 200 nm. This implies that writing high density features in ma-N is possible, although the structural stability is the limitation of the resist.

Table 6-1. Parameters for writing pillars in ma-N 2410

	100 nm pitch	200 nm pitch
Scan Size	$2.950 \times 2.574 \mu\text{m}^2$	$2.950 \times 2.574 \mu\text{m}^2$
Scan Voltage form DAQ	$10 \times 10 \text{ V}$	$10 \times 10 \text{ V}$
Pixel resolution	$256 \times 256$	$256 \times 256$
Pitch in pixels	10	20
Number of pixels written	484	100
Range of dwell time	105 $\mu\text{s}$ to 6.84 ms	105 $\mu\text{s}$ to 6.84 ms

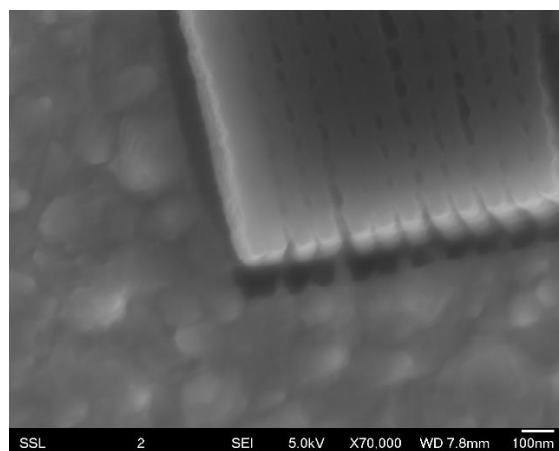


Figure 6-2. SEM images of pillars turned lines in ma-N shown after Ni plating

### 6.2.2 Grating writing in ma-N 2410

Grating discussed in chapter on simulation were written next after the object and collimator slits were opened to increase the count rate and accommodate writing features for larger scan area. With an object and collimator size set to  $28 \times 20 \mu\text{m}^2$  and  $40 \times 40 \mu\text{m}^2$ , a count rate of  $2.16 \times 10^6$  protons was established by keeping pin diode off-axis. The reduced brightness was measured to be  $10.81 \text{ A/m}^2\text{srV}$  with a spot size of  $42 \times 160 \text{ nm}^2$ . Scan size was set to  $50 \times 50 \mu\text{m}^2$ . Gratings with pitches of 1 and  $5 \mu\text{m}$  were written for varying dosage in the scan pattern. Figure 6-3 shows the scanned grating file used for writing 100 nm linewidth in ma-N. Three rows of varying line widths were fabricated in the resist in the range 100 nm, 200 nm and 300 nm.

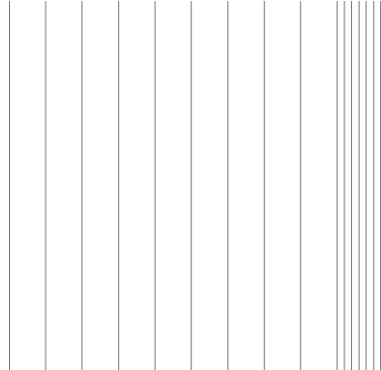


Figure 6-3. EPL layout for scanning. Shown are two grating pitches  $1 \mu\text{m}$  (right) and  $5 \mu\text{m}$  left

Scan area was digitized to 2048 pixels with an equivalent resolution of 24.41 nm ( $50 \mu\text{m}/2048$ ). Pixel width chosen for the three linewidths were 3 (100 nm), 6 (200 nm) and 9 (300 nm). Three rows were written with a separation of 100  $\mu\text{m}$  in Y direction. Each row had 9 regions of the same pixel width, with the regions exposed at 9 doses ranging from 20 to  $300 \text{ nC/mm}^2$  with a stage stepping

of 100  $\mu\text{m}$  in X direction. Total time for the exposure was 29.5 mins. Both the pillars and the grating were written on the same sample.

Figure 6-4 shows the developed features. Images were taken after development and before Ni plating. Features from left to right are written with increasing dosage. Line width increases from top to bottom (100 nm to 300 nm).

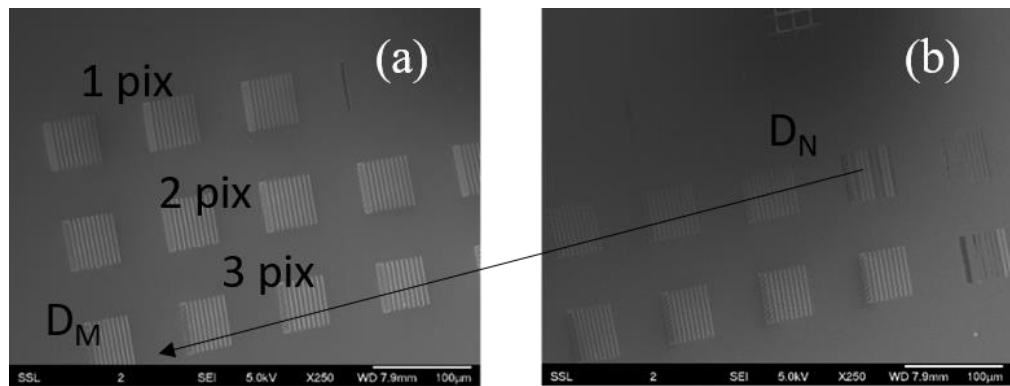


Figure 6-4. SEM image of full area of the grating written in ma-N 2410 after development. Dose increases from right to left and line width increases from top to bottom.  $D_M = 300 \text{ nC/mm}^2$  and  $D_N = 20 \text{ nC/mm}^2$

As with the case of pillars, the first thing that can be observed is the higher dose required to leave a feature stable enough after development. The minimum dose required to leave the grating feature for the 3-pixel line width is 200  $\text{nC/mm}^2$ . Only the last three dosages are seen in the image. While, a minimum dose of 70  $\text{nC/mm}^2$  is required for the 6-pixel linewidth, a minimum dose of 50  $\text{nC/mm}^2$  is necessary for the 9-pixel linewidth feature.

Figure 6-5 shows a high resolution of the image of the developed features with 3-pixel linewidth, written at a dosage of 300  $\text{nC/mm}^2$  and measured linewidths of 230 nm.

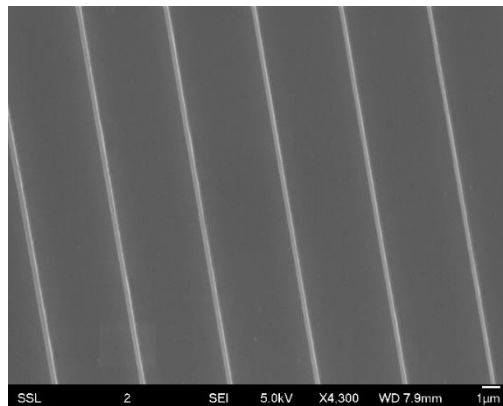


Figure 6-5. SEM image of 230 nm linewidth in ma-N after development written using 3 pixels

It is important to mention here that the resolution is also limited based on the adhesion of the resist to the sample. As observed for the pillars, even though a linewidth of 50 nm can be resolved, it's important to place the features closer. This is necessitated by the required structural stability of the resist features to withstand the surface tension in the developer due to poor adhesion of the resist with the electroplating seed layer coated on the silicon wafer. Figure 6-6 depicts the gratings written in PMMA after development.

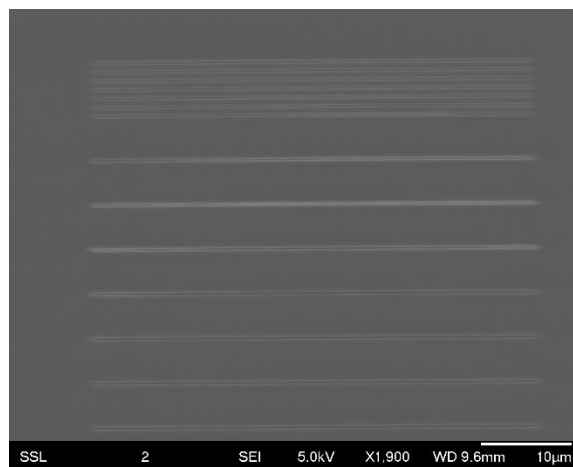


Figure 6-6. Grating in PMMA after development. showing line width of 200 nm

### 6.2.3 Ni electroplating

Pattern replication using Ni electroplating has been a vital tool for PBW replication used for applications like nanofluidics [183], [184]. Both the PMMA sample and ma-N sample were electroplated with 1  $\mu\text{m}$  thick Ni using a Ni sulfamate bath at a plating rate of 200 nm/min and  $8.49 \text{ mA/cm}^2$ . The adhesion of the photoresist proved to be the limiting factor in reproducing the developed feature in PMMA. Since the electroplating electrolyte seeps in the photo resist layer that is masking the non-exposed regions of PMMA, an underplating is observed as shown in Figure 6-7.

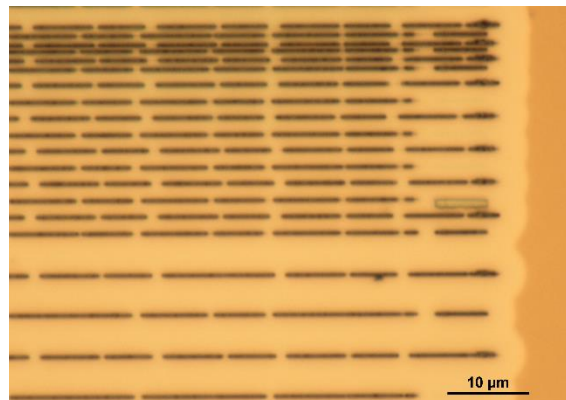


Figure 6-7. Ni lines of 200 nm at varying pitch of 500 nm to 5  $\mu\text{m}$  from top to bottom. Lines were resolved in PMMA and written with stage scan. Gaps in the lines are seen which result from non-uniform stage motion  
ma-N was stripped off in acetone for 1 hr at room temperature. We found that the removal of ma-N is dependent on the dose used as will be shown below for the case of 300 nm lines written with  $300 \text{ nC/mm}^2$ . Figure 6-8 shows the SEM Image of the sample after electroplating and before Cu etching.

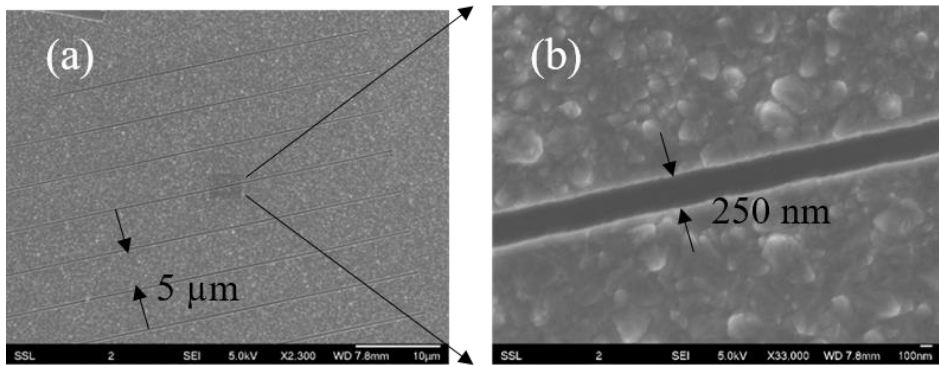


Figure 6-8. 250 nm wide apertures 50  $\mu\text{m}$  long in Ni after stripping ma-N 2410 in acetone. (a) shows the grating with 5  $\mu\text{m}$  pitch; (b) shows a high resolution of the 250 nm opening in 1  $\mu\text{m}$  thick Ni before Cu etching

Some of the lines are peeled off from the base allowing the electroplating to continue in its place. This can be seen from the edge of the line which seems to have moved and collapsed from its place. Image in Figure 6-8a shows the 250 nm apertures at a pitch of 5  $\mu\text{m}$ . Also, shown in Figure 6-8b is a high-resolution image of the aperture showing a bit rough edge. This roughness is the limitation of the photo resist as has been observed by van Kan *et al.* [185]. ma-N is completely removed in acetone within 1 hr. Figure 6-9 shows 300 nm lines fabricated using 9-pixel width after electroplating with left over ma-N in the aperture space due to higher degree of crosslinking.

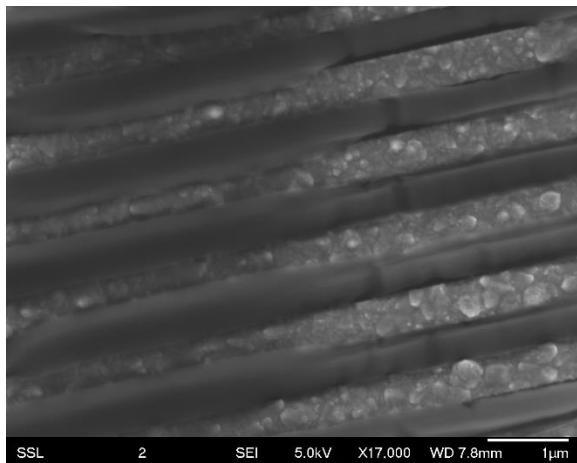


Figure 6-9. 300 nm gap in Ni masked by cross-linked ma-N which is harder to be removed in Acetone

Two major issues that limit the resolution of the resist are - adhesion to the substrate and resist swelling in acidic medium.

Ideal electroplating bath pH is maintained using a pH dosimeter which pumps sulfamic acid to control the pH level around 3.5. During the plating of these samples, the pH meter had malfunctioned. Measuring the pH of the bath, following the gross under-plating, using pH strips showed a pH of 1.5 to 2. Methyl acrylate resists are not stable in acidic environment. Therefore, following Ni electroplating, we couldn't see the 100 nm lines written using 3 pixel linewidth since they collapsed in the electrolyte. Also, the lines written as a grating with pitch of 1 μm were pulled closer during electroplating leading to a narrow gap of 60 nm between the lines. As the plating continues, the gap becomes stable as the sample doesn't spend much time in the electrolyte, and initial layer of electroplated Ni provides solid support and barrier for further motion. These lines of 60 nm width as shown in the SEM images (Figure 6-10c and d) only occur along the end of the exposed regions for both 230 nm and 300 nm linewidth areas.

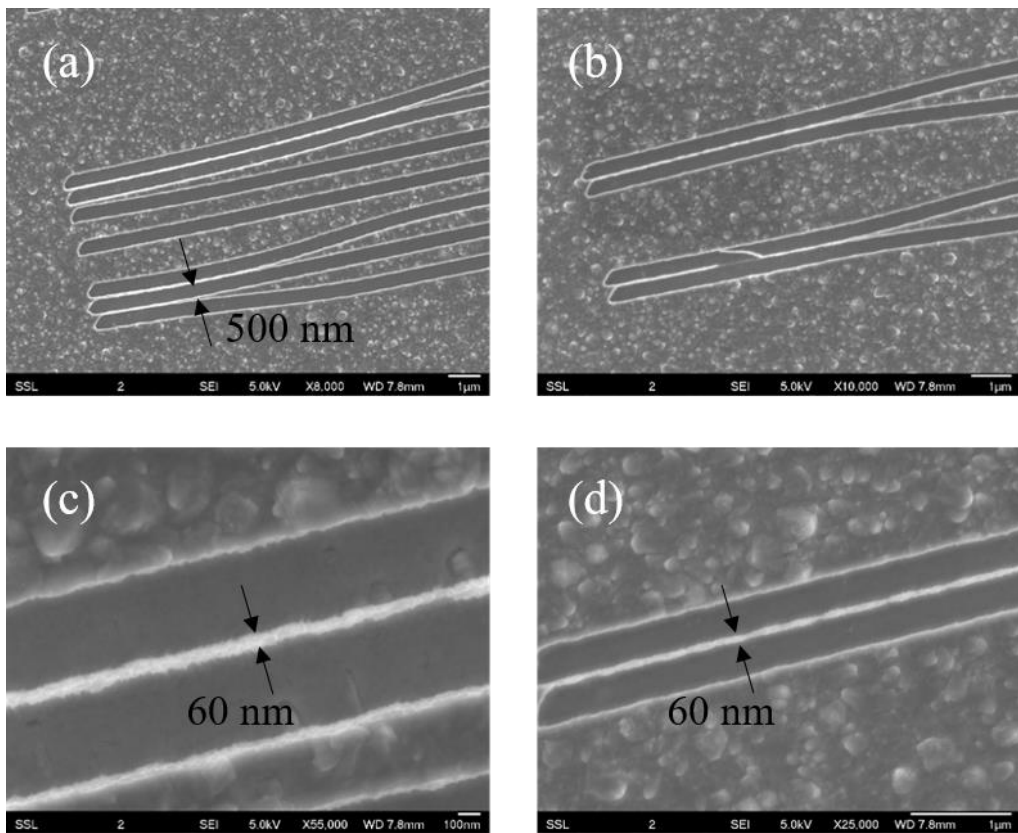


Figure 6-10. Mask features showing 60 lines in Ni after ma-N stripping but before Cu etching. (a) 500 nm spaced lines 60 nm wide at the edge of the grating region due to ma-N adhesion. (b), (c) and (d) shows 60 nm lines in Ni left after electroplating due to ma-N adhesion loss during Ni electroplating.

To make this 1 μm thick mask manageable, we covered the feature region with AZ 40XT and exposed it to UV (365 nm) following the process for fabrication of supporting grid for resolution standard. 100 μm Ni foil made by dummy plating was cut to a size of  $4 \times 4$  mm<sup>2</sup> and was used as mask rim for the UV exposure. Post development in TMAH, a 30 μm thick Ni electroplating (plating rate of 1.5 μm/min and current density of 63.65 mA/cm<sup>2</sup>) was carried out to cover the entire sample. This frame around the mask features makes it easy to handle and mount on the sample for further experiments.

#### 6.2.4 Cu etching

Etching of the sacrificial Cu layer was done using a mixture of acetic acid (5 vol%): H<sub>2</sub>O<sub>2</sub> (5vol%): De-ionized water (90 vol%). This etchant is highly selective to Cu and doesn't etch Ni. The etching is done at room temperature. Since the entire sample is plated with Ni, only sides and aperture defined on the sample are available for etching. It took about two days in the solution to etch the Cu layer underneath. The sample was later washed in DI water for 30 s. Figure 6-11 shows a photograph of the mask fabricated.

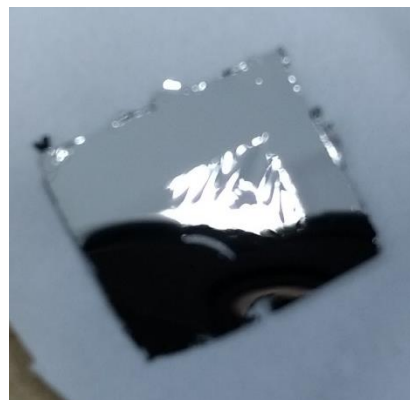


Figure 6-11. Mask with electroplated frame around to ease handling

#### 6.2.5 Experimental set-up

Helium (+1) ions were generated using the RF ion source and accelerated using a 200 keV terminal voltage. A mass selector magnet bends the beam towards an objective aperture. The beam is then steered to the target chamber using a switching magnet. Collimation is done before the magnetic scanner and the beam is scanned over the mask in the target plane.

PMMA A4 495k was spin coated on the wafer at 4000 RPM to a thickness of 200 nm. The sample was pre-baked at 180 °C for 2 mins. A second coat of PMMA A4 950k was spin coated on top to a target thickness of 200 nm followed

by another pre-exposure bake at 180 °C for 2 mins. The wafer was cleaved into pieces of 2 cm × 2 cm area and exposed using the mask placed directly on top of the PMMA layer. Since Ni is magnetic, a magnet was fixed on top of the sample holder using double sided carbon tape. PMMA spin coated wafer was then placed on top of the magnet and fixed using double sided carbon tape. Mask was brought at last on top of the PMMA layer by slowly positioning from one side. The magnet holds the mask firmly on top of the PMMA layer. Front face of electroplating is chosen to have contact with the PMMA layer because of the surface roughness close to the roughness of the electroplating seed layer of typically 2-3 nm. A gap of less than 500 nm was verified using an optical microscope.

The sample holder was attached to a three-axis manual stage to position the mask. Target chamber was pumped down to  $4 \times 10^{-5}$  mbar. Objective and collimator sizes of  $3 \times 3$  mm<sup>2</sup> and  $1.1 \times 1.1$  mm<sup>2</sup> were used with an equivalent maximum divergence of 0.37 mrad. The spot size was observed on the quartz piece mounted on top of the magnet to maintain the same plane. Beam spot observation and the sample positioning was done using a camera focused on the sample holder.

#### 6.2.6 Irradiation parameter

A beam spot size of  $1.2 \times 1.2$  mm<sup>2</sup> was observed on the quartz piece without focusing. A beam scanning of  $4 \times 4$  mm<sup>2</sup> was done using Oxford Microbeam OM50e magnetic scanner. Scanning was pixelated using IonDAQ interface with  $256 \times 256$  pixels equivalent of 15.6 μm per pixel scan size. Entire scan area was scanned multiple times to deposit even dose to the sample. Scanning introduces

a tilt in the sample plane with respect to beam to a maximum tilt of  $0.11^\circ$ , which according to the simulation, doesn't affect the beam resolution beyond 5 nm. Exposure was done at a beam current of 0.88 nA. Centre of the scan field was kept at the centre of the mask to irradiate the entire mask. Table 6-2 lists the parameters used for the exposure which were scaled from the optimized dose used for writing with a focused 2 MeV proton beam at typical exposure timing of 30 s. A good match is observed from the SRIM estimation of the dose range. This further confirms that the sensitivity for the PMMA layer using  $\text{He}^+$  at 200 keV is 10 times higher than 2 MeV protons. Samples were developed using IPA: DI water mixture at 7:3 volume ratio for 2.5 min.

Table 6-2. Optimum dose comparison from SRIM

Ion	Ion Energy (keV)	Stopping Power (keV/ $\mu\text{m}$ )		Optimum Dose (nC/mm $^2$ )	
		Electronic	Nuclear		
Proton	2000	19.23	$1.27 \times 10^{-2}$	100	200
Helium	200	200.8	1.207	9.5	19.1

### 6.2.7 Developed feature

The samples were coated with  $\sim 2$  nm of Pt to image using low energy SEM and to avoid charging of the sample during electron irradiation. Figure 6-12 shows the SEM image of the sample with an irradiation of  $2.4 \text{ nC/mm}^2$  dose. The features appear under-developed due to the presence of a rough PMMA base layer. Due to the metal coating on top, the sample couldn't be developed any further. Nevertheless, the features could be seen to follow the pattern on the mask. Image shows two 69 nm lines spaced 500 nm apart. In Figure 6-12, lines

of 269 nm are resolved with rough base layer due to under-exposure. This dose is half the optimum dose obtained with SRIM comparison.

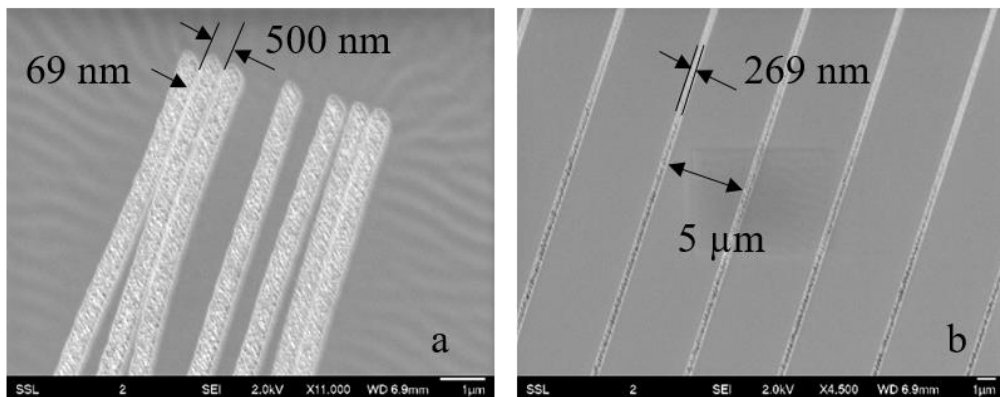


Figure 6-12. SEM image of (a) 69 nm linewidth in PMMA written with a beam of 200 keV He<sup>2+</sup> at a dose of 2.5 nC/mm<sup>2</sup>. (b) 269 nm channels written with 250 nm aperture in Ni

As the dose is increased, the sample is fully developed. For a dose of 9.5 nC/mm<sup>2</sup> (the estimated optimum dose), we could see from the SEM image (refer Figure 6-13a) that the line of 69 nm is transferred to a fully developed PMMA. A line width of 65 nm is seen from the image. This gives an aspect ratio of 6.15. However, only one of the two lines could be seen in the exposed area. This implies the collapsing of the lines during development. Figure 6-13b shows the 314 nm line widths exposed through 250 nm aperture at a dose of 9.5 nC/mm<sup>2</sup>.

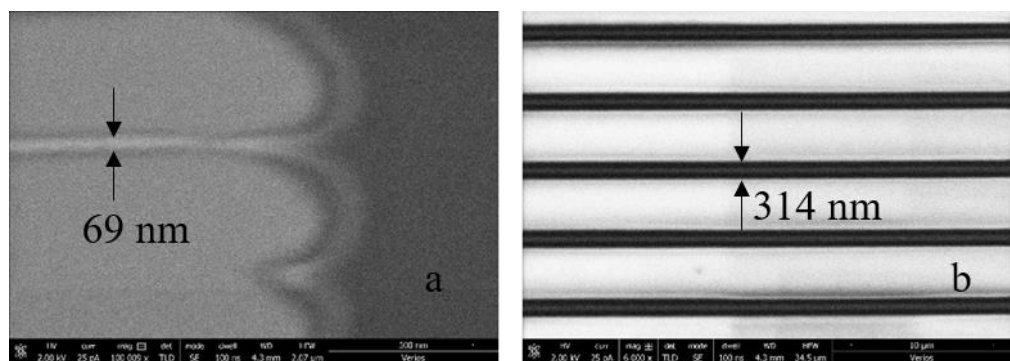


Figure 6-13. SEM image of (a) 69 nm linewidth and (b) 314 nm linewidth in 400 nm thick PMMA written with a beam of 200 keV He<sup>2+</sup> at a dose of 9.5 nC/mm<sup>2</sup>

At even higher dosage, the 60 nm lines collapse and are not seen in the image. Figure 6-14 shows the SEM image of the 250 nm aperture region exposed using  $15 \text{ nC/mm}^2$ . The line width increases to 540 nm.

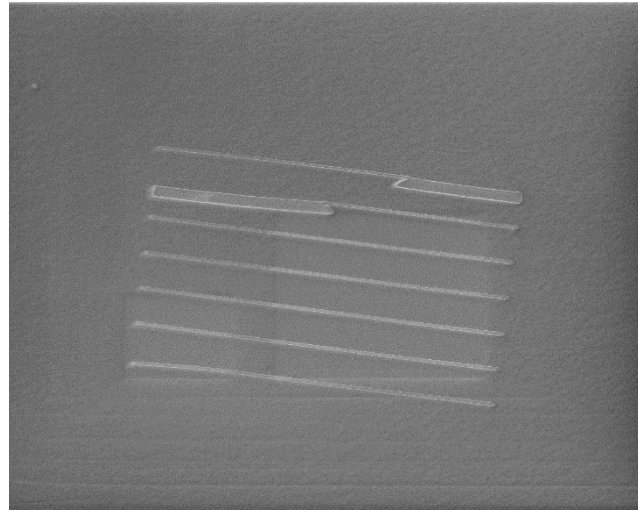


Figure 6-14. 260 nm lines reproduced in PMMA layer written with a beam of 200 keV  $\text{He}^{2+}$  at a dose of  $9.5 \text{ nC/mm}^2$

### 6.3 Summary

Fabrication of 50 nm merged pillars was shown in 2  $\mu\text{m}$  thick ma-N 2410 matching the beam size in X direction. This is the smallest feature size resolved in ma-N 2410 using charged particle lithography. Fabrication of 230 nm lines in ma-N with an aspect of  $\sim 9$  was also described improving the pattern transfer to Ni by half compared to earlier works with ma-N 2410 [183]. Due to adhesion loss, displacement of ma-N lines was observed during electroplating leading to lines of 60 nm being electroplated with Ni. A stencil mask was fabricated by Cu etching and supporting frame fabrication using UV exposure and Ni electroplating. A Monte Carlo simulation using Geant4 toolkit was carried out to study effects of scattering from the mask features on photo resist. Masked irradiation results were shown with feature replication down to 69 nm. Geant4

model was extended to study the pattern transfer capability of the masked ion lithography down to 10 nm lines and spaces.

## 7 Conclusion and future work

PBW is a serial process using a beam of focused protons accelerated to MeV energies. Low reduced brightness (6 orders) of the RF ion source compared to electron sources used in EBL makes focusing of the proton beam challenging. In this thesis, we addressed three major challenges related to focusing proton beam under sub-20 nm: positioning, imaging and alignment.

Maintaining the correct depth of focus with higher demagnification system was achieved by implementing a closed loop positioning system which enables sample focal plane positioning offset of less than 500 nm. This limits the broadening in the sample plane of a 2 MeV proton beam to 2 nm in X direction and 0.5 nm in Y direction for object and collimator aperture openings of  $8 \times 4 \mu\text{m}^2$  and  $30 \times 30 \mu\text{m}^2$  respectively.

Beam size estimation is done after imaging a resolution standard using scanning transmission ion microscopy (STIM) modelled as a complementary error function. The accuracy of the beam size estimation depends greatly on the sidewall slope of the resolution standard. However, direct measurement of side wall slop for sub- $\mu\text{m}$  thick resolution standard is challenging using SEM. We showed that STIM can be used to measure the thickness of the for sub- $\mu\text{m}$  thick resolution standards and estimate their side wall slope. Through STIM characterization, we experimentally measured the thickness of a Ni resolution standard to be  $0.9 \pm 0.1 \mu\text{m}$  and a side wall slope estimate of  $6.0 \pm 0.6 \text{ nm}$ .

Besides STIM, secondary electrons induced by transmitting ions through the resolution standard can be collected for estimating the beam spot size. Using an

MCP, we showed that a bias optimization leads to an improvement in the secondary electron collection efficiency for the MCP detector. We showed that fabrication of a Au resolution standard leads to a higher secondary electron collection efficiency compared to Ni resolution standard. Using a modified resolution standard fabrication process, a 190 nm thick Au resolution standard was fabricated using sputtering and metal lift-off. This is the thinnest free-standing resolution standard fabricated so far using PBW. It was also shown that the secondary electron collection efficiency is proportional to the stopping power of the ion in the resolution standard. Enhanced secondary electron collection of 92 % electrons per proton was shown for the Au grid for a beam of 500 keV  $\text{H}_2^+$ . Besides an enhanced collection efficiency, this Au grid also extends the capability of PBW at energies down to 250 keV.

Finally, we showed the effect of quadrupole lens misalignment on the focused spot size. The direction with lower demagnification was shown to be affected severely with rotational misalignment. A comparison of collimator slit translation was shown to characterize system misalignment. Using STIM, a quadrupole system alignment was described which is shown to be effective in removing higher order misalignments. A beam focusing of  $13 \times 32 \text{ nm}^2$  was achieved in agreement with the system demagnification. An automated slit alignment system is implemented towards reproducible slit alignment in both object and collimator apertures. A backlash of  $1.375 \mu\text{m}$  was measured experimentally using a focused beam of 1 MeV  $\text{H}_2^+$  ions with a positioning repeatability of 375 nm. This backlash and repeatability is combined with the transparency window of the ions the slits which is challenging to be decoupled from the systematic backlash of the micrometre gear system. An alternative

approach to minimize the backlash is by moving the slits from a closed position wherein all the slits only move outward from the beam axis. This approach however, requires greater stability of the beam with respect to the slit axis centre and doesn't take into account the beam centre position variation from run-to-run. Using automated slit alignment and focusing, we showed an optimal beam focusing of  $23 \times 35 \text{ nm}^2$ .

With an optimized auto-focusing system, we showed the characterization of PBW in photo-resists with sub-100 nm stitching error in X direction. However, Y direction limits the stitching error to a minimum of 500 nm due to the stage motion against gravity and stepper motion due to a slower controller.

Nanograting fabrication with 200 nm lines and 300 nm spacing over scan size of 100  $\mu\text{m}$  was demonstrated in PMMA. Fabrication of 30 nm channels in 2  $\mu\text{m}$  thick PMMA with an aspect ratio of 67 was shown. This is the smallest feature size written in PMMA to the best of our knowledge. Replication of 30 nm channels to Ni lines was demonstrated using electroplating. Nano-grating fabrication of 200 nm channels (aspect ratio 10) was shown in 2  $\mu\text{m}$  thick PMMA at pitches of 500 nm and 1  $\mu\text{m}$ . Using metal lift-off on 400 nm thick PMMA, we showed fabrication of 174 nm wide Cu lines of 30 nm thickness and a Cr base of 10 nm. Adhesion of PMMA was found to be the limiting factor in patterning using PBW and subsequent electroplating wherein under-plating was observed in unexposed PMMA regions for the substrates coated with Au/Cu.

In HSQ, we demonstrated fabrication of 30 nm pillars, and 50 nm lines. A nano-imprint mold with 42 nm lines was fabricated in HSQ and copied twice in

Ormostamp for nanofluidics. A nanofluidic chip was fabricated using imprinting and thermal bonding in PMMA. This chip is intended to study the behaviour of DNA molecules in nano-channels with dimensions lower than the persistence length of a DNA (50 nm). High aspect ratio channels with dimensions of 100 nm were fabricated using PBW and electrochemical etching in p-type Si. Besides, 5 mm long waveguides were fabricated in STO at varying pitches using stage scan.

Fabrication of 50 nm merged pillars was shown in 2  $\mu\text{m}$  thick ma-N 2410 matching the beam size in X direction. This is the smallest feature size resolved in ma-N 2410 using charged particle lithography. Fabrication of 230 nm lines in ma-N 2410 was also described (aspect ratio  $\sim 9$ ). Grating patterns were written with varying pitches and line widths. Poor adhesion limits the transfer of pattern to Ni below 250 nm (a factor to 2 reduction in the Ni transfer). Due to adhesion loss, displacement of ma-N lines was observed during electroplating leading to lines of 60 nm being electroplated with Ni. A stencil mask was fabricated by Cu etching and supporting frame fabrication using UV exposure and Ni electroplating. A Monte Carlo simulation using Geant4 toolkit was carried out to study effects of scattering from the mask features on photo resist. Masked irradiation results were shown with feature replication down to 69 nm. Geant4 model was extended to study the pattern transfer capability of the masked ion lithography down to 10 nm lines and spaces.

A realistic beam of 200 keV alpha particles was modelled using General Particle Source to study the impact of parameters such as: edge scattering; beam incident angle; beam divergence; and sample to mask gap. The edge scattering through

lines and apertures were analysed using point beam positioned at a known distance from the edge. It was found that smaller nano-apertures with vertical sidewalls offer reduced scattering compared to wider apertures. A lower fluence is observed with increasing beam divergence due to scattering within the mask. Similar observation is noted for increasing sample to mask gap wherein a lower fluence is registered at the sample plane to scattered ion trajectories. The most important parameter which affects the pattern transfer resolution is found to be the beam incident angle with respect to the sample normal. The critical angle at which no (or all) particle from the incoming beam reaches the resist surface directly through the aperture (line) reduces for smaller linewidths. Masked ion beam through these simulations is predicted to be a viable method for pattern transfer of lines and spaces down to 10 nm. However, it is challenging to fabricate such 10 nm features with increased aspect ratios, approaching 100, required to stop the particles. Besides, free standing stencils can only be used for open patterns such as lines or holes. Closed structures such as Fresnel rings need support for the mask structure making it difficult to pattern as a free-standing stencil.

The major bottleneck of the proton beam writing is the limited reduced brightness from the RF ion sources. A Nano-aperture ion sources (NAIS) has been developed and optimized at CIBA [186] and Delft [187] which shows an improvement of three orders higher reduced brightness compared to RF ion sources. A compact proton beam writing system [188] is based around NAIS, which will be a smaller foot-print system towards sub-10 nm lithography.

## List of publications

1. S. Qureshi, P. S. Raman, A. Stegmaier, and J. A. van Kan, “Quadrupole lens alignment with improved STIM and secondary electron imaging for Proton Beam Writing,” *Nucl. Instruments Methods Phys. Res. Sect. B Beam Interact. with Mater. Atoms*, vol. 404, pp. 74–80, 2017.
2. Liang, H.D., Dang, Z.Y., Wu, J.F., van Kan, J.A., S. Qureshi, Ynsa M.D., Torres-Costa, V., Maira, A., Venkatesan, T.V., Breese, M.B.H., “High aspect ratio channels in glass and porous silicon,” *Nucl. Instruments Methods Phys. Res. Sect. B Beam Interact. with Mater. Atoms*, vol. 394, 2017.
3. R. Basak, F. Liu, S. Qureshi, N. Gupta, Ce Zhang, R. de Vries, J. A. van Kan, S. T. Dheen, and J. R.C. van der Maarel “Linearisation and labelling of single-stranded DNA for optical sequence analysis”. Submitted Nucleic Acids Research, 2018
4. S. Qureshi, Wu Jiacheng, and J. A. van Kan “Automated alignment and focusing system for Nuclear Microprobes”, submitted to *Nucl. Instruments Methods Phys. Res. Sect. B Beam Interact. with Mater. Atoms*
5. S. Qureshi and J. van Kan, “Fabrication of high aspect ratio 30 nm features in PMMA”, in preparation
6. S. Qureshi, S. Vajandar, T. Basu and Jeroen van Kan, “Fabrication and simulation of high aspect ratio mask for fast nano-replication”, in preparation

## References

- [1] R. F. Pease and S. Y. Chou, “Lithography and other patterning techniques for future electronics,” *Proc. IEEE*, vol. 96, no. 2, pp. 248–270, 2008.
- [2] T. M. Bloomstein, M. F. Marchant, S. Deneault, D. E. Hardy, and M. Rothschild, “22-nm immersion interference lithography,” *Opt. Express*, 2006.
- [3] L. Capodieci, “From optical proximity correction to lithography-driven physical design (1996-2006): 10 years of resolution enhancement technology and the roadmap enablers for the next decade,” in *Optical Microlithography Xix, Pts 1-3*, 2006.
- [4] M. D. Levenson, N. S. Viswanathan, and R. A. Simpson, “Improving Resolution in Photolithography with a Phase-Shifting Mask,” *IEEE Trans. Electron Devices*, 1982.
- [5] B. S. Haran *et al.*, “22 nm technology compatible fully functional  $0.1 \mu\text{m}^2$  6T-SRAM cell,” in *2008 IEEE International Electron Devices Meeting*, 2008, pp. 1–4.
- [6] “International Technology Roadmap for Semiconductors (ITRS),” 2015. [Online]. Available: <http://www.itrs2.net/itrs-reports.html>.
- [7] T. Ito and S. Okazaki, “Pushing the limits of lithography,” *Nature*, vol. 406, no. 6799, pp. 1027–1031, 2000.
- [8] F. WATT, A. A. Bettoli, J. A. Van Kan, E. J. Teo, and M. B. H. Breese, “Ion beam lithography and nanofabrication: a review,” *Int. J. Nanosci.*, vol. 4, no. 03, pp. 269–286, 2005.
- [9] L. J. Guo, “Nanoimprint lithography: Methods and material requirements,” *Adv. Mater.*, 2007.
- [10] S. Natarajan *et al.*, “A 14nm logic technology featuring  $2^{nd}$ -generation FinFET, air-gapped interconnects, self-aligned double patterning and a 0.0588 SRAM cell size,” in *2014 IEEE International Electron Devices Meeting*, 2014, p. 3.7.1-3.7.3.
- [11] I. Englard *et al.*, “Metrology challenges for advanced lithography techniques,” 2007, vol. 6518, p. 65181G.
- [12] R. Jonckheere, A. Wong, A. Yen, K. Ronse, and L. Van den hove, “Optical proximity correction: Mask pattern-generation challenges,” *Microelectron. Eng.*, vol. 30, no. 1–4, pp. 115–118, Jan. 1996.
- [13] L. Bocquet and E. Charlaix, “Nanofluidics, from bulk to interfaces,”

*Chem. Soc. Rev.*, vol. 39, no. 3, pp. 1073–1095, Feb. 2010.

- [14] R. Marie and A. Kristensen, “Nanofluidic devices towards single DNA molecule sequence mapping,” *Journal of Biophotonics*. 2012.
- [15] L. Ying and Q. Wang, “Microfluidic chip-based technologies: Emerging platforms for cancer diagnosis,” *BMC Biotechnology*. 2013.
- [16] R. Ostafe, R. Prodanovic, W. L. Ung, D. A. Weitz, and R. Fischer, “A high-throughput cellulase screening system based on droplet microfluidics,” *Biomicrofluidics*, 2014.
- [17] M. H. Kryder *et al.*, “Heat Assisted Magnetic Recording,” *Proc. IEEE*, 2008.
- [18] T. R. Albrecht *et al.*, “Bit-Patterned Magnetic Recording: Theory, Media Fabrication, and Recording Performance,” *IEEE Trans. Magn.*, vol. 51, no. 5, pp. 1–42, May 2015.
- [19] J. S. Meena, S. M. Sze, U. Chand, and T. Y. Tseng, “Overview of emerging nonvolatile memory technologies,” *Nanoscale Res. Lett.*, 2014.
- [20] S. S. P. Parkin, M. Hayashi, and L. Thomas, “Magnetic domain-wall racetrack memory.,” *Science*, vol. 320, no. 5873, pp. 190–4, Apr. 2008.
- [21] J. O. Choi, J. A. Moore, J. C. Corelli, J. P. Silverman, and H. Bakhru, “Degradation of poly(methylmethacrylate) by deep ultraviolet, x-ray, electron beam, and proton beam irradiations,” *Cit. J. Vac. Sci. Technol. B Microelectron. Process. Phenom.*, vol. 6, p. 2286, 1988.
- [22] R. A. B. Devine, J. W. Tringe, and J. R. Chavez, “Radiation-induced charge trapping in low-k silsesquioxane-based intermetal dielectric films,” *IEEE Trans. Nucl. Sci.*, vol. 49, no. 6, pp. 2729–2732, Dec. 2002.
- [23] J. K. W. Yang *et al.*, “Understanding of hydrogen silsesquioxane electron resist for sub-5-nm-half-pitch lithography,” *J. Vac. Sci. Technol. B Microelectron. Nanom. Struct.*, vol. 27, no. 6, p. 2622, 2009.
- [24] J. A. van Kan, A. A. Bettoli, and F. Watt, “Hydrogen silsesquioxane a next generation resist for proton beam writing at the 20 nm level,” *Nucl. Instruments Methods Phys. Res. Sect. B Beam Interact. with Mater. Atoms*, vol. 260, no. 1, pp. 396–399, 2007.
- [25] R. G. Brault and L. J. Miller, “Sensitivity and contrast of some proton-beam resists,” *Polym. Eng. Sci.*, vol. 20, no. 16, pp. 1064–1068, Nov. 1980.
- [26] S. Choi, N. Jin, V. Kumar, I. Adesida, and M. Shannon, “Effects of developer temperature on electron-beam-exposed hydrogen silsesquioxane resist for ultradense silicon nanowire fabrication,” *J.*

*Vac. Sci. Technol. B Microelectron. Nanom. Struct.*, vol. 25, no. 6, p. 2085, Dec. 2007.

- [27] V. A. Sidorkin, “Resist and Exposure Processes for Sub-10-nm Electron and Ion Beam Lithography.” 2010.
- [28] R. . A. Lawes, “Future trends in high-resolution lithography,” *Appl. Surf. Sci.*, vol. 154, pp. 519–526, Feb. 2000.
- [29] P. Gupta, A. B. Kahng, D. Sylvester, and Jie Yang, “Performance Driven OPC for Mask Cost Reduction,” in *Sixth International Symposium on Quality of Electronic Design (ISQED’05)*, pp. 270–275.
- [30] K. Lucas *et al.*, “Triple patterning in 10nm node metal lithography.”
- [31] B. Yu, K. Yuan, D. Ding, and D. Z. Pan, “Layout Decomposition for Triple Patterning Lithography,” *IEEE Trans. Comput. Des. Integr. Circuits Syst.*, vol. 34, no. 3, pp. 433–446, Mar. 2015.
- [32] Y. Chen, *Nanofabrication by electron beam lithography and its applications: A review*, vol. 135. Elsevier, 2015, pp. 57–72.
- [33] R. F. W. Pease, “Electron beam lithography,” *Contemp. Phys.*, vol. 22, no. 3, pp. 265–290, 1981.
- [34] T. H. P. Chang, “Proximity effect in electron-beam lithography,” *Cit. J. Vac. Sci. Technol.*, vol. 12, p. 1271, 1975.
- [35] S. A. Rishton and D. P. Kern, “Point exposure distribution measurements for proximity correction in electron beam lithography on a sub-100 nm scale,” *J. Vac. Sci. Technol. B Microelectron. Nanom. Struct.*, vol. 5, no. 1, p. 135, Jan. 1987.
- [36] G. Owen and P. Rissman, “Proximity effect correction for electron beam lithography by equalization of background dose,” *J. Appl. Phys.*, vol. 54, no. 6, pp. 3573–3581, Jun. 1983.
- [37] C. Vieu *et al.*, “Electron beam lithography: resolution limits and applications,” *Appl. Surf. Sci.*, vol. 164, no. 1–4, pp. 111–117, Sep. 2000.
- [38] M. M. Greve and B. Holst, “Optimization of an electron beam lithography instrument for fast, large area writing at 10 kV acceleration voltage,” *J. Vac. Sci. Technol. B, Nanotechnol. Microelectron. Mater. Process. Meas. Phenom.*, vol. 31, no. 4, p. 043202, Jul. 2013.
- [39] A. A. A. Tseng *et al.*, “Electron beam lithography in nanoscale fabrication: Recent development,” *IEEE Trans. Electron. Packag. Manuf.*, vol. 26, no. 2, pp. 141–149, Apr. 2003.
- [40] A. S. Gangnaik, Y. M. Georgiev, and J. D. Holmes, “New Generation Electron Beam Resists: A Review.”

- [41] W. (Walter) Hu, K. Sarveswaran, M. Lieberman, and G. H. Bernstein, “Sub-10 nm electron beam lithography using cold development of poly(methylmethacrylate),” *J. Vac. Sci. Technol. B Microelectron. Nanom. Struct.*, 2004.
- [42] V. R. Manfrinato *et al.*, “Aberration-Corrected Electron Beam Lithography at the One Nanometer Length Scale,” *Nano Lett.*, 2017.
- [43] S. Gorelick, J. Vila-Comamala, V. Guzenko, R. Mokso, M. Stampaconi, and C. David, “Direct e-beam writing of high aspect ratio nanostructures in PMMA: A tool for diffractive X-ray optics fabrication,” 2009.
- [44] H. Miyoshi and J. Taniguchi, “Fabrication of a high-resolution mask by using variable-shaped electron beam lithography with a non-chemically amplified resist and a post-exposure bake,” *Microelectron. Eng.*, vol. 143, pp. 48–54, Aug. 2015.
- [45] P. Hahmann *et al.*, “High resolution variable-shaped beam direct write,” *Microelectron. Eng.*, vol. 84, no. 5–8, pp. 774–778, May 2007.
- [46] M. Green *et al.*, “Mask manufacturing of advanced technology designs using multi-beam lithography (Part 1),” 2016, vol. 10032, p. 1003205.
- [47] C. A. Volkert and A. M. Minor, “Focused Ion Beam Microscopy and Micromachining The FIB Instrument.”
- [48] D. K. Stewart, J. A. Doherty, A. F. Doyle, and J. C. Morgan, “State of the art in focused ion-beam mask repair systems,” 1995, vol. 2512, p. 398.
- [49] T. Liang, A. Stivers, R. Livengood, P.-Y. Yan, G. Zhang, and F.-C. Lo, “Progress in extreme ultraviolet mask repair using a focused ion beam,” *J. Vac. Sci. Technol. B Microelectron. Nanom. Struct. Process. Meas. Phenom.*, vol. 18, no. 6, p. 3216, Dec. 2000.
- [50] Z. Liu, K. Iltanen, N. Chekurov, K. Grigoras, and I. Tittonen, “Aluminum oxide mask fabrication by focused ion beam implantation combined with wet etching,” *Nanotechnology*, vol. 24, no. 17, p. 175304, May 2013.
- [51] P. Sievilä, N. Chekurov, and I. Tittonen, “The fabrication of silicon nanostructures by focused-ion-beam implantation and TMAH wet etching,” *Nanotechnology*, vol. 21, no. 14, p. 145301, Apr. 2010.
- [52] L. A. Giannuzzi and F. A. Stevie, “A review of focused ion beam milling techniques for TEM specimen preparation,” *Micron*, vol. 30, no. 3, pp. 197–204, Jun. 1999.
- [53] D. A. M. de Winter and J. J. L. Mulders, “Redeposition characteristics of focused ion beam milling for nanofabrication,” *J. Vac. Sci. Technol. B Microelectron. Nanom. Struct.*, vol. 25, no. 6, p. 2215, Dec. 2007.

- [54] B. W. Ward, J. A. Notte, and N. P. Economou, “Helium ion microscope: A new tool for nanoscale microscopy and metrology,” *J. Vac. Sci. Technol. B Microelectron. Nanom. Struct.*, vol. 24, no. 6, p. 2871, Nov. 2006.
- [55] M. S. Joens *et al.*, “Helium Ion Microscopy (HIM) for the imaging of biological samples at sub-nanometer resolution,” *Sci. Rep.*, vol. 3, no. 1, p. 3514, Dec. 2013.
- [56] D. Winston *et al.*, “Sub-10-nm nanolithography with a scanning helium beam,” *Metrol. J. Vac. Sci. Technol. B Microelectron. Nanom. Struct. Process. Meas. Phenom.*, vol. 27, p. 3244, 2009.
- [57] W.-D. Li, W. Wu, and R. Stanley Williams, “Combined helium ion beam and nanoimprint lithography attains 4 nm half-pitch dense patterns,” *J. Vac. Sci. Technol. B, Nanotechnol. Microelectron. Mater. Process. Meas. Phenom.*, vol. 30, no. 6, p. 06F304, Nov. 2012.
- [58] F. Watt, “Focused high energy proton beam micromachining: A perspective view,” *Nucl. Instruments Methods Phys. Res. Sect. B Beam Interact. with Mater. Atoms*, vol. 158, no. 1–4, pp. 165–172, Sep. 1999.
- [59] F. Watt, M. B. H. Breese, A. A. Bettoli, and J. A. van Kan, “Proton beam writing,” *Materials Today*, vol. 10, no. 6, pp. 20–29, 2007.
- [60] C. N. B. Udalagama, “A Monte Carlo study of the extent of proximity effects in e-beam and p-beam writing of PMMA,” *Nucl. Instruments Methods Phys. Res. Sect. B Beam Interact. with Mater. Atoms*, vol. 260, no. 1, pp. 384–389, Jul. 2007.
- [61] C. Udalagama, A. A. Bettoli, and F. Watt, “Stochastic spatial energy deposition profiles for MeV protons and keV electrons,” *Phys. Rev. B - Condens. Matter Mater. Phys.*, vol. 80, no. 22, p. 224107, Dec. 2009.
- [62] J. a Van Kan, A. a Bettoli, K. Ansari, and F. Watt, “Micromachining using a focused MeV proton beam for the production of high precision 3D microstructures with vertical sidewalls of high orthogonality,” *Signals*, vol. 4343, no. 65, pp. 466–472, 2001.
- [63] K. Ansari, J. A. Van Kan, A. A. Bettoli, and F. Watt, “Fabrication of high aspect ratio 100 nm metallic stamps for nanoimprint lithography using proton beam writing,” *Appl. Phys. Lett.*, 2004.
- [64] J. a. Van Kan, A. a. Bettoli, K. Ansari, E. J. Teo, T. C. Sum, and F. Watt, “Proton beam writing: a progress review,” *Int. J. Nanotechnol.*, vol. 1, no. 4, p. 464, 2004.
- [65] Y. Yao, P. Santhana Raman, and J. A. Van Kan, “Orthogonal and fine lithographic structures attained from the next generation proton beam writing facility,” *Microsyst. Technol.*, vol. 20, no. 10–11, pp. 2065–2069, 2014.

- [66] J. Melngailis, “A review of ion projection lithography,” *J. Vac. Sci. Technol. B Microelectron. Nanom. Struct.*, vol. 16, no. 3, p. 927, 1998.
- [67] S. Hirscher *et al.*, “Ion projection lithography below 70 nm: Tool performance and resist process,” in *Microelectronic Engineering*, 2002, vol. 61–62, pp. 301–307.
- [68] S. Gorelick, N. Puttaraksa, T. Sajavaara, M. Laitinen, S. Singkarat, and H. J. J. Whitlow, “Fabrication of microfluidic devices using MeV ion beam Programmable Proximity Aperture Lithography (PPAL),” *Nucl. Instruments Methods Phys. Res. Sect. B Beam Interact. with Mater. Atoms*, vol. 266, no. 10, pp. 2461–2465, May 2008.
- [69] S. Gorelick, N. Puttaraksa, T. Sajavaara, M. Laitinen, S. Singkarat, and H. J. J. Whitlow, “Fabrication of microfluidic devices using MeV ion beam Programmable Proximity Aperture Lithography (PPAL),” *Nucl. Instruments Methods Phys. Res. Sect. B Beam Interact. with Mater. Atoms*, vol. 266, no. 10, pp. 2461–2465, May 2008.
- [70] K. Ansari, P. G. Shao, J. A. Van Kan, A. A. Bettoli, and F. Watt, “Proton beam fabrication of nickel stamps for nanoimprint lithography,” *Nucl. Instruments Methods Phys. Res. Sect. B Beam Interact. with Mater. Atoms*, vol. 231, no. 1–4, pp. 407–412, 2005.
- [71] J. A. van Kan, L. P. Wang, P. G. Shao, A. A. Bettoli, and F. Watt, “High aspect ratio PDMS replication through proton beam fabricated Ni masters,” *Nucl. Instruments Methods Phys. Res. Sect. B Beam Interact. with Mater. Atoms*, vol. 260, no. 1, pp. 353–356, 2007.
- [72] F. Liu, Y. Yao, and J. A. Van Kan, “OrmoStamp mold fabrication via PBW for NIL,” *Nucl. Instruments Methods Phys. Res. Sect. B Beam Interact. with Mater. Atoms*, vol. 348, pp. 229–232, 2015.
- [73] S. Y. Chou and P. R. Krauss, “Imprint lithography with sub-10 nm feature size and high throughput,” *Microelectron. Eng.*, vol. 35, no. 1–4, pp. 237–240, Feb. 1997.
- [74] Y. Zhang, H. Whitlow, of Jyväskylä, and F. Harry JWhitlow, “25 Modification of Materials by MeV Ion Beams.”
- [75] M. Dapor, I. Abril, P. De Vera, and R. Garcia-Molina, “Energy deposition around swift proton tracks in polymethylmethacrylate: How much and how far,” *Phys. Rev. B*, vol. 96, no. 6, pp. 1–12, 2017.
- [76] J. A. Van Kan, T. C. Sum, T. Osipowicz, and F. Watt, “Sub 100 nm proton beam micromachining: theoretical calculations on resolution limits,” *Nucl. Instruments Methods Phys. Res. Sect. B Beam Interact. with Mater. Atoms*, vol. 161, pp. 366–370, 2000.
- [77] M. J. Rooks, E. Kratschmer, R. Viswanathan, J. Katine, R. E. Fontana, and S. A. MacDonald, “Low stress development of poly(methylmethacrylate) for high aspect ratio structures,” *J. Vac. Sci.*

- Technol. B Microelectron. Nanom. Struct.*, vol. 20, no. 6, p. 2937, 2002.
- [78] J. A. Van Kan, A. A. Bettoli, and F. Watt, “Three-dimensional nanolithography using proton beam writing,” *Appl. Phys. Lett.*, vol. 83, no. 8, pp. 1629–1631, 2003.
  - [79] T. C. Sum, A. A. Bettoli, H. L. Seng, J. A. Van Kan, and F. Watt, “Direct measurement of proton-beam-written polymer optical waveguide sidewall morphology using an atomic force microscope,” *Appl. Phys. Lett.*, vol. 85, no. 8, pp. 1398–1400, 2004.
  - [80] K. Ansari, J. A. Van Kan, A. A. Bettoli, and F. Watt, “Stamps for nanoimprint lithography fabricated by proton beam writing and nickel electroplating,” *J. Micromechanics Microengineering*, vol. 16, no. 10, pp. 1967–1974, 2006.
  - [81] J. A. Van Kan, I. Rajta, K. Ansari, A. A. Bettoli, and F. Watt, “Nickel and copper electroplating of proton beam micromachined SU-8 resist,” *Microsyst. Technol.*, vol. 8, no. 6, pp. 383–386, 2002.
  - [82] Y. H. Wang, P. Malar, and J. A. Van Kan, “Resist evaluation for proton beam writing, Ni mold fabrication and nano-replication,” *Microsyst. Technol.*, vol. 20, no. 10–11, pp. 2079–2088, 2014.
  - [83] P. G. Shao, J. A. van Kan, K. Ansari, A. A. Bettoli, and F. Watt, “Poly (dimethyl siloxane) micro/nanostructure replication using proton beam written masters,” *Nucl. Instruments Methods Phys. Res. Sect. B Beam Interact. with Mater. Atoms*, vol. 260, no. 1, pp. 479–482, 2007.
  - [84] F. van Delft, R. van de Laar, M. Verschuur, E. Platzgummer, and H. Loeschner, “Charged Particle Nanopatterning (CHARPAN) of 2D and 3D masters for flexible replication in Substrate Conformal Imprint Lithography (SCIL),” *Microelectron. Eng.*, vol. 87, no. 5–8, pp. 1062–1065, 2010.
  - [85] J. A. van Kan, C. Zhang, P. Perumal Malar, and J. R. C. van der Maarel, “High throughput fabrication of disposable nanofluidic lab-on-chip devices for single molecule studies,” *Biomicrofluidics*, vol. 6, no. 3, 2012.
  - [86] I. Rajta *et al.*, “Proton beam micromachined buried microchannels in negative tone resist materials,” *Nucl. Instruments Methods Phys. Res. Sect. B Beam Interact. with Mater. Atoms*, vol. 260, no. 1, pp. 414–418, 2007.
  - [87] C. Zhang, K. Jiang, F. Liu, P. S. Doyle, J. A. van Kan, and J. R. C. van der Maarel, “A nanofluidic device for single molecule studies with in situ control of environmental solution conditions,” *Lab Chip*, vol. 13, no. 14, p. 2821, 2013.
  - [88] C. Zhang *et al.*, “Nanofluidic compaction of DNA by like-charged protein,” *J. Phys. Chem. B*, vol. 116, no. 9, pp. 3031–3036, 2012.

- [89] S. Homhuan, B. Zhang, F. S. Sheu, A. A. Bettoli, and F. Watt, “Single-cell electroporation using proton beam fabricated biochips,” *Biomed. Microdevices*, vol. 14, no. 3, pp. 533–540, 2012.
- [90] F. Liu *et al.*, “Separation of superparamagnetic particles through ratcheted Brownian motion and periodically switching magnetic fields,” *Biomicrofluidics*, vol. 10, no. 6, 2016.
- [91] A. A. Bettoli *et al.*, “A progress review of proton beam writing applications in microphotonics,” *Nucl. Instruments Methods Phys. Res. Sect. B Beam Interact. with Mater. Atoms*, vol. 231, no. 1–4, pp. 364–371, 2005.
- [92] T. C. Sum *et al.*, “Proton beam writing of erbium-doped waveguide amplifiers,” *Nucl. Instruments Methods Phys. Res. Sect. B Beam Interact. with Mater. Atoms*, vol. 231, no. 1–4, pp. 394–399, 2005.
- [93] I. Bányaśz *et al.*, “Ion beam irradiated optical channel waveguides,” in *SPIE Photonics West 2014-OPTO: Optoelectronic Devices and Materials*, 2014, vol. 8988, p. 898814.
- [94] B. Volckaerts *et al.*, “Deep lithography with protons: A generic technology for the fabrication of refractive micro-optical modules,” *2000 IEEE/LEOS Int. Conf. Opt. MEMS*, pp. 103–104, 2000.
- [95] C. Udalagama, E. J. Teo, S. F. Chan, V. S. Kumar, A. A. Bettoli, and F. Watt, “Proton beam writing of long, arbitrary structures for micro/nano photonics and fluidics applications,” *Nucl. Instruments Methods Phys. Res. Sect. B Beam Interact. with Mater. Atoms*, vol. 269, no. 20, pp. 2417–2421, Oct. 2011.
- [96] A. A. Bettoli, S. P. Turaga, Y. Yan, S. K. Vanga, and S. Y. Chiam, “Three-dimensional metamaterials fabricated using Proton Beam Writing,” *Nucl. Instruments Methods Phys. Res. Sect. B Beam Interact. with Mater. Atoms*, vol. 306, pp. 271–274, 2013.
- [97] S. K. Vanga, V. Nalla, and A. A. Bettoli, “Polymer microlasers with a suspended cavity design,” *Opt. Mater. (Amst.)*, vol. 42, pp. 144–147, 2015.
- [98] I. Rajta, I. Gómez-Morilla, M. H. Abraham, and Á. Z. Kiss, “Proton beam micromachining on PMMA, Foturan and CR-39 materials,” *Nucl. Instruments Methods Phys. Res. Sect. B Beam Interact. with Mater. Atoms*, vol. 210, pp. 260–265, 2003.
- [99] I. Gomez-Morilla, M. H. Abraham, D. G. De Kerckhove, and G. W. Grime, “Micropatterning of Foturan photosensitive glass following exposure to MeV proton beams,” *J. Micromechanics Microengineering*, vol. 15, no. 4, pp. 706–709, 2005.
- [100] J. A. van Kan *et al.*, “New resists for proton beam writing,” *Nucl. Instruments Methods Phys. Res. Sect. B Beam Interact. with Mater.*

*Atoms*, vol. 260, no. 1, pp. 460–463, 2007.

- [101] F. Picollo *et al.*, “Realization of a diamond based high density multi electrode array by means of Deep Ion Beam Lithography,” *Nucl. Inst. Methods Phys. Res. B*, vol. 348, pp. 199–202, 2015.
- [102] J. Song, Z. Y. Dang, S. Azimi, M. B. H. Breese, J. Forneris, and E. Vittone, “On the Formation of 50 nm Diameter Free-Standing Silicon Wires Produced by Ion Irradiation,” *ECS J. Solid State Sci. Technol.*, vol. 1, no. 2, pp. P66–P69, 2012.
- [103] S. Azimi, J. Song, Z. Y. Dang, H. D. Liang, and M. B. H. Breese, “Three-dimensional silicon micromachining,” *J. Micromechanics Microengineering*, vol. 22, no. 11, 2012.
- [104] E. J. Teo *et al.*, “Fabrication of silicon microstructures using a high energy ion beam,” *Proc. SPIE*, vol. 5347, pp. 264–270, 2004.
- [105] J. Song, S. Azimi, Z. Y. Dang, and M. B. H. Breese, “Integration of nano-scale components and supports in micromachined 3D silicon structures,” *J. Micromechanics Microengineering*, vol. 24, no. 4, 2014.
- [106] Z. Dang *et al.*, “Silicon and porous silicon mid-infrared photonic crystals,” *Appl. Phys. A Mater. Sci. Process.*, vol. 112, no. 3, pp. 517–523, 2013.
- [107] S. Azimi *et al.*, “Lab on a Chip Buried centimeter-long micro-and nanochannel arrays in porous silicon and glass,” 2014.
- [108] I. Rajta, E. Baradács, M. Chatzichristidi, E. S. Valamontes, I. Uzonyi, and I. Raptis, “Proton beam micromachining on strippable aqueous base developable negative resist,” *Nucl. Instruments Methods Phys. Res. Sect. B Beam Interact. with Mater. Atoms*, vol. 231, no. 1–4, pp. 423–427, 2005.
- [109] I. Gomez-Morilla, C. J. Sofield, G. W. Grime, and R. Gwilliam, “Rapid deep micromachining of polytetrafluoroethylene by MeV ion bombardment in oxygen-rich atmospheres,” *J. Micromechanics Microengineering*, vol. 15, no. 4, pp. 698–701, 2005.
- [110] G. W. Grime, C. J. Sofield, I. Gomez-Morilla, R. Gwilliam, M. D. Ynsa, and O. Enguita, “Rapid direct micromachining of PTFE using MeV ions in an oxygen rich atmosphere,” *Nucl. Instruments Methods Phys. Res. Sect. B Beam Interact. with Mater. Atoms*, vol. 231, no. 1–4, pp. 378–383, 2005.
- [111] S. Z. Szilasi *et al.*, “PMMA melting under proton beam exposure,” *Nucl. Instruments Methods Phys. Res. Sect. B Beam Interact. with Mater. Atoms*, vol. 231, no. 1–4, pp. 419–422, 2005.
- [112] A. Alves, P. Reichart, R. Siegele, P. N. Johnston, and D. N. Jamieson, “Ion beam lithography using single ions,” *Nucl. Instruments Methods*

*Phys. Res. Sect. B Beam Interact. with Mater. Atoms*, vol. 249, no. 1–2 SPEC. ISS., pp. 730–733, 2006.

- [113] A. Alves, P. N. Johnston, P. Reichart, D. N. Jamieson, and R. Siegele, “Characterization of ion tracks in PMMA for single ion lithography,” *Nucl. Instruments Methods Phys. Res. Sect. B Beam Interact. with Mater. Atoms*, vol. 260, no. 1, pp. 431–436, Jul. 2007.
- [114] M. Chatzichristidi *et al.*, “Aqueous base developable: Easy stripping, high aspect ratio negative photoresist for optical and proton beam lithography,” in *Microsystem Technologies*, 2008, vol. 14, no. 9–11, pp. 1423–1428.
- [115] M. Chatzichristidi *et al.*, “High aspect ratio micro/nano machining with proton beam writing on aqueous developable - easily stripped negative chemically-amplified resists,” *Microelectron. Eng.*, vol. 85, no. 5–6, pp. 945–948, 2008.
- [116] J. A. van Kan, F. Zhang, C. Zhang, A. A. Bettoli, and F. Watt, “Exposure parameters in proton beam writing for hydrogen silsesquioxane,” *Nucl. Instruments Methods Phys. Res. Sect. B Beam Interact. with Mater. Atoms*, vol. 266, no. 8, pp. 1676–1679, 2008.
- [117] M. D. Ynsa, P. Shao, S. R. Kulkarni, N. N. Liu, and J. A. Van Kan, “Exposure parameters in proton beam writing for KMPR and EPO Core negative tone photoresists,” *Nucl. Instruments Methods Phys. Res. Sect. B Beam Interact. with Mater. Atoms*, vol. 269, no. 20, pp. 2409–2412, 2011.
- [118] N. Puttaraksa, R. Norarat, M. Laitinen, T. Sajavaara, S. Singkarat, and H. J. Whitlow, “Lithography exposure characteristics of poly(methyl methacrylate) (PMMA) for carbon, helium and hydrogen ions,” *Nucl. Instruments Methods Phys. Res. Sect. B Beam Interact. with Mater. Atoms*, vol. 272, pp. 162–164, Feb. 2012.
- [119] Y. Koike *et al.*, “Micro fabrication of poly L lacid and its application,” in *The 1st IEEE Global Conference on Consumer Electronics 2012*, 2012, pp. 60–61.
- [120] Y. Maeyoshi *et al.*, “Fabrication of Poly(9,9\$’\$-dioctylfluorene)-Based Nano- and Microstructures by Proton Beam Writing,” *Jpn. J. Appl. Phys.*, vol. 51, p. 045201, Mar. 2012.
- [121] K. Takano *et al.*, “Microprocessing of Arched Bridge Structures with Epoxy Resin by Proton Beam Writing,” *J. Photopolym. Sci. Technol.*, vol. 25, no. 1, pp. 43–46, 2012.
- [122] Y. H. Wang, P. Malar, J. Zhao, and J. A. Van Kan, “Resist evaluation for Ni mold fabrication and proton beam writing,” 2013.
- [123] E. Højlund-Nielsen, T. Greibe, N. A. Mortensen, and A. Kristensen, “Single-spot e-beam lithography for defining large arrays of nano-

- holes,” *Microelectron. Eng.*, vol. 121, pp. 104–107, Jun. 2014.
- [124] J. A. Van Kan, P. Malar, and Y. H. Wang, “Resist materials for proton beam writing: A review,” *Appl. Surf. Sci.*, vol. 310, pp. 100–111, 2014.
- [125] G. W. Grime and F. Watt, *Beam Optics of Quadrupole Probe-forming Systems*. Adam Hilger Limited, 1984.
- [126] R. Nob1ling, Y. Civelekocjlu, D. Schwalm, and K. Traxel, “COLLIMATION OF ION BEAMS TO MICROMETER DIMENSIONS.”
- [127] J. A. Cookson, “THE PRODUCTION AND USE OF A NUCLEAR MICROPROBE OF IONS AT MeV ENERGIES.”
- [128] S. Gorelick and H. J. Whitlow, “Aperture edge scattering in focused MeV ion beam lithography and nuclear microscopy: An application for the GEANT4 toolkit,” *Nucl. Instruments Methods Phys. Res. Sect. B Beam Interact. with Mater. Atoms*, vol. 267, no. 12–13, pp. 2050–2053, 2009.
- [129] J. A. Van Kan, P. Malar, A. B. De Vera, X. Chen, A. A. Bettoli, and F. Watt, “Proton beam writing nanoprobe facility design and first test results,” in *Nuclear Instruments and Methods in Physics Research, Section A: Accelerators, Spectrometers, Detectors and Associated Equipment*, 2011.
- [130] F. Watt, T. F. Choo, K. K. Lee, T. Osipowicz, I. Orlic, and S. M. Tang, “The effect of external fields and slit scattering on the beam spot profile of the coupled triplet system,” *Nucl. Inst. Methods Phys. Res. B*, 1995.
- [131] T. Osipowicz, H. L. Seng, T. K. Chan, and B. Ho, “The CIBA high resolution RBS facility,” *Nucl. Instruments Methods Phys. Res. Sect. B Beam Interact. with Mater. Atoms*, 2006.
- [132] F. Watt, X. Chen, C. B. Chen, C. N. B. Udalagama, J. A. Van Kan, and A. A. Bettoli, “Whole cell structural imaging at 20 nanometre resolutions using MeV ions,” *Nucl. Instruments Methods Phys. Res. Sect. B Beam Interact. with Mater. Atoms*, 2013.
- [133] R. Minqin, F. Watt, B. T. K. Huat, and B. Halliwell, “Trace elemental distributions in induced atherosclerotic lesions using nuclear microscopy,” in *Nuclear Instruments and Methods in Physics Research, Section B: Beam Interactions with Materials and Atoms*, 2003.
- [134] Y. Yao and J. A. Van Kan, “Automatic beam focusing in the 2ndgeneration PBW line at sub-10 nm line resolution,” *Nucl. Instruments Methods Phys. Res. Sect. B Beam Interact. with Mater. Atoms*, vol. 348, pp. 203–208, 2015.
- [135] AccelSoft Inc., “PBO Lab.” [Online]. Available: <http://www.ghga.com/accelsoft/pbolab.html>.

- [136] C. UDALAGAMA, A. A. BETTIOL, and F. WATT, “Imaging using pulses: a simple and fast (>100 kHz) solution,” *J. Microsc.*, vol. 238, no. 2, pp. 185–188, May 2010.
- [137] J. A. Van Kan, A. A. Bettiol, and F. Watt, “Proton beam writing of three-dimensional nanostructures in hydrogen silsesquioxane,” *Nano Lett.*, vol. 6, no. 3, pp. 579–582, 2006.
- [138] Y. Yao, M. W. Van Mourik, P. Santhana Raman, and J. A. Van Kan, “Improved beam spot measurements in the 2nd generation proton beam writing system,” *Nucl. Instruments Methods Phys. Res. Sect. B Beam Interact. with Mater. Atoms*, vol. 306, pp. 265–270, 2013.
- [139] R. M. Sealock, D. N. Jamieson, and G. J. F. Legge, “Scanning transmission microscopy with a 2 MeV alpha particle microbeam,” *Nucl. Instruments Methods Phys. Res. Sect. B Beam Interact. with Mater. Atoms*, vol. 29, no. 3, pp. 557–566, Dec. 1987.
- [140] M. Cholewa, G. J. F. Legge, I. Dierck, and R. Van Grieken, “STIM investigation of laser microprobe damage,” *Nucl. Instruments Methods Phys. Res. Sect. B Beam Interact. with Mater. Atoms*, vol. 54, no. 1–3, pp. 109–114, Mar. 1991.
- [141] J. F. Ziegler, M. D. Ziegler, and J. P. Biersack, “SRIM - The stopping and range of ions in matter (2010),” *Nucl. Instruments Methods Phys. Res. Sect. B Beam Interact. with Mater. Atoms*, 2010.
- [142] D. N. Jamieson, “New generation nuclear microprobe systems,” in *Nuclear Instruments and Methods in Physics Research, Section B: Beam Interactions with Materials and Atoms*, 2001.
- [143] N. Instruments, “LabVIEW 2011.” [Online]. Available: <http://www.ni.com/labview/release-archive/2011/>.
- [144] A. A. Bettiol, C. N. B. Udalagama, J. A. van Kan, and F. Watt, “Ionscan: scanning and control software for proton beam writing,” *Nucl. Instruments Methods Phys. Res. Sect. B Beam Interact. with Mater. Atoms*, vol. 231, no. 1–4, pp. 400–406, Apr. 2005.
- [145] A. A. Bettiol, C. N. B. Udalagama, J. A. Van Kan, and F. Watt, “Ionscan: Scanning and control software for proton beam writing,” *Nucl. Instruments Methods Phys. Res. Sect. B Beam Interact. with Mater. Atoms*, vol. 231, no. 1–4, pp. 400–406, 2005.
- [146] T. C. Sum, A. A. Bettiol, H. L. Seng, J. A. Van Kan, and F. Watt, “Direct measurement of proton-beam-written polymer optical waveguide sidewall morphology using an atomic force microscope,” *Cit. Appl. Phys. Lett.*, vol. 85, no. 10, pp. 1398–1707, 2004.
- [147] S. Qureshi, P. S. Raman, A. Stegmaier, and J. A. van Kan, “Quadrupole lens alignment with improved STIM and secondary electron imaging for Proton Beam Writing,” *Nucl. Instruments Methods Phys. Res. Sect.*

*B Beam Interact. with Mater. Atoms*, vol. 404, pp. 74–80, 2017.

- [148] R. Szymanski and D. N. Jamieson, “Ion source brightness and nuclear microprobe applications,” *Nucl. Instruments Methods Phys. Res. Sect. B Beam Interact. with Mater. Atoms*, vol. 130, no. 1–4, pp. 80–85, Jul. 1997.
- [149] J. A. Van Kan, P. Malar, A. B. De Vera, X. Chen, A. A. Bettoli, and F. Watt, “Proton beam writing nanoprobe facility design and first test results,” *Nucl. Instruments Methods Phys. Res. Sect. A Accel. Spectrometers, Detect. Assoc. Equip.*, vol. 645, no. 1, pp. 113–115, 2011.
- [150] J. Ladislas Wiza, “Microchannel plate detectors,” *Nucl. Instruments Methods*, 1979.
- [151] D. Hasselkamp, S. Hippler, A. Scharmann, and T. Schmehl, “Electron Emission from Clean Solid Surfaces by Fast Ions,” *Ann. Phys.*, vol. 502, no. 7, pp. 555–567, 1990.
- [152] D. Hasselkamp, “Kinetic Electron Emission from Solid Surfaces Under Ion Bombardment.”
- [153] E. J. Sternglass, “Theory of Secondary Electron Emission by High-Speed Ions,” *SscoND SsR1ss*, vol. 108, no. 1, 1957.
- [154] E. Veje, “Secondary electron emission from gold bombarded with H+, H<sub>2</sub>+, H<sub>3</sub>+, He+, and HeH+,” *Nucl. Instruments Methods Phys. Res.*, vol. 194, no. 1–3, pp. 433–436, Mar. 1982.
- [155] Y. Yao, P. Santhana Raman, and J. A. van Kan, “Orthogonal and fine lithographic structures attained from the next generation proton beam writing facility,” *Microsyst. Technol.*, vol. 20, no. 10–11, pp. 2065–2069, Oct. 2014.
- [156] S. Gorelick, F. Zhang, J. A. van Kan, H. J. Whitlow, and F. Watt, “Adhesion of proton beam written high aspect ratio hydrogen silsesquioxane (HSQ) nanostructures on different metallic substrates,” *Nucl. Instruments Methods Phys. Res. Sect. B Beam Interact. with Mater. Atoms*, vol. 267, no. 19, pp. 3314–3318, 2009.
- [157] M. B. H. Breese, E. J. Teo, D. Mangaiyarkarasi, F. Champeaux, A. A. Bettoli, and D. Blackwood, “Proton beam writing of microstructures in silicon,” in *Nuclear Instruments and Methods in Physics Research, Section B: Beam Interactions with Materials and Atoms*, 2005.
- [158] T. Yamaguchi and S. Sato, “Continuously Variable Threshold Voltage Devices,” in *1974 International Electron Devices Meeting (IEDM)*, 1974, pp. 537–540.
- [159] W. J. W. Selinger R.L., R. L. Seliger, and J. W. Ward, *Fabrication of lateral doping profiles by a computer-controlled focused ion beam*, vol.

12. American vacuum Society, 1975, pp. 1378–1381.
- [160] W. V. Seliger, R.L., Kubena R.L., Olney R.D., Ward, J.W., “High-resolution, ion-beam processes for microstructure fabrication.” pp. 1610–1612, 1979.
- [161] F. L. Lithography and I. O. N. Beams, “Ilesanmi ADESIDA \*,” pp. 923–928, 1985.
- [162] J. N. Randall, “Linewidth control with masked ion beam lithography using stencil masks,” *J. Vac. Sci. Technol. B Microelectron. Nanom. Struct.*, vol. 4, no. 1, p. 10, Jan. 1986.
- [163] S. W. Pang, “Submicrometer Structures Fabricated by Masked Ion Beam Lithography and Dry Etching,” *J. Electrochem. Soc.*, vol. 135, no. 6, p. 1526, 1988.
- [164] L. M. Buchmann *et al.*, “Lithography with High Depth of Focus by an Ion Projection System,” *J. Microelectromechanical Syst.*, vol. 1, no. 3, pp. 116–120, 1992.
- [165] J. C. Wolfe *et al.*, “A proximity ion beam lithography process for high density nanostructures,” *J. Vac. Sci. Technol. B Microelectron. Nanom. Struct.*, vol. 14, no. 6, p. 3896, Nov. 1996.
- [166] I. Rangelow *et al.*, “Silicon stencil masks for masked ion beam lithography proximity printing,” *Microelectron. Eng.*, vol. 30, pp. 257–260, 1996.
- [167] P. Hudek, “Deep ultraviolet resists AZ DX-561 and AZ DX-1300P applied for electron beam and masked ion beam lithography,” *J. Vac. Sci. Technol. B Microelectron. Nanom. Struct.*, vol. 15, no. 6, p. 2550, Nov. 1997.
- [168] J. D. Gillaspy, D. C. Parks, and L. P. Ratliff, “Masked ion beam lithography with highly charged ions,” *J. Vac. Sci. Technol. B*, vol. 16, no. 6, pp. 3294–3297, 1998.
- [169] M. M. Deshmukh, D. C. Ralph, M. Thomas, and J. Silcox, “Nanofabrication using a stencil mask,” *Appl. Phys. Lett.*, vol. 75, no. 11, pp. 1631–1633, 1999.
- [170] A. Ehrmann *et al.*, “Stencil mask key parameter measurement and control,” in *Proceedings of SPIE - The International Society for Optical Engineering*, 2000, vol. 3997, pp. 373–384.
- [171] T. Shibata, K. Suguro, K. Sugihara, T. Nishihashi, J. Fujiyama, and Y. Sakurada, “Stencil mask ion implantation technology,” *IEEE Trans. Semicond. Manuf.*, vol. 15, no. 2, pp. 183–188, 2002.
- [172] S. Eder-Kapl *et al.*, “Line edge roughness investigation on chemically amplified resist materials with masked helium ion beam lithography,”

- in *Microelectronic Engineering*, 2004, vol. 73–74, pp. 252–258.
- [173] M. L. Taylor *et al.*, “Ion beam lithography using a nano-aperture,” *Nucl. Instruments Methods Phys. Res. Sect. B Beam Interact. with Mater. Atoms*, vol. 260, no. 1, pp. 426–430, 2007.
- [174] G. Villanueva *et al.*, “Etching of sub-micrometer structures through Stencil,” *Microelectron. Eng.*, vol. 85, no. 5–6, pp. 1010–1014, 2008.
- [175] J. Allison *et al.*, “Geant4 developments and applications,” *IEEE Trans. Nucl. Sci.*, 2006.
- [176] J. Allison *et al.*, “Recent developments in GEANT4,” *Nucl. Instruments Methods Phys. Res. Sect. A Accel. Spectrometers, Detect. Assoc. Equip.*, 2016.
- [177] J. Van Donkelaar *et al.*, “Single atom devices by ion implantation,” *J. Phys. Condens. Matter*, vol. 27, no. 15, 2015.
- [178] M. H. Mendenhall and R. A. Weller, “An algorithm for computing screened coulomb scattering in GEANT4,” *Nucl. Instruments Methods Phys. Res. Sect. B Beam Interact. with Mater. Atoms*, 2005.
- [179] D. Drouin, A. R. Couture, D. Joly, X. Tastet, V. Aimez, and R. Gauvin, “CASINO V2.42 - A fast and easy-to-use modeling tool for scanning electron microscopy and microanalysis users,” *Scanning*, 2007.
- [180] H. W. Lewis, “Multiple Scattering in an Infinite Medium,” *Phys. Rev.*, vol. 78, no. 5, pp. 526–529, Jun. 1950.
- [181] F. Watt *et al.*, “The National University of Singapore high energy ion nano-probe facility: Performance tests,” *Nucl. Instruments Methods Phys. Res. Sect. B Beam Interact. with Mater. Atoms*, vol. 210, pp. 14–20, Sep. 2003.
- [182] J. A. Van Kan, P. G. Shao, K. Ansari, A. A. Bettoli, T. Osipowicz, and F. Watt, “Proton beam writing: A tool for high-aspect ratio mask production,” *Microsyst. Technol.*, vol. 13, no. 5–6, pp. 431–434, 2007.
- [183] J. A. Van Kan, P. G. Shao, Y. H. Wang, and P. Malar, “Proton beam writing a platform technology for high quality three-dimensional metal mold fabrication for nanofluidic applications,” *Microsyst. Technol.*, 2011.
- [184] Y. H. Wang, P. Malar, and J. A. Van Kan, “Resist evaluation for proton beam writing, Ni mold fabrication and nano-replication,” *Microsyst. Technol.*, vol. 20, no. 10–11, pp. 2079–2088, 2014.
- [185] J. A. Van Kan, P. Malar, and Y. H. Wang, “Resist materials for proton beam writing: A review,” *Appl. Surf. Sci.*, vol. 310, pp. 100–111, 2014.
- [186] X. Xu, R. Pang, P. S. Raman, R. Mariappan, A. Khursheed, and J. A.

- van Kan, “Fabrication and development of high brightness nano-aperture ion source,” *Microelectron. Eng.*, vol. 174, pp. 20–23, 2017.
- [187] L. van Kouwen and P. Kruit, “Brightness measurements of the nano-aperture ion source,” *J. Vac. Sci. Technol. B*, vol. 36, no. 6, p. 06J901, Nov. 2018.
- [188] X. Xu *et al.*, “Design considerations for a compact proton beam writing system aiming for fast sub-10 nm direct write lithography,” *Nucl. Instruments Methods Phys. Res. Sect. B Beam Interact. with Mater. Atoms*, vol. 404, pp. 243–249, 2017.